FUNDAMENTAL STUDY OF THE DESIGN AND DEVELOPMENT OF MAGNESIUM-ZINC BASED ALLOYS FOR BIODEGRADABLE IMPLANT DEVICES

by

Daeho Hong

B.S. in Computer Engineering, Purdue University, 2009

Submitted to the Graduate Faculty of

the Swanson School of Engineering in partial fulfillment

of the requirements for the degree of

Doctor of Philosophy

University of Pittsburgh

2015

UNIVERSITY OF PITTSBURGH

SWANSON SCHOOL OF ENGINEERING

This dissertation was presented

by

Daeho Hong

It was defended on

November 20, 2015

and approved by

Prashant N. Kumta, PhD, Department of Bioengineering, University of Pittsburgh

Harvey Borovetz, PhD, Department of Bioengineering, University of Pittsburgh

Spandan Maiti, PhD, Department of Bioengineering, University of Pittsburgh

Howard A. Kuhn, PhD, Department of Industrial Engineering, University of Pittsburgh

Arif Sirinterlikci, PhD, Department of Engineering, Robert Morris University

Dissertation Director: Prashant N. Kumta, PhD, Department of Bioengineering, University of Pittsburgh

Copyright © by Daeho Hong

2015

FUNDAMENTAL STUDY OF THE DESIGN AND DEVELOPMENT OF MAGNESIUM-ZINC BASED ALLOYS FOR BIODEGRADABLE IMPLANT DEVICES

Daeho Hong, PhD

University of Pittsburgh, 2015

Inert but biocompatible metals and biodegradable polymers are currently used as orthopedic fixations devices to achieve bone healing. However, the high stiffness of permanent metals such as stainless steel (SS), cobalt-chromium (Co-Cr), and titanium (Ti) alloys can cause stress shielding and loosening of the surrounding bone. Long term use of these devices can also result in wear related debris and associated risks of metallosis requiring secondary removal surgeries causing further complications. Inferior strength and acidic degradation products of biodegradable polymers on the other hand, also limit their use as orthopedic devices. Recently, biodegradable magnesium (Mg) and Mg-based alloys have received wide attention and have become the target of intense research due to the benefit of degradability, suitable mechanical properties matching natural bone and the desired biocompatibility. The degradation mechanism of biodegradable magnesium is primarily corrosion which tends to be highly rapid for pure Mg and most Mg based alloys resulting in rapid evolution of unwanted hydrogen gas pockets. Hence, controlling the corrosion of magnesium has been the key challenge limiting the technological development, thwarting the accelerated progress of implementation of Mg based alloys for various biomedical applications. Rapid corrosion of magnesium in the body and the associated hydrogen gas evolution results in device failure, and consequent risks of pain and potential infection. Alteration of alloy composition and the associated microstructure has been typically employed to improve the corrosion resistance and achieve the desired mechanical properties while maintaining the essential biocompatibility suitable for a desired biomedical application.

In this work, Mg-Zn based alloys were developed for biodegradable orthopedic fixation device applications. Magnesium-zinc alloys have the advantage of using zinc as a major alloying element that is considered biocompatible up to a daily dose of 11 mg. Mg-Zn-Zr was thus selected as the alloy system that was accordingly processed systematically varying the elemental composition, and characterizing the resultant system for phase, structure, microstructure, in-vitro corrosion and cytocompatibility properties yielding promising preliminary results. Results of characterization showed that the processing related Mg-Zn intermetallic precipitates formed at the grain boundaries acting as initiation centers for corrosion leading to reduction in the corrosion resistance. Thus, strontium and cerium were selected and added as micro alloying elements to improve the corrosion resistance due to alteration of the alloy phase dynamics and thermodynamic stability of the precipitates. In addition, the osteogenic attributes of Mg, Sr, and Ce ions were studied using human mesenchymal stem cells.

Furthermore, to demonstrate the biosafety of Mg-Zn alloys, Mg-Zn-Sr-Zr pins were implanted in a rat femoral fracture model. The model was selectively designed to result in extreme stress on the machined Mg-Zn pin hardware and also test their biocompatibility under load-bearing conditions. As intended, higher degradation rates and device failures were observed in the micro-computed tomography (micro-CT) images. Despite the pre-designed extreme stress assisted corrosion observed, normal fracture healing response was still exhibited in the micro-CT images and bone histology demonstrating the efficacy of the alloy system. Moreover, no systemic or local tissue toxicity were detected from blood, liver and kidney assessments further validating the beneficial aspects of this alloys system for orthopedic applications.

TABLE OF CONTENTS

LIST OF TABLES

LIST OF FIGURES

PREFACE

First of all, I thank God for giving me strength and wisdom to get through all the hurdles during my undergraduate and graduate studies in the United States. There are also several people who contributed to the research and study of this dissertation work. While working with them, I learned how to perform a scientific research and I could complete this work for my graduation.

I am forever grateful to Dr. Prashant N. Kumta for accepting me as his graduate student and advising my research and dissertation. He saw my potential to succeed in biomaterials research although my educational background was in computer engineering. He made an effort to meet with me and discuss the every step of the research whenever he was available. He went beyond the level of advisorship that is required to complete this dissertation and took a role of an academic father, guiding me to reborn as a biomaterials expert.

I am also grateful to my dissertation committee members. Drs. Harvey Borovetz, Spandan Maiti, Howard Kuhn, and Arif Sirinterlikci helped me during the course of this research and made valuable comments to excel the quality of this dissertation.

I would like to thank my fellow researchers. Dr. Da-Tren Chou was a great co-worker/friend who worked together to develop our patent-pending biodegradable Mg-based alloys and pursue 3D printing of Fe-Mn system. Drs. Abhijit Roy, Partha Saha, Moni Datta, and Oleg I. Velikokhatnyi were helpful post-docs who always answered my questions.

I also would like to thank Boeun Lee, Sudhanshu Shekhar, Sung Jae Chung, Jingyao Wu, Mitali Patil, Dr. Nicole Ostrowski, and Dr. Satish Singh were great labmates who worked closely with me and helped me in many ways.

Finally, I thank my wife and family who has trusted me and supported me throughout my dissertation studies. My lovely wife, Yoon Jung Huh, postponed her own graduate studies to spend time with me after our marriage and helped me in all directions to succeed in my dissertation study. Both my parents and parents-in-law supported me with their heart and prayers. Also, my mother's side families in New York took a good care of me from the day I arrived in the United States for the first time.

Pittsburgh has been my new home in the United States as I spent the longest time and became a permanent resident of the United States in this city. With all good memories that I had in Pittsburgh, I look forward to a new beginning of my career.

1.0 INTRODUCTION

1.1 ORTHOPEDIC FRACTURE RECONSTRUCTION AND REPAIR

Orthopedic fractures are common injuries resulting from debilitating diseases, sports related accidents, occupational injuries, traumatic car accidents, etc. arising from normal daily activities of individuals. The increase in life expectancy of global population is also related to the growing demand for orthopedic treatment (1). In the United States alone, the total orthopedic device market has witnessed an increase from US$ 9.7 billion in 2003 to US$ 29.2 billion in 2013 at the compounded annual growth rate of 11.6% (2).

In the clinic, the fracture fixation and repair is primarily focused on the reunion of bone fragments using fixation devices (3) (4). On the other hand, bone grafting is required additionally to fill a critical-sized defect (CSD) which is typically beyond the capability of natural bone healing process due to the size of the detect itself (5). Regardless of the need for bone grafting, use of the appropriate bone fixation devices is critical to anatomically align the remaining fragments or bone graft to fit the defect size, shape and configuration in most cases to avoid loosening and other post-surgery related complications due to improper fitting of the hardware (6).

Bone fixation is the first step in a typical bone reconstruction process associated with surgical remediation and intervention that is needed to address the loss and complicated bone injuries sustained by individuals either in the battlefield or due to normal aging as well as traumatic accidents. In all cases, stable fixation contributes to low and moderate inter-fragmentary movements required for tissue differentiation during the fracture healing process (7). Initial inflammatory phase of fracture healing process depends on systematic inflammatory factors such as trauma-induced inflammatory response, sepsis, leukocytosis/leukocyte activation, diabetes, and autoimmune diseases as well as the local inflammatory factor, fracture stability (8). Unstable fixation will inevitably lead to the inhibition of the fracture healing process causing an avalanche of problems, and hence, the effectiveness of fixation device is extremely important (9).

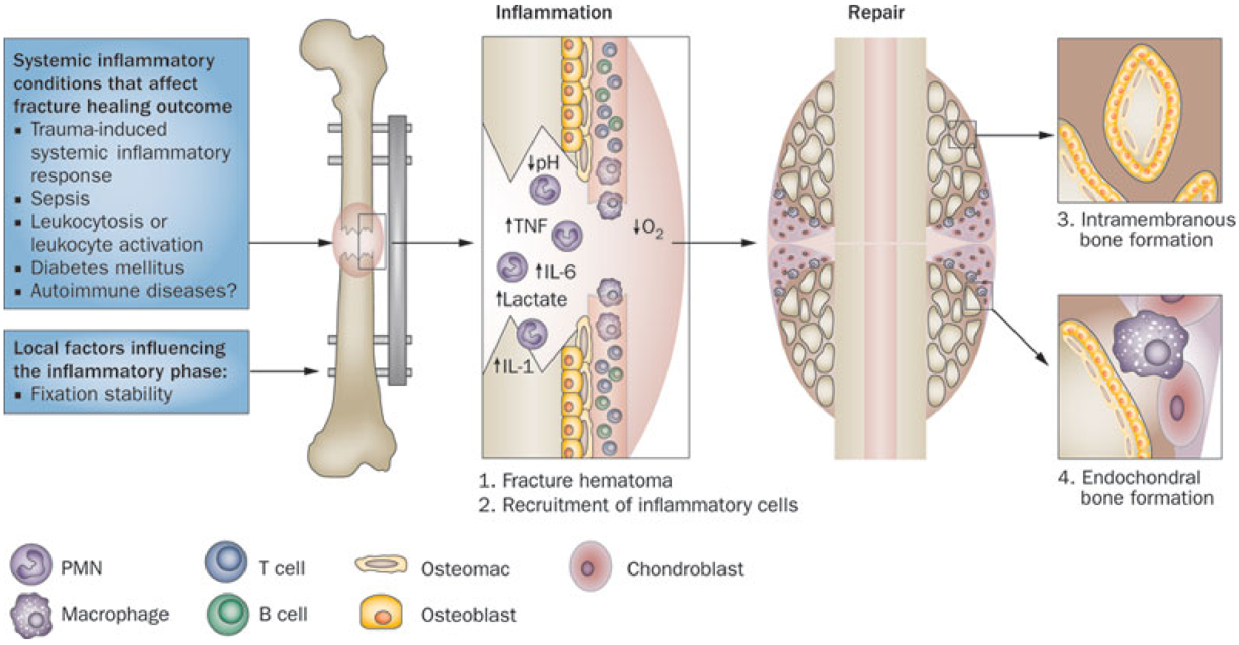

Figure 1.1 The fracture fixation and healing process (6).

It is normal that following fixation of bone fragments as shown in Figure 1.1, bleeding or hematoma formation, revascularization, and inflammation processes continue with recruitment of the related cells, cytokines and growth factors. Gradually in time, callus and fibrocartilage tissue forms, wrapping around the fracture site. Osteoblastic differentiation of mesenchymal stem cells then occurs in the callus to bridge the bones by the mineralization of osteoblasts. Osteoclast activity is then known to remodel the mineralized tissue at the wounded site to complete the repair and modeling of new bone formation.

1.2 CURRENT CLINICAL SOLUTION AND ITS LIMITATION

1.2.1 Inert metal implants

Figure 1.2 CT scan image showing the intraspinal migration of one K-wire (10).

The remediation or medical intervention processes currently in vogue for addressing complex fractures involving bone defects greater than the critical size outlined above require incorporation of hardware devices that are essentially belonging to either synthetic materials, autografts or allografts (11). The latter two involving grafts taken from another site of the patient of from a cadaver suffer from limitations of infections and risk of transmitted diseases. The synthetic implant materials are by far the most common mode of treatment of complex fractures comprising CSD conditions. The synthetic materials systems typically comprise three major classes of biomaterials: metals, ceramics, and polymers, the metals have gained popularity for load-bearing applications due to their high stiffness and mechanical strength, compared to polymers and ceramic materials (12). Thus, metallic implants based on titanium alloy (Ti6Al4V) and stainless steel (SS316L) have been used for more than a decade by clinicians for orthopedic reconstruction. These biocompatible but inert metals are designed to be corrosion resistant and biologically inactive in the body. However, use of orthopedic devices made of these inert metals has some limitations and can lead to several long-term side effects.

A most common problem is the strong mismatch between the elastic moduli and tensile strength of the metals and the bone causing stress shielding effect resulting in the weakening of the surrounding bone. Bone resorption is often observed at the interface between the bone tissue and the inert metal devices such as fixation plates and femoral rod (13, 14). High stiffness of the inert metal device with a sharp tip also induces a dangerous migration as shown in Figure 1.2 (15).

In addition, the long term use of current inert metal implants often requires invasive secondary surgery to prevent the side effects from corrosion and wear debris causing metallosis (16-18). Furthermore, immuno-inflammatory response is often observed in stainless steel or titanium plate and screws when used in human patients. The presence of T-lymphocytes, B-lymphocytes, and macrophages near these implant devices proves that the inert biometals has some involvement in tissue reaction. Immuno-inflammatory response can result in causing osteolysis and aseptic loosening at the interface between the bone and implant device.

Table 1.1 Properties and fabrication of biodegradable polymer materials (19).

Polymer	Melting point T_m (°C)	Glass transition point T_g (°C)	Biodegradation time (months)	Compressive* or tensile strength (MPa)	Modulus (GPa)
PDLLA	Amorphous	55–60	12–16	Pellet: 35–150* Film or disk: 29–35	Film or disk: 1.9–2.4
PLLA	173–178	60–65	>24	Pellet: 40–120* Film or disk: 28–50 Fibre: 870–2300	Film or disk: 1.2–3.0 Fibre: 10–16
PGA	225–230	35–40	6–12	Fibre: 340–920	Fibre: 7–14
PLGA	Amorphous	45–55	Adjustable: 1–12	41.4–55.2	1.4–2.8
PPF			Bulk	2–30*	
PCL	58	−72	>24		
PHA and blends	120-177	-2 to 4	Bulk	20-43	
Poly(anhydrides)				25-27	0.14-1.4
Poly(ortho-esters)	30–100		Surface	4–16*	2.5–4.4
Polyphosphazene	−66 to 50	242	Surface		

No significant toxicity has been detected experimentally or reported clinically due to the accumulation of titanium or iron at a systematic level or in specific organs. Therefore, most often, surgical removal has been the preferred solution to treat these complications arising from use of inert metal fixation devices. However, a removal surgery places the patient at a higher risk of infection with accrual of additional cost. Hence, there is a need for further improvement or the development of new concepts to provide better clinical care in treating orthopedic fractures.

1.2.2 Polymeric implants

In addition to the inert biometals, biodegradable polymeric materials are also widely used in clinics for bone tissue engineering applications. Poly (glycolic acid) (PGA), Poly (lactic acid) (PLA), and their blends have been investigated and commercialized for orthopedic fixation devices. Poly (glycolic acid) was the first biodegradable polymer that was approved by the U.S Food and Drug Administration in 1969 (20). Although PGA was initially approved as sutures, its use was extended to bone fixation device due to its high crystallinity (45-55%) resulting in suitable mechanical properties (21). Poly (lactic acid) on the other hand, is synthesized in two optically active isomers; L-lactide and D-lactide. PLA exhibits ~37% crystallinity, high tensile strength, low extension, high modulus, and slow degradation. Due to these characteristics, PLA has been used for orthopedic applications in load-bearing conditions. The blends of PGA and PLA were synthesized to optimize the mechanical and degradation properties required for each application. Table 1.1 summarizes the biodegradable polymer attributes for orthopedic applications such as tensile strength, compressive strength, modulus, elongation, degradation time, degradation product, and the various application areas.

Despite the advantage of biodegradability, acidic degradation products cause low pH in the local tissue and hence, adverse tissue reaction is often observed to result in swelling and pain. More number of such cases have been reported of late from the clinical use of PGA. PLA is also reported for its slow degradation and some cases exhibited delayed inflammatory response after 4 or 5 years. The amount of biodegradable polymers implanted in patient is highly correlated with the risk of having a foreign body reaction (FBR). In addition, exposure of the material to different tissue environment is another factor that determines the probability of inflammatory response. Therefore, the use of biodegradable polymers as bone fixation device requires further improvement in mechanical strength and biocompatibility to obtain clinical versatility. Another limitation of biodegradable polymers for orthopedic applications is its lack of osteogenic potential or ability to induce mineralization. Hence, the polymers are often required to be further augmented with ability to deliver growth factors to induce bone regeneration via encapsulation of microspheres or microparticles carrying growth factors (22, 23). Although, the approach has merit, often the use of large doses of signaling molecules such as BMP-2 can induce complications of severe side reactions that can pose significant risks (24, 25).

1.2.3 Recent development in orthopedic biomaterials

Calcium phosphate bone cements (CPCs) have been used as bone scaffold or bone void fillers in clinics due to their similarity with the inorganic mineral component of bone tissue (26). Unfortunately, calcium phosphate (CaP) alone does not mimic the mechanical properties of mineralized bone tissue. The composites of biopolymer and ceramic are reported to exhibit improved mechanical stability and tissue interaction (27). Compression screws and medical scaffolds of biodegradable polymer-ceramic composite have been approved by the U.S. Food and Drug Administration. As alternatives to inert metal devices, these devices have been available for the patients for more than 5 year. However, clinical studies did not show any significant difference of clinical outcome between bioabsorbable polymer screws and biocomposite screws (28). Moreover, the use of biodegradable composite was not as robust as biometals in bone fixation due to the low mechanical strength.

Polyetheretherketone (PEEK) and polyetherketoneketone (PEKK) have been developed for their enhanced mechanical properties (see Table 1.1) to replace titanium or stainless steel in bone applications (29) (30). PEEK and PEKK are non-degradable polymers that result in no acidic degradation products. These inert polymers with excellent mechanical strength can resolve the stress shielding and potential metal ion release of titanium or stainless steel.

In recent years, effort has been made to minimize the stress shielding effect of titanium by adjusting the Young’s modulus of Ti. By employing porous designs or altering the crystallographic phase, a decrease in Young’s modulus of titanium has been achieved to cause less stress shielding effect in bone fixation (31-33). However, despite this, the immuno-inflammatory response issues of titanium implants due to the inert biological properties of Ti will still persist and is not anticipated to be resolved by both methods.

1.3 NEED FOR BIODEGRADABLE METALS

As outlined above, in current clinical practice, biodegradable polymers are used to design degradable orthopedic devices such as interference screws, ACL screws, and fracture fixation devices. However, the initial strength of these polymers is lower than the natural human bone and degradation products of the polymers can cause undesired swelling in the long term (34, 35).

Resorbable calcium phosphate (CaP) as mentioned above, is another viable clinical option preferred for vertebral compression fractures (36). Injectable form of calcium phosphate has been shown to provide a versatile solution (37). However, the degradation rate and mechanical stability are not sufficient to warrant its widespread use replacing the currently used preferred embodiment of bio-inert metallic implant devices. Of late however, the concept of degradable metallic systems in particular, magnesium (Mg) and magnesium (Mg) alloys has received considerable attention with meteoric rise in the sheer volume of research publications over the last few years. Magnesium alloys exhibits the density and mechanical properties similar to human bone (see Table 1.2).

Table 1.2 Physical and mechanical properties of various implant materials in comparison to natural bone (38).

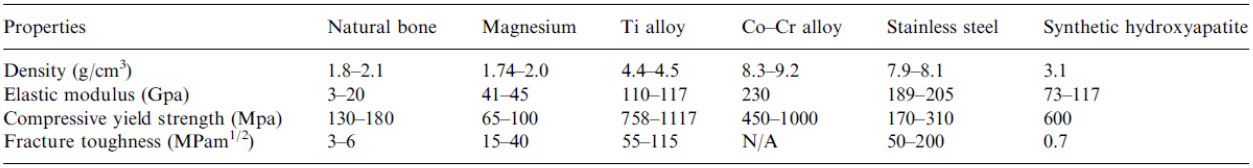

Properties	Natural bone	Magnesium	Ti alloy	Co–Cr alloy	Stainless steel	Synthetic hydroxyapatite
Density (g/cm^3)	1.8–2.1	1.74–2.0	4.4–4.5	8.3–9.2	7.9–8.1	3.1
Elastic modulus (Gpa)	3–20	41–45	110–117	230	189–205	73–117
Compressive yield strength (Mpa)	130–180	65–100	758–1117	450–1000	170–310	600
Fracture toughness (MPam$^{1/2}$)	3–6	15–40	55–115	N/A	50–200	0.7

Biodegradable Mg alloys therefore are expected to cause minor stress shielding effect and also lead to minimal cytotoxicity from the degradation products since the primary by product of degradation is $Mg(OH)_2$ which is easily excreted through the urine and feces (39, 40). Therefore, the development of biodegradable metal implants to overcome the limitations of current clinical solutions is of high interest in the field of orthopedics and regenerative medicine. With the current use of state of the art inert metallic implants, adult patients are likely to undergo secondary removal surgery only in the event of any undesirable complication. On the other hand, pediatric patients are highly likely to require secondary surgeries to remove the implants interrupting bone growth. Biodegradable Mg implant devices as mentioned above, will likely resolve the limitations of current metallic implants while keeping the advantage of higher stiffness and mechanical strength.

1.4 DEVELOPMENT OF BIODEGRADABLE MAGNESIUM

Biodegradation of Mg-based alloys has been demonstrated *in vivo* using animal models showing the degradation and replacement of the implanted devices with recovery of bone tissue (41-44). Research in the field of biodegradable Mg-based alloys is recently gathering much attention due to the possible advantage of promoting bone growth and avoiding painful second surgery as outlined above. Despite the significant interest and much progress made in the field of Mg alloys for biological applications there is still a need for improvement in biodegradable Mg alloys particularly, due to the highly reactive nature of Mg resulting in rapid corrosion in the body environment resulting in generation of hydrogen gas causing gas pockets in and around the implanted region of the animal. Much of the research that is being carried out involves controlling the rapid corrosion of Mg and Mg alloys to prevent hydrogen gas evolution and consequently the onset of premature mechanical failure. Additionally, demonstration of the biocompatibility of biodegradable magnesium and validation of the completely non-toxic nature of all of the alloying elements in the final implanted alloy is another hurdle that needs to be overcome for the technology to make the much needed translation to bring the technology to the clinics.

Hence, over the past decade or so the field has witnessed a phenomenal growth largely focused at designing new alloy systems that can be considered safe exhibiting the desired degradability and the much needed device efficacy in the implanted tissue site. In addition to alloy development, another component of Mg alloys that has received vibrant interest is the area of coatings and surface engineering strategies to control the corrosion of Mg. In this regards, calcium phosphate (45-48), use of various polymers (49), and the development of passivation layer (50-53) coatings have been researched to augment corrosion resistance of the biodegradable Mg alloys. Despite much advances made, further studies are still very much needed to accomplish the degradation of Mg implant devices to prevent hydrogen gas evolution and the accompanying mechanical failure.

1.4.1 Magnesium Alloys: State of the art

As mentioned above, there has been considerable progress in the area of degradable Mg alloys over the past decade. In particular, there have been advances made in clinical translation arena as well. Accordingly, human clinical trials have been reported to date for 3 biodegradable Mg-based devices; a cardiovascular stent from BIOTRONIK (Berlin, Germany), a compression screw from Syntellix (Hannover, Germany), and a bone screw from U&I Corporation (Uijeongbu, South Korea), schematic of which is shown in Figure 1.3. A common aspect in all these three cases is that these biodegradable Mg-based devices have demonstrated their biosafety and efficacy in the clinical trials and have all obtained regulatory approvals in Europe and South Korea.

BIOTRONIK has been developing a drug eluting absorbable metal scaffold (DREAMS) made of a magnesium-based alloy containing 93% of pure magnesium and 7% of rare earth elements (54). The first generation of DREAMS is named as BIOSOLVE-I and has been tested in 46 human patients. In the first round clinical trial, BIOSOLVE-I exhibited good biocompatibility and angiographic performance (55). The second generation of DREAMS, BIOSOLVE II, involves a modified design to add tantalum radiographic markers combined with replacement of Paclitaxel with Sirolimus for drug delivery. The testing of the BIOSOLVE-II platform technology has led to recruitment of more than 100 patients for the next clinical trial (56).

Figure 1.3 Biodegradable Mg-based medical devices used in clinical trials.

Syntellix obtained the CE mark of approval for MAGNEZIX bone compression screw in 2014. MAGNEZIX compression screw is manufactured using the metal injection casting of Mg-Y-RE-Zr alloy powders (57). The clinical trial for MAGNEZIX was performed using titanium screw as the control. 26 patients were accordingly involved in the trial and there were no significant differences noted in the clinical outcome between the patient group with MAGNEZIX screw and the other group with titanium screw (58). Also, no elevated magnesium level was observed in the blood, urine, and renal analysis with no adverse effect being reported as well.

1.4.2 Preferred alloying element for magnesium alloys

In keeping with the concept of development of new compositions for controlling the corrosion of the Mg alloys, various alloy systems including Mg-Zn (59-62), Mg-FAl (49, 63-65), Mg-Y(66, 67), and Mg-Y (67-70) have been investigated to date. The purpose of adding alloying elements to Mg as discussed earlier is mainly to increase the corrosion resistance and mechanical properties of pure Mg. Combination of different alloying elements results in a synergy that favorably affects both corrosion and mechanical properties.

Aluminum (Al) is the most effective alloying element considered to date for Mg alloys. It improves the strength, hardness, and ductility. Commercial Mg-Al alloys contain up to 9 wt. % of Al in most cases and these alloys have been investigated as potential biodegradable Mg alloys for implantable devices. Although aluminum is a favorable alloying element for Mg alloys, a constant exposure is reported to cause renal function impairment and bone disease (71, 72). Higher concentration of aluminum is also observed in brain tissues of the patients with Alzheimer’s disease (73). The effect of aluminum exposure on neuropyschiatric symptoms is being researched to identify any significant correlation (74). There has therefore been considerable negative attributes to the role of Al additions to Mg. Hence, it is essential that complete local and systemic safety of aluminum has to be first demonstrated prior to the use of Mg-Al alloys as biodegradable metal.

Zinc (Zn) is also the second most effective alloying element and often used with aluminum in commercial alloys such as AZ31 and AZ91. Zinc can improve precipitation hardening and strength at room temperature (75). Zinc can also reduce the corrosive effect of impurities such as iron and nickel (76). Mg-Zn-Zr system is thus a commercial alloy series that has been explored and considered for good strength and corrosion resistance characteristics. Thus, it is also widely investigated as a potential biodegradable metal.

Yttrium (Y) is an effective alloying element that is often alloyed with zirconium and other rare earth elements such as neodymium, cerium, lanthanum, and etc. Mg-Y based alloys are comparable to Mg-Al and Mg-Zn alloys in terms of corrosion resistance (77) and mechanical properties (78). In this family, WE43 is one of the most widely used form of Mg-Y alloys and there are two CE-marked biodegradable devices made of WE43 that are already deployed in European clinics.

In contrast to the above insoluble iron, nickel, and copper are regarded as impurity ions that are known to negatively affect the properties of Mg alloys.

1.4.3 Importance of post-processing

In addition to alloy design strategy implemented during melting and casting post processing methodologies such as heat treatment and engineered bulk processing are also used to improve the quality of the Mg alloys. It is well-known that microstructure of Mg alloys is highly correlated with the mechanical properties and corrosion resistance of the Mg alloys. Thus, the post-processing methods accordingly are focused on altering the microstructure of biodegradable Mg alloys to fulfill the required properties desired depending on the different medical device applications.

Heat treatment of Mg alloys is focused primarily on homogenizing the alloying elements within the parent Mg matrix phase. Segregated alloying elements are often embedded in the parent Mg matrix phase, or present along the grain boundary. These segregated precipitates or secondary phase(s) can induce galvanic corrosion with the primary Mg matrix phase due to their difference in electrochemical work potentials. Thus, in order to homogenize the Mg alloys, heating time and temperatures need to be suitably altered and optimized depending on the alloying element. Although heat treatments can increase the grain size of the alloys, the approach is routinely employed to improve solubility of the alloying elements and thus purify and refine the grains and the grain boundaries to enhance corrosion resistance while also simultaneously improving the ductility.

Equal channel angular pressing (ECAP), extrusion, combined with hot and cold rolling shown in Figure 1.4 are three most popular bulk processing techniques employed to improve the corrosion and mechanical properties of these alloy systems (79, 80). These processing methods are often applied to heat-treated Mg alloys to reduce the grain size. Grain size reduction is well-correlated with mechanical strength of Mg alloys. This is normally achieved by using the Hall-Petch relation which explains that grain boundaries of crystalline solids act as pinning points to impede dislocation movements, thus correspondingly influencing the yield strength. Hence, grain size reduction via post processing in the bulk enhances mechanical strength of Mg alloys. In addition, improved corrosion resistance has been reported to be achieved due to the elimination of casting defect such as voids or suitably modifying the dislocation density following bulk processing methods such as extrusion (81).

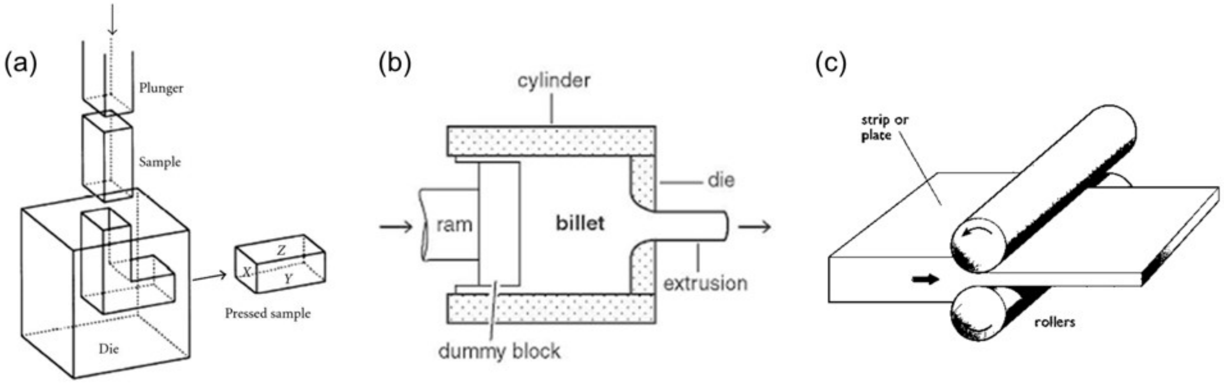

Figure 1.4 Bulk working methods such as (a) ECAP, (b) extrusion, and (c) rolling for magnesium alloys.

1.5 MAGNESIUM-ZINC: A USEFUL BIODEGRADABLE METAL

Magnesium metal was first discovered in 1880. The metallurgy of magnesium metal has since advanced with identification of suitable alloying elements that have been widely researched primarily with the goal to exploit the low atomic weight of magnesium to develop a class of light-weight materials for a variety of structural applications including the automotive space. Hence, it was logical to explore some of these commercial alloys to demonstrate the use of magnesium as biodegradable implant material. Aluminum is known as the most effective alloying element in Mg alloys. Consequently, aluminum-containing alloys (Mg-Al) such as AZ31, AZ91, and etc. have been primarily developed and used for light-weight structural materials. Mg-Al based alloys exhibit suitable corrosion resistance and mechanical properties in both, *in vitro* and *in vivo* experiments. Similarly, alloying of Mg with various rare earth elements has demonstrated improvement in corrosion resistance and the associated mechanical properties. There are therefore rare-earth element containing (Mg-RE) alloys such as LAE224 and WE43. Thus, Mg-Al (49, 63-65) and Mg-RE (67-70) based alloys that have been intensely researched as degradable metallic biomaterials and have presented much promise for their use in medical devices. However, the various neurotoxic effects of aluminum (72-74) and the large knowledge gaps related to the known biological effects of rare earth element (82) in the human body make it questionable for these systems to be ubiquitously used for biological applications until much research is conducted to unequivocally demonstrate their biocompatibility and biosafety.

On the other hand, the Mg-Zn alloys have been widely studied as degradable metallic biomaterials and exhibit much less toxicity concerns compared to Mg-Al or Mg-RE. Zinc is known to be biocompatible with the recommended daily allowance of 11 mg (83) and is an effective alloying ingredient that improves room-temperature strength overcoming the unfavorable corrosive effect of impurities (84, 85). Zinc content up to 5% by weight is known to cause grain boundary, solid solution, and the secondary phase strengthening which results in improved corrosion resistance and desired enhanced mechanical properties (75). In a recent study, Mg-Zn alloys have exhibited considerable new bone formation after implantation in the femoral cavity of a rabbit model (59). Further, murine osteoblastic cells cultured on Mg-Zn alloys, in comparison to PLLA, have also exhibited an improvement in mRNA expressions of collagen type lαl and osteocalcin (59).

1.6 STRONTIUM AND CERIUM: POTENTIAL MICRO-ALLOYING ELEMENTS FOR BONE REGENERATION

As mentioned above different alloy systems have been researched and studied for a variety of biological applications. Similarly, different types of coatings have also been researched widely to improve the corrosion resistance of Mg alloys (48, 50, 52, 86-88). Drug eluting coating have been also proposed and studied to enhance the regeneration of wounded tissue. However, polymeric or ceramic coatings that can load drug molecules do not exhibit enough mechanical stability on the alloy surface. Use of different alloying elements in Mg alloys to control the mechanical and corrosion properties is a much more preferred approach. During the degradation of Mg alloys, the release of ions of alloying elements at the local wound site can significantly affect the wound healing and bone regeneration process. Strontium (Sr) is widely studied for its effect on the differentiation of bone cells such as osteoclasts and osteoblasts. It is also known to promote the replication of pre-osteoblastic cells and activity of osteoblasts (89). Further, Sr also reduces the differentiation of osteoclasts to enhance bone formation (90). Similarly, Cerium (Ce) has shown its ability to influence the osteogenic differentiation of hMSC (91, 92) while improving the stability of the corrosion protective layer following initial corrosion (87).

Both Sr and Ce thus have significant merit as alloying elements if the release of these ions following the degradation of Mg alloys for medical devices can stimulate bone fracture repair. The ability to accelerate bone fracture repair and new bone formation using biodegradable fracture fixation devices will motivate further studies in device design, degradation control, biomechanics, etc.

Accordingly four specific aims have been designed revolving around various alloy systems and study their materials characteristics combined with *in vitro* and *in vivo* response particularly for orthopedic related applications. Specific Aim 3 in particular, will be focused on systematically studying the *in vitro* characteristics of Sr and Ce containing Mg alloys. The bone regeneration effect will also be investigated using *in vitro* mineralization and alkaline phosphatase assays.

2.0 THESIS GOALS

2.1 SPECIFIC AIM I

Processing and optimization of the Mg-Zn-Zr alloys

Rationale: Mg-Zn-Zr alloys have been studied and developed for corrosion resistant lightweight structural applications to replace some steel and aluminum materials. Its corrosion resistance and favorable mechanical properties are essential characteristics for biodegradable metal application and hence the system is clearly worthy of further investigation. Before characterizing the corrosion resistance, mechanical properties, and biocompatibility, it is crucial to investigate the optimal processing conditions to obtain a high quality Mg alloy with low impurities and desired microstructure. Low impurities and microstructure directly correlate with corrosion and mechanical properties. Impurities such as ion (Fe), nickel (Ni), and copper (Cu) as mentioned earlier, serve as a nucleation site for initiating corrosion and causing pitting corrosion which leads to heterogeneous degradation of the biodegradable Mg alloys. Micro structure also plays a key role in determining the mechanical properties of Mg alloys. Processing conditions such as melting temperature, settling time, heat treatment techniques, and impurity level of pure ingots essentially control the quality of Mg alloys in terms of impurities and microstructure. Therefore, processing conditions were investigated in detail essentially to have control on the impurity levels and on the microstructure to calibrate the integrity of Mg alloy assessment in terms of achieving acceptable corrosion resistance, mechanical properties, combined with cytocompatibility as well as biocompatibility.

Experimental Design: This involved the following various steps as outlined below.

Conventional melting and casting: High-purity pure Mg (US Magnesium, 99.97%), Zn (Alfa aesar, 99.99%), and Zirmax (Mg-33Zr master alloy, Mg Elektron, Commercial grade) were used for producing Mg-4 wt.% Zn-0.5 wt.% Zr (ZK40) alloy to minimize the impurity level in the final alloy ingot. Pure Mg, Zn, and Zirmax were weighed and melted in a stainless steel crucible using an electrical resistant furnace at 700^o C under protective atmosphere. The molten metal was stirred using a stainless steel rod, allowed to set for 30 minutes, and cast in a mild steel mold preheated at 500^o C. Following melting and casting of the alloys, 1 cm from the top, bottom, and side of the cast ingots were correspondingly removed, and the remaining piece of ingots were used to minimize the probability of retention of voids and impurities resulting from the melting and casting processes.

Post processing: Solution treatment was mainly investigated to solubilize the solutes into α-Mg matrix in the microstructure of ZK40 alloy. Based on the Mg-Zn binary phase diagram, a eutectic composition of Mg_7Zn_3 at 325 °C transforms into α-Mg and MgZn intermetallic during solidification. The Mg_7Zn_3 composition is known to undergo eutectic transformation below 325^oC forming α-Mg(Zn, Zr) solid solution and MgZn intermetallic which can exist as the second phase precipitates nucleating along the grain boundaries. As mentioned above, these second phase precipitates are undesired from the corrosion point of view contributing to galvanic corrosion albeit serving to improve the mechanical strength. The accelerated corrosion however outweighs the advantages of mechanical strengths and hence is undesired. Since the T4 treatment comprises heat treatment conducted above 325 °C, this can lead to unwanted second phase precipitation which is undesirable as mentioned above and grain growth which is also not desirable since large grains can contribute to lower mechanical strengths. Thus the ZK40 alloy were correspondingly heat-treated at 300 °C for 1 hour followed by quenching in silicon oil to suppress the precipitation of these undesired secondary phases.

Phase and microstructure characterization: X-ray diffraction (XRD) was performed to determine the phase(s) formation using Philips X'Pert Pro system employing the CuKα (λ=1.54056 Å) radiation operated at 45 kV and 40 mA at 2θ range of 10-80°. Alloy specimens were mounted in epoxy resin and polished using 9, 3, 1 µm diamond slurry, and 0.5 µm colloidal silica slurry to obtain mirror finish surface. Polished surface were imaged using back-scattered scanning electron microscopy (SEM) to observe the microstructure and precipitates. Energy-dispersive spectrometry (EDS) probe was used along with SEM to analyze the elemental content of precipitates and grain matrices. Finally, polished surface were etched and observed using optical microscopy to obtain the optical microstructure images.

Impurity characterization: Impurities in ZK40 alloys were analyzed using inductively coupled plasma-optical emission spectroscopy (ICP-OES, iCAP duo 6500 Thermo Fisher, Waltham, MA) to confirm the real chemical composition of the as-cast ingots. Melting process can alter the final composition of the cast ingots due to evaporation and oxidation. Also, the presence of Fe, Ni, and Cu as mentioned earlier, can elevate the corrosion rates of Mg alloys. Therefore, ICP-OES measurement of ZK40 was performed utilizing Mg, Zn, Zr, Fe, Ni, and Cu as standards. The content of precipitation along the grain boundary observed in back-scattered SEM microstructure analysis was assessed using EDS probe attached to SEM to check if unwanted impurities exist.

Statistical Considerations: Grain sizes of ZK40 alloy after different heat treatment condition will be analyzed using the t-test. The content of impurity levels from ICP analysis was saved for ANOVA analysis with corrosion rates as a dependent variable among the different batches, if batch to batch corrosion rates are observed to be very different. These statistical analyses were performed using Statistical Packages for Social Studies (SPSS) 17.0 (IBM). The results were correspondingly judged for significance at $p < 0.05$.

Anticipated Results: Single phase form of Mg, α-Mg with restricted precipitation of the second phase is anticipated in the microstructure of the as-cast ingot. Correspondingly, low impurity levels (less than 20 ppm) for Fe, Ni, and Cu are also anticipated. Grain growth is also restricted to be in the size range lower than 100 µm to preserve the mechanical strength. Melting temperature, protective gas, heat treatment temperature and duration were thus investigated to optimize the impurity level and achieve the desired microstructure. Results of these studies are discussed in Chapter 3. Processing conditions were also correlated with corrosion resistance, mechanical properties, and biocompatibility in Specific Aim 2 and further optimized during the development of the biodegradable Mg-Zn based alloy which are discussed in Chapters 4 and 5.

2.2 SPECIFIC AIM II

Identification of the potential of Mg-Zn based alloys as a biodegradable system using in vitro characterization methods

Rationale: Corrosion resistance, mechanical properties, and biocompatibility are three primary criteria required to be assessed comprehensively to prove the safety and function of biodegradable Mg alloy for orthopedic application. *In vitro* assessment of biodegradable Mg alloys is designed to focus on mimicking the physiological environment and replicating the trend of in vivo degradation of the different Mg alloys. Pure Mg and various commercial Mg alloys such as AZ31 and WE43 have been reported to exhibit suitable corrosion resistance, mechanical properties, and biocompatibility in the initial stages of *in vivo* and *in vitro* experiments. Thus, pure Mg and AZ31 are good negative controls for assessing the *in vitro* characteristics of ZK40 alloy and the result can determine the need for *in vivo* studies to understand the ZK40 alloy better. Understanding *in vitro* corrosion resistance, mechanical properties, and cell cytotoxicity of ZK40 will provide useful direction in developing Mg-Zn based alloys for orthopedic applications.

Experimental Design: This will involve conducting several systematic studies as outlined below under various categories.

Corrosion measurement: Corrosion measurement of biodegradable Mg alloys can be achieved using different methods such as mass loss immersion, hydrogen evolution, electrochemical impedance spectroscopy (EIS), and potentiodynamic polarization (PDP). In this study, mass loss immersion and potentiodynamic polarization (PDP) were performed to assess the corrosion characteristics at different time points. Mass loss immersion has also exhibited similar trend of Mg alloy degradation compared to what is observed in *in vivo* subcutaneous implantation models. The specimens were immersed in cell culture media using a fishing line at 37.4 °C in a humidified atmosphere with 5% CO_2. Media volume to surface area ratio was maintained at 20 ml/cm^2 according to the ASTMG31-72 standard. Samples were removed after 1, 2 and 3 weeks of immersion, rinsed with distilled water and dried at room temperature. Further, the corrosion product layer of samples were cleaned with a solution mixture of chromic acid and $AgNO_3$. The difference in weight after immersion will be recorded, and the degradation rates (in units of mm/year) were obtained according to ASTMG31-72.

Potentiostatic dynamic polarization (PDP): PDP was performed to measure the electrochemical stability of bare metal surface of Mg alloys. A three electrode cell setup was employed for the electrochemical corrosion test using platinum as the counter electrode, Ag/AgCl as the reference electrode, and the epoxy mounted sample as the working electrode. The tests were performed in the same culture media at pH 7.2 ± 0.2, held at 37.4 °C. Before each measurement, the sample was immersed in the media for 15 min at open circuit potential (OCP) to provide voltage stability. The cathodic and anodic branches of the generated Tafel plots were extrapolated linearly to calculate corrosion potential, Ecorr, and corrosion current density, icorr.

Mechanical testing: Tension and compression tests were performed in accordance with ASTM standard practice for tensile testing ASTM-E8-04 and compressive testing ASTM-E9-09 at room temperature. For the tension tests, standard dog bone specimens of 12.7 mm in gauge length and 3 × 3 mm in gauge cross-section were machined and pulled to failure employing a cross-head speed of 1.3 mm/min. Specimens for compression test corresponded to dimensions of 10 mm diameter and 20 mm in length. The specimens were accordingly machined from the long axis of the ingots and loaded to failure at rate of 2mm/min. Tensile and compressive stress-strain curves were utilized to determine the yield strength (YS), ultimate tensile strength (UTS), Young's modulus (E) during tension, total elongations (%), compressive yield strengths, and total compression (%) of each alloy specimens.

Cell cytotoxicity: The mouse osteoblast-like cell line MC3T3 were cultured in Dulbecco's modified eagle medium (α-MEM) with 10% fetal bovine serum (FBS) and 1% p/s at 37.4 °C in a humidified atmosphere of 5% CO_2. Cells were seeded onto specimen surfaces and cultured for 72h. The live/dead assay were performed subsequently with commercially available kit and fluorescence microscopy was used to determine the viability/cytotoxicity of cells. After fluorescence imaging, cells on the specimens were fixed by 2.5% glutaraldehyde and dehydrated by ethanol. Fixed cells were imaged by scanning electron microscopy after palladium sputtering. MTT(3-(4,5-Dimethylthiazol-2-yl)-2,5-diphenyltetrazolium bromide) assay was used to assess the cytotoxicity of degradation product after 72 h immersion of specimens in culture medium. Extract media in dilution of 1x, 2x, 4x and 10x were added to the 24 h cultured MC3T3 cell and MTT assay will be performed after 72h.

Statistical Considerations: One-way ANOVA with graphical and summary statistics was used to assess the degradation rates, mechanical properties, and cell cytotoxicity results. MTT cell cytotoxicity test were normalized by the negative control (cell culture plastic) to compare the cytotoxicity levels between the different alloy groups. Cell count of live/dead assay images were accordingly examined using the ImageJ software to add more justification to the analyses.

Anticipated Results: In comparison to pure Mg and as-drawn AZ31, ZK40 alloy is expected to exhibit comparable characteristics to pure Mg and AZ31 with respect to degradation rates. Pure

Mg and AZ31 are reported to have good corrosion resistance and as-cast and heat-treated ZK40 alloys are anticipated to perform similarly. In terms of mechanical properties, ZK40 alloys are expected to perform better than pure Mg. However, ZK 40 alloys are not expected to match the mechanical properties of commercial as-drawn AZ31 since the drawing technique will have a significantly higher level of grain refinement. Cell cytotoxicity result of ZK40 alloy on the other hand, is anticipated to perform better than AZ31 and as good as pure Mg following both MTT and live/dead assays. Results of these studies are discussed in Chapter 4.

2.3 SPECIFIC AIM III

Effects of addition of Sr and Ce on the degradation, mechanical and biological properties of Mg-Zn-Zr alloys

Rationale: As discussed above for the each alloy category, a new class of system considered here is alloys containing Sr and Ce. Both Sr and Ce as discussed earlier, naturally exist in bone and have been reported for their biological effect in terms of hMSC differentiation for bone. On the other hand, Sr is known to have grain refining effects while Ce is known to help form a stronger metallurgical corrosion protection layer on Mg alloy, thus significantly improving the quality and expected performance of the resultant alloy. Release of Sr and Ce during degradation of Mg alloys has potential to thus further enhance the regeneration of bone tissue. Therefore, small but nevertheless noticeable amounts of Sr and Ce as alloying elements have been added to the base Mg-Zn based alloy to study the effect of these elements. The amounts of Sr and Ce addition are thus fixed as 0.25 and 1 wt. %, to systematically investigate the correlation between the amount of the addition and the key three properties, as well as the bone forming ability.

Experimental Design: Mg-Zn-Sr-Zr and Mg-Zn-Ce-Zr (Sr, Ce = 1, 0.25) alloys were melted and casted utilizing the same experimental setup as described in Specific Aim 1. Sr and Ce were accordingly added during melting, using Mg-Sr and Mg-Ce master alloy. Heat treatment conditions were optimized after microstructure and impurity analysis using SEM. After the processing parameters are determined, the *in vitro* corrosion, mechanical, and biological properties measurements were performed following the experimental design of Specific Aim 2 to understand the basic characteristics required for biodegradable Mg alloy.

In addition, bone forming ability of Mg-Zn-Sr-Zr and Mg-Zn-Ce-Zr alloys were assessed using alkaline phosphatase, and mineralization assay. hMSC were cultured with differentiation media supplemented with Mg, Sr, and Ce ions to test the effect of degradation product without engaging direct cell attachment. The alkaline phosphates assay was normalized by DNA quantification. After 1, 2, 3 weeks of culture, the hMSC lysates was mixed with p-nitrophenyl phosphate (pNPP) solution and substrate solution, incubated and observed at the absorbance of 405nm. Mineralization of osteoblast cells was measured using alizarin red assay after 2 and 3 weeks of culture. Quantitative analysis was performed after alizarin red staining and the stained cells was dissolved for quantitation using plate reader at the absorbance of 605nm.

Statistical Considerations: The same statistical analyses from Specific Aim 1 and Specific Aim2 were employed for the repeated experiments performed on Mg-Zn-Sr-Zr and Mg-Zn-Ce-Zr alloys. Two-way ANOVA was accordingly used for ALP and mineralization studies with independent variables of the group and time. The significance level was set at $p < 0.5$ to prove if Sr or Ce addition has an effect on bone forming ability.

Anticipated Results: As outlined above, Ce and Sr addition to ZK40 alloy is not expected to deteriorate the corrosion resistance although even small amounts of these alloying elements are likely to form small precipitates along the grain boundary or inside of the parent Mg matrix phase. Mechanical properties would correspondingly change, but it is still expected to maintain 80% of the ZK40 alloy in terms of tensile strength. Mg-Zn-Sr-Zr and Mg-Zn-Ce-Zr alloys are projected to exhibit significantly higher level of ALP activity and mineralization while the cell cytotoxicity of the alloys would not be significantly different from ZK40. These results are outlined in Chapter 5.

2.4 SPECIFIC AIM IV

Rat femoral fracture repair using intramedullary pins of Mg-Zn-Sr-Zr alloy

Rationale: Biodegradable Mg-Zn alloys are anticipated to exhibit suitable degradation, mechanical properties, and biocompatibility characteristics desired for various orthopedic applications. It is well-known that depending on the load experienced by the biodegradable Mg-Zn implant device, the degradation rates will vary, and hence, the failure of the implanted device can induce a sudden inflammatory response. To demonstrate the influence of stress on the biodegradation and mineralization response of the Mg-Zn based alloy, a rat femoral fracture model is selected to investigate the biocompatibility and mineralization potential of the Mg-Zn alloy under load-bearing condition. Although the Mg-Zn alloy can be potentially used as intramedullary rod, the alloy will be implanted in the intramedullary region to support and fix a non-union resulting in healing of the fractured femur causing re-union. Correspondingly, biocompatibility of the Mg-Zn alloy and its degradation products will be assessed using blood test as well as the histology of liver and kidney. Bone healing and local toxicity will be assessed using bone histology and elemental analysis of the muscle.

Experimental Design: To demonstrate the efficacy of the alloy in the above discussed rat femoral fracture model, a single composition of the Mg-Zn alloy was judiciously selected based on the *in vitro* corrosion resistance and mechanical properties. At the same time, Ti-alloy was used as a control group to mimic the level of toxicity observed in currently used state of the art clinical biomaterial for bone fixation. Intramedullary pins were therefore machined corresponding to the same dimensions. Each pin was inserted in the intramedullary region of the right femur of each Sprague-Dawley rat after osteotomy. The animals with implant device were all sacrificed after 2, 8, and 14 weeks for assessing the biocompatibility of Mg and Ti pins.

Blood test: Whole blood samples were accordingly analyzed for complete blood count panel. Serum samples were analyzed to obtain a comprehensive picture of the metabolic and chemistry profile. The chemistry profile was used to essentially assess the level of phosphorous and magnesium in the blood.

Micro CT analysis: Micro CT imaging was also performed on the original implant and harvested bones. Degradation rates correspondingly have been calculated from the volume loss. Finally, bone healing response has been determined and assessed based on the the CT images.

Histology: Liver and kidney tissues were also correspondingly fixed using neutral buffered formalin, embedded in paraffin, and sectioned using a microtome. Hematoxylin and eosin staining was performed to examine any tissue damage or abnormal response. Harvested femurs were then subsequently processed as undecalcified bone and embedded in plastic. Embedded tissue were correspondingly sectioned and subjected to various staining methods including Goldner's Masson Trichrome and toluidine blue.

Statistical Considerations: Two-way ANOVA statistical analysis was used to determine the mean comparison of degradation rates and blood test results with regards to independent variables, time and group. The significance level was set at $p < 0.5$ to prove that Sr or Ce addition indeed have an effect on bone forming ability. Histology results were also accordingly judiciously considered to justify only the subjective positive outcome.

Anticipated Results: After 14 weeks, more than 50% volume of the Mg pins is expected to remain following degradation. Callus formation on the fracture site will also be expected to occur while helping to maintain the stability of the fixation. No significant difference between groups and time will be expected from the blood test results and histology outcome. An elevated level of Mg could be likely expected following analysis of the chemistry panel analysis. However, it is anticipated that the level will be maintained within the normal range. Results of these studies are discussed in Chapter 6.

3.0 SPECIFIC AIM I: PROCESSING AND OPTIMIZATION OF MAGNESIUM-ZINC-ZIRCONIUM ALLOYS

3.1 INTRODUCTION

For the present studies, Mg-4wt%Zn-0.5wt%Zr (ZK40) was selected based on the rationale discussed earlier in Chapter 2. Alloys were developed by permanent mold casting route and were further solution treated at elevated temperature. Elemental analysis was performed using an inductively coupled plasma (ICP) as explained in Chapter 2 to assess the final chemical contents including potential impurities. X-ray diffraction was also used to perform phase analysis. Microstructure analysis was accordingly performed using optical and back-scattered scanning electron microscopy. Energy dispersive spectroscopy technique using the equipment attached to the scanning electron microscope (SEM) was used along with back-scattered scanning electron microscopy to provide the chemical composition of the precipitates observed at the grain boundaries. Postentiodynamic polarization (PDP) measurements were also performed to identify the electrochemical corrosion properties of as-cast and solution-treated ZK40.

3.2 MATERIALS AND METHODS

3.2.1 Mg alloy melting and casting

Pure elemental ingots of Mg (US magnesium Inc. 99.97%), Zn shots (Alfa-Aesar 99.99%), were melted in a mild steel crucible inside an electrical resistance furnace (Wenesco Inc.). A typical melt size was 200 g. The melt was covered with (0.5% SF6 + balance Ar) protective gas atmosphere to prevent burning and loss of magnesium. Once the desired melting temperature (700 °C) was reached, equivalent amount of zirconium was added using Zirmax® (Mg-33.3 wt% Zr) master alloy (Magnesium Elektron Ltd.). The liquid melt after zirconium addition was stirred for 10 s after 1 min and 5 min intervals to dissolve and disperse the zirconium particles uniformly into the melt. Further, the melt was held for 30 min at 700 °C and then poured into a preheated mild steel mold (Ø 44.5 mm × 82.5 mm) at 500 °C.

3.2.2 Heat treatment

The as-cast ingots obtained were solution treated (T4) at 300 °C for 1 h inside a tubular furnace covered with magnesium powder as a getter under protective atmosphere of Ar and SF_6 and then quenched into water.

3.2.3 X-ray diffraction

The alloys were characterized for phase(s) formation using x-ray diffraction. Accordingly, x-ray diffraction (XRD) was performed using a Philips XPERT PRO system employing CuK$_\alpha$ (λ=1.54056 Å) radiation operated at 45 kV and 40 mA in the 2θ range of 10-80°.

3.2.4 Microstructure analysis

The microstructure of as-cast and solution treated (T4) ZK40 alloys were observed using optical microscopy (Axiovert 40 MAT, Carl Zeiss, Jena, Germany). Square specimens were mounted in epoxy (EpoxiCure, Buehler), and mechanically polished using 9, 3, and 1 µm diamond slurry followed by 0.5 µm colloidal silica to obtain a mirror-like finish using semi-automatic polishing system (Tegramin-20, Struers, Ballerup, Denmark). Specimens following polishing were chemically etched in a solution of 5 mL acetic acid, 6 g picric acid, 10 mL water, and 100 mL ethanol and washed immediately using isopropanol to clearly reveal the grain boundaries. Grain size was calculated according to ASTM E112 (93) linear intercept method, and the ASTM grain number G was converted to average grain size. The alloys were further characterized to observe the presence of voids/impurities/oxide scales using computerized nano-tomography. Correspondingly, nano computed tomographic (nanoCT) images were captured using the Phoenix Nanotom-m 180 kV / 15 W X-ray nanoCT® system equipped with a tungsten filament. Disk samples of 1.5 mm dia × 3mm height was sectioned from the as-cast Mg-4%Zn-0.5%Zr alloy and nanoCT images were captured with a minimum voxel resolution ~ 300 nm to delineate the finer details of the microstructures.

3.2.5 Elemental analysis

The alloy nominal compositions, determined by inductively coupled plasma optical emission spectroscopy (ICP-OES, iCAP duo 6500 Thermo Fisher, Waltham, MA), are listed in Table 3.1.

Table 3.1 Chemical composition of Mg-4wt%Zn-0.5wt%Zr (ZK40) alloy.

Alloy	Chemical compositions (wt.%)							
	Zn	Zr	Cu	Fe	Mn	Ni	Si	Mg
Mg-4Zn—0.5Zr	4.28 ± 0.11	0.36 ± .008	0.014	0.002	0.003	0.018	0.007	Balance

3.2.6 Potentiodynamic polarization (PDP) measurement

Potentiodynamic polarization (PDP) test was carried out with an electrochemical workstation (CHI 604A, CH Instruments, Inc., Austin, TX) at a scanning rate of 1 mV/s and potential window of ~500 mV above and below the open circuit potential (OP). Square samples (surface area ~ 1cm^2) were connected to a copper wire using silver epoxy, mounted in epoxy resin. The mounted samples were mechanically polished using 320, 600, and 1200 grits SiC papers, sonicated in isopropyl alcohol, and dried in air. A three electrode cell setup was employed for the electrochemical corrosion test with platinum being the counter electrode, Ag/AgCl as the reference electrode, and the epoxy mounted sample as the working electrode. The test was performed in Dulbecco's Modified Eagle Medium (DMEM, with 4.5 g/l glucose, L-glutamine, and sodium pyruvate, Cellgro, Manassas, VA) supplemented with 10% fetal bovine serum (FBS), 100 U/ml penicillin, and 100 μg/ml streptomycin at pH 7.2 ± 0.2 and temperature held at 37.4 °C. Before each measurement, the sample was immersed in DMEM for 15 min at open circuit potential to provide voltage stability. The cathodic and anodic branches of the generated Tafel plots were extrapolated linearly to calculate the corrosion potential, E_{corr}, and corrosion current density, i_{corr}. Average and standard deviations of these 3 sample measurements are reported and one-way ANOVA was used to determine any significant mean differences with a p-value less than 0.05. Corroded samples following the test measurements were subsequently cleaned by immersion in 200 g/L of chromic acid and 10 g/L of $AgNO_3$ solution for 10 min at ambient temperature to remove the corrosion products (94) and the corrosion surface was then characterized using scanning electron microscopy (SEM).

3.3 RESULTS AND DISCUSSION

3.3.1 Phase analysis

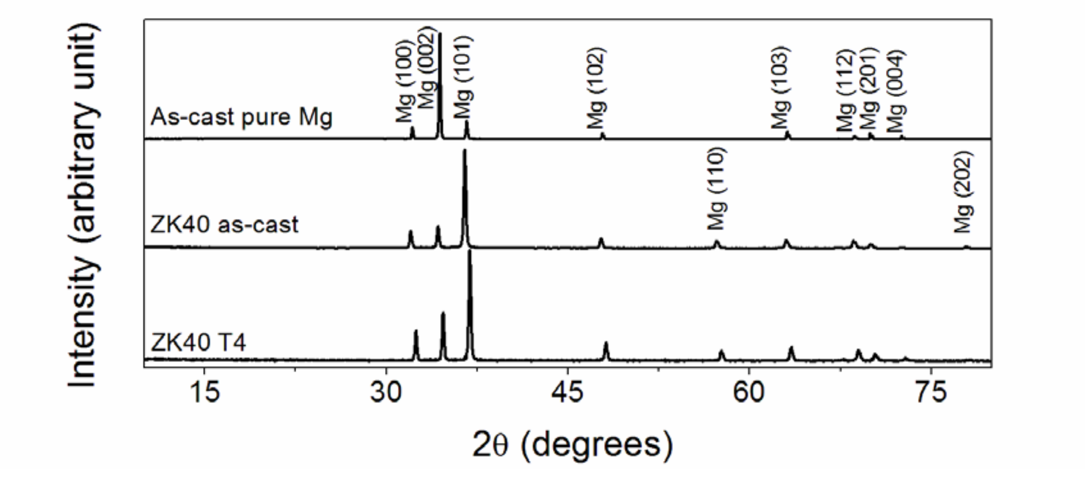

Figure 3.1 X-ray diffraction patterns collected on pure Mg, ZK40 as-cast, and ZK40 T4-treated alloys.

Figure 3.1 show the X-ray diffraction (XRD) patterns of the pure Mg, Mg-4%Zn-0.5%Zr (ZK40) as-cast and solution treated samples. All of the peaks were indexed to single phase α-Mg matrix with the hexagonal close packed (hcp) crystal structure in case of Pure Mg. Interestingly, in the case of Mg-4%Zn-0.5%Zr, both for the as-cast and solution treated samples, only α-Mg peaks were found. The XRD patterns thus clearly show that the α–Mg(Zn, Zr) solid solution single phase was formed during solidification which should be observed in the final microstructure. However, the highest diffraction peak intensity observed corresponded to the (101) pyramidal plane which suggests that the orientation of the α–Mg(Zn, Zr) solid solution single phase was altered during melting and solidification in comparison to pure α- Mg matrix suggesting the influence of either the alloying elements or the segregated elements within the crucible containing the melt acting as nucleating sites causing preferential aligning of the solidifying elements in the preferred (101) plane.

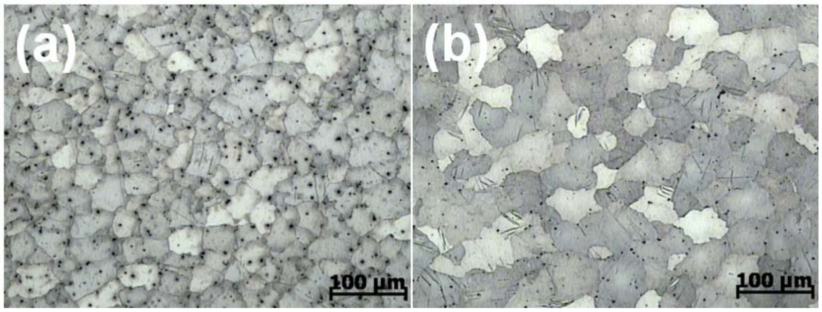

Figure 3.2 Optical micrographs of Mg-4Zn-0.5Zr (ZK40) alloys (a) as-cast and (b) T4-treated at 300 °C for 1 h.

Figure 3.2 correspondingly illustrates the optical micrographs of the as-cast and solution treated Mg-4%Zn-0.5%Zr alloys. It can be seen that the microstructures of both, the as-cast and solution treated alloys contain primary α-Mg matrix and minor secondary phase(s) precipitated along the grain boundaries. The average grain size for the as-cast and solution treated alloys were 50±10 μm and 87±10 μm, respectively. The grains were uniform and equiaxed throughout the microstructures, likely suggesting the excellent grain refinement ability of Zr inoculants added during solidification of the liquid melt (95, 96). It is well-known that Zr is an excellent grain refiner for magnesium and in the presence of solute (here zinc), the effective barrier for nucleation is likely much reduced leading to a large number of critical sized zirconium nuclei serving as active sites for nucleation, hence effectively refining the structure (97, 98). Zinc which is present as a solute also tends to segregate in the diffusion layer ahead of the solid/liquid interface of the growing grains during constitutional undercooling which helps to restrict α-Mg grains to grow further. Maxwell and Hellawell (99) and later Greer et al. (100) further showed that the grain refinement efficacy of a solute can be determined by the growth restriction factors (GRF). It has been determined that Zr and Zn have GRF values of 38.29 and 5.31 respectively, which thus together, impart a powerful grain refinement effect in the resultant alloy validating the observed microstructure(101). The slight increase in the average grain size of the T4-treated sample was likely due to coalescence of smaller grains along the triple junction grain boundary regions and eventually formation of supersaturated α–Mg(Zn, Zr) solid solution after the precipitates dissolve into the matrix. The SEM of the as-cast and solution treated alloys were also captured using back-scattered electron (BSE) mode to reveal clearly the compositional contrast due to the large difference in the atomic number of Mg with Zn and Zr. Figure 3.3(a) shows the BSE mode SEM micrograph of as-cast ZK40 alloy. It can be observed that Zn/Zr rich second phase is continuously distributed along the grain boundary regions. Energy dispersive spectra (EDS) analysis of the Zn and Zr rich second phase shown in Figure 3.3(a) identified the elemental composition of the precipitates to be Mg_7Zn_3. According to the magnesium-zinc phase diagram there exist a eutectic composition of Mg_7Zn_3 ~ 325 °C which eventually transform in to α-Mg and MgZn intermetallic during solidification (102). It is believed that Mg_7Zn_3 undergoes eutectic transformation and formed σ-Mg(Zn, Zr) solid solution and MgZn intermetallic which is the second phase observed along the grain boundaries. Similarly, in the case of solution treated

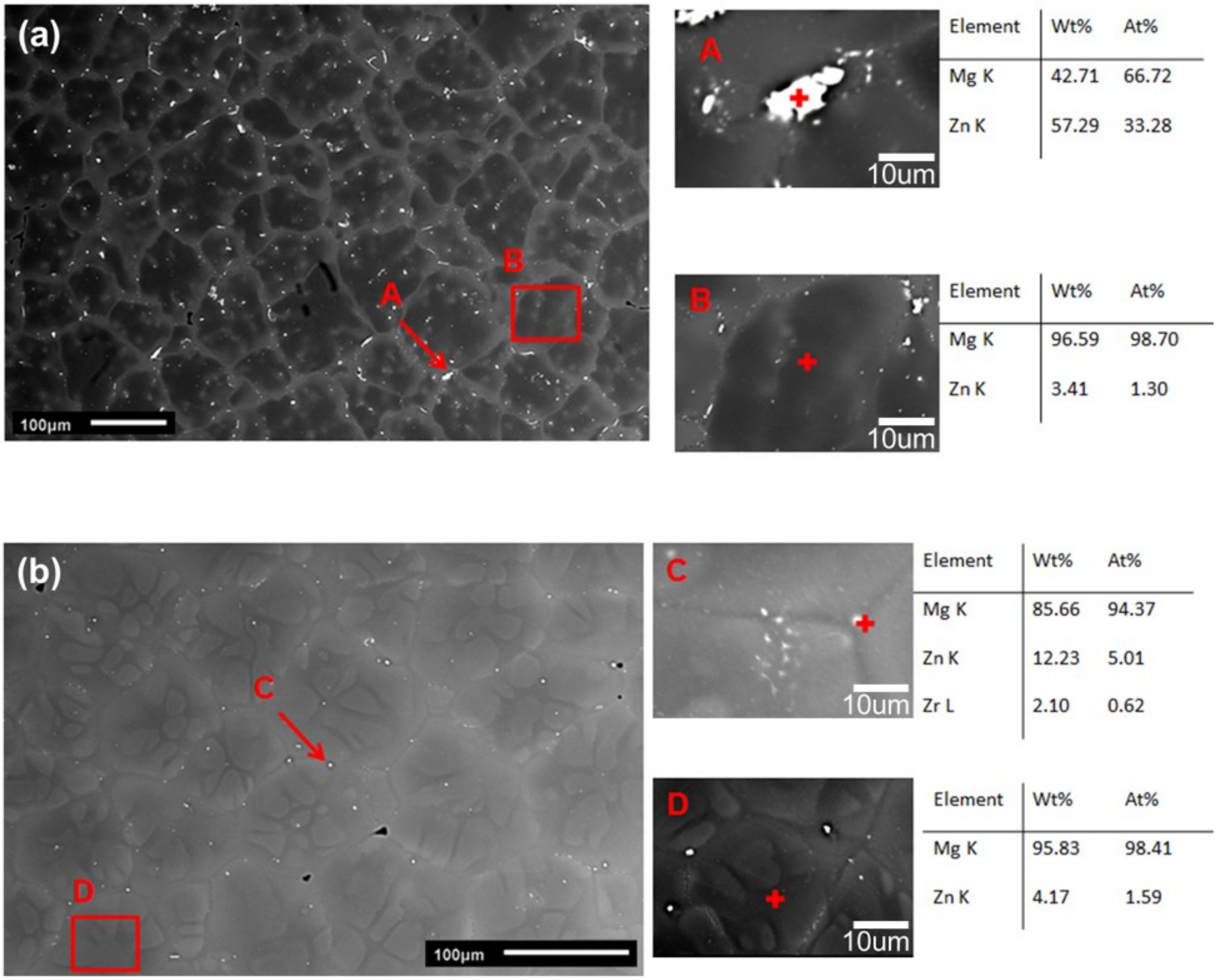

A

Element	Wt%	At%
Mg K	42.71	66.72
Zn K	57.29	33.28

B

Element	Wt%	At%
Mg K	96.59	98.70
Zn K	3.41	1.30

C

Element	Wt%	At%
Mg K	85.66	94.37
Zn K	12.23	5.01
Zr L	2.10	0.62

D

Element	Wt%	At%
Mg K	95.83	98.41
Zn K	4.17	1.59

Figure 3.3 Back-scattered mode (BSE) SEM micrographs and EDS analysis of (a) as-cast ZK40 and (b) T4-treated ZK40 alloy microstructure on grain boundary and matrix.

alloys the MgZn intermetallic was observed along the grain boundaries (see Figure 3.3b). However, the reduction in the volume percent of second phase was evident due to rapid dissolution of MgZn intermetallic in to α-Mg grain during solution treatment.

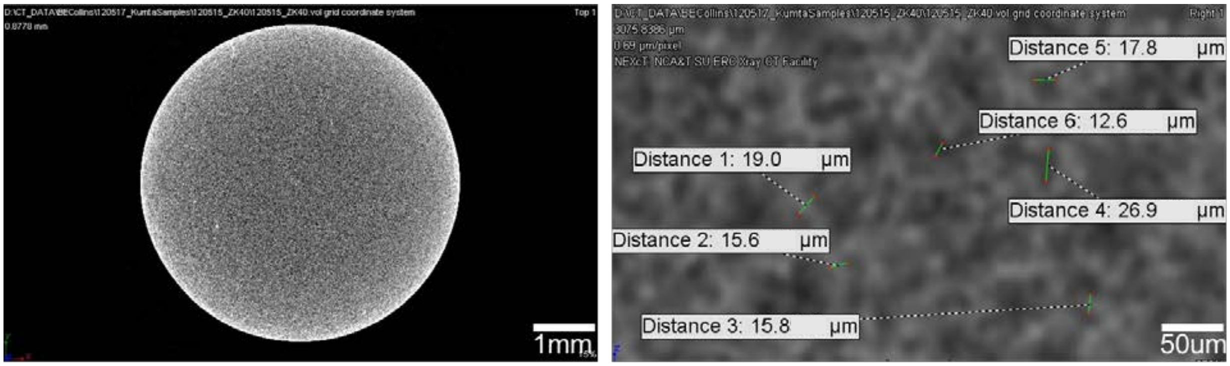

Figure 3.4 NanoCT images of as-cast Mg-4%Zn-0.5%Zr alloy, (a) top view, (b) spatially high resolution image showing distances between the interior of grains to grain boundary regions.

Figure 3.4(a) shows the nanoCT scan image of the as-cast Mg-Zn-Zr alloys. It clearly reveals the absence of any casting defects/inclusion suggesting the excellent castability of the Mg-Zn-Zr alloy composition and the cleanliness of the melting and casting approach adopted in this study. The high resolution nanoCT scan shown in Figure 3.4(b) illustrates the average distance between grain interiors to the grain boundaries. Table 3.1 also illustrates the ICP data of the alloy composition which further validates that the impurity levels of the liquid melt was very low (combined impurity levels including Fe, Ni, Mn, Cu, and Si was ~ 440 ppm) ensuring the better biocompatibility and degradation properties of this alloy in the physiological environment.

3.3.2 Tafel analysis of the potentiodynamic polarization measurement on Mg-Zn-Zr alloy

Table 3.2 Chemical composition of DMEM + FBS (mM/L) + P/S (mg/L) used for the present biocorrosion study.

Name	DMEM(L) + FBS
$CaCl_2$	200.00
NaCl	6400.00
KCl	400.00
$NaHCO_3$	3700.00
NaH_2PO_4	125.00
$MgSO_4$	97.70
$Fe(NO_3)_2$	0.10
Glucose	4500.00
Amino acid	1605.36
Fetal bovine serum	10%
Penicillin/streptomycin	1%

The potentiodynamic polarization (PDP) behavior of the ZK40 in both, the as-cast and solution treated conditions along with pure Mg and as-drawn AZ31 alloys have been studied extensively under DMEM + 10%FBS+1% P/S physiological condition. The composition of the DMEM + 10%FBS+1% P/S is listed in Table 3.2. The potentiodynamic polarization curves (Tafel plot) of the various samples and pure Mg, recorded at a scan rate of ~1 mV/s are plotted in Figure 3.5. In general, the cathodic branch of the tafel plot shows the hydrogen evolution through a reduction process whereas the anodic branch represents the magnesium dissolution by oxidation.

The cathodic plateaus of pure Mg suggest that the corrosion potential, E_{corr} for hydrogen evolution occurs at −1.62 V versus Ag/AgCl reference electrode. The calculated corrosion current density, i_{corr} (tabulated in Table 3.3) for pure Mg is ~29.26 μAcm^{-2} equivalent to corrosion rate ~ 0.7 mm/year if it is assumed that the general corrosion occurred on the surface

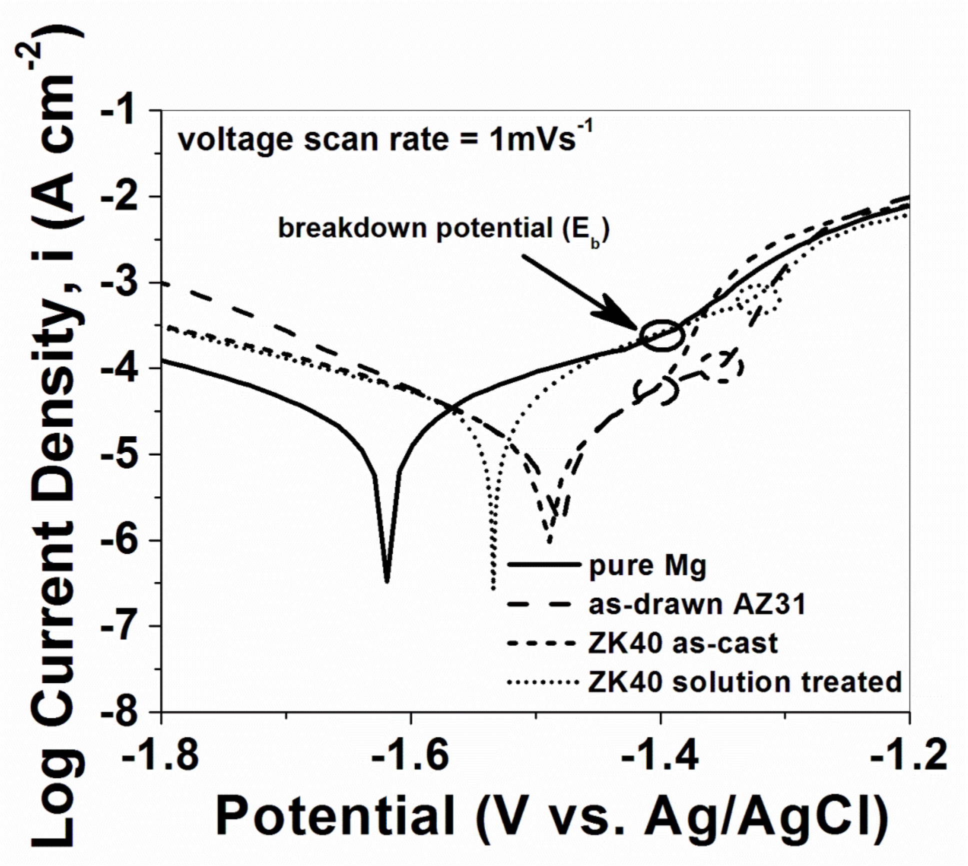

Figure 3.5 Potentiodynamic polarization plots (tafel plots) of pure Mg, AZ31, as-cast ZK40, and T4-treated ZK40 alloys.

(103). On the other hand, the as-cast ZK40 and as expected, the as-drawn AZ31 samples showed improved corrosion potential and E_{corr} values displaced toward the more noble direction compared to pure Mg. It is already known that zinc contributes to elevation of the corrosion potential and thus improve the corrosion rate (104). Corrosion potentials for as-cast ZK40 and AZ31 alloys were determined to be -1.49 V and -1.48 V, respectively.

The calculated corrosion rate, i_{corr} (determined by Tafel extrapolation) values for the as-cast ZK40 and AZ31 was ~ 0.90 mm/year and 0.43 mm/year, respectively. Although the corrosion potential of solution treated ZK40 alloy is -1.55 V, which shifted slightly towards the cathodic direction, there was an improvement in the corrosion rate over the as-cast sample. The corrosion rate, i_{corr} of the solution treated ZK40 sample is 0.87 mm/year. Improvement in the corrosion current density (~39.32 μAcm^{-2}) and corrosion rate of solution treated ZK40 alloy compared to the as-cast state is primarily due to reduction in the second phase (Mg_7Zn_3) intermetallic which was observed to be discontinuously precipitated along the grain boundaries in the as-cast sample as discussed earlier. Solution treatment of the as-cast sample at 300 °C for 1 h reduces the volume fraction of the second phase [$Mg_7Zn_3 \rightarrow \sigma$-Mg(Zn,Zr) + MgZn] occurring as a consequence of the eutectic transformation causing an increase in the amount of σ-Mg(Zn, Zr) primary phase resulting hence in the sudden drop in the corrosion potential.

Figure 3.5 also illustrates the formation of a passivation layer in the anodic branch of the polarization plot. The breakdown potential, E_b of pure Mg, AZ31, as-cast and solution treated ZK40 samples were correspondingly -1.41, -1.35, -1.41, and -1.33 V, respectively. It can be seen that the E_b for AZ31 and solution treated ZK40 samples were both higher and thus better than pure Mg which suggests that pure Mg was more prone to localized corrosion by disruption of the protective oxide layers. On the other hand, both AZ31 and solution treated ZK40 exhibit

Table 3.3 Corrosion rates (mm/year) determined by potentiodynamic polarization and immersion techniques of pure Mg, as-drawn AZ31, as-cast and solution treated ZK40 alloys (n=3, $^{*}p<0.05$ with all other groups).

Materials	Corrosion potential, E_{corr} (V)	Corrosion current density, i_{corr} ($\mu A\ cm^{-2}$)	Breakdown Potential E_b (V)	Corrosion rate CR (mm/year)
Pure Mg	-1.62	29.26±3.18	-.141	0.70±0.07*
As-drawn AZ31	-1.48	19.20±2.08	-1.35	0.43±0.05*
As-cast ZK40	-1.49	39.69±1.08	-1.41	0.90±0.02
T4 treated ZK40	-1.55	39.32±2.01	-1.33	0.87±0.04

resistance to localized corrosion by the well-known passivation phenomena. Interestingly, the as-cast ZK40 alloys exhibited a low breakdown potential (-1.41 V). In general, the anodic branch of polarization curve is characterized by a sudden drop in the anodic current representing a change in the slope, known as the breakdown Potential (E_b). During anodic polarization, a passive film formed on the surface provides a protective barrier that keeps the corrosion current at a low value so that the extent of corrosion damage is minimized. An effective protective layer is obviously characterized by one that provides a strong resistance to breakdown of the passivation layer. As the potential is increased, corrosion via surface breakdown will begin at a certain voltage value termed as the breakdown potential (E_b), the lowest potential at which corrosion occurs. Since corrosion relates to an increase in the oxidation rate, the E_b is determined by the corresponding increase in measured anodic current. An increase in E_b is associated with higher resistance to corrosion. Breakdown potentials cause the disruption of the passive film and thus expose bare sites of the surface to an aggressive physiological environment wherein the tendency for attack is very high contributing to the accelerated corrosion of the alloy.

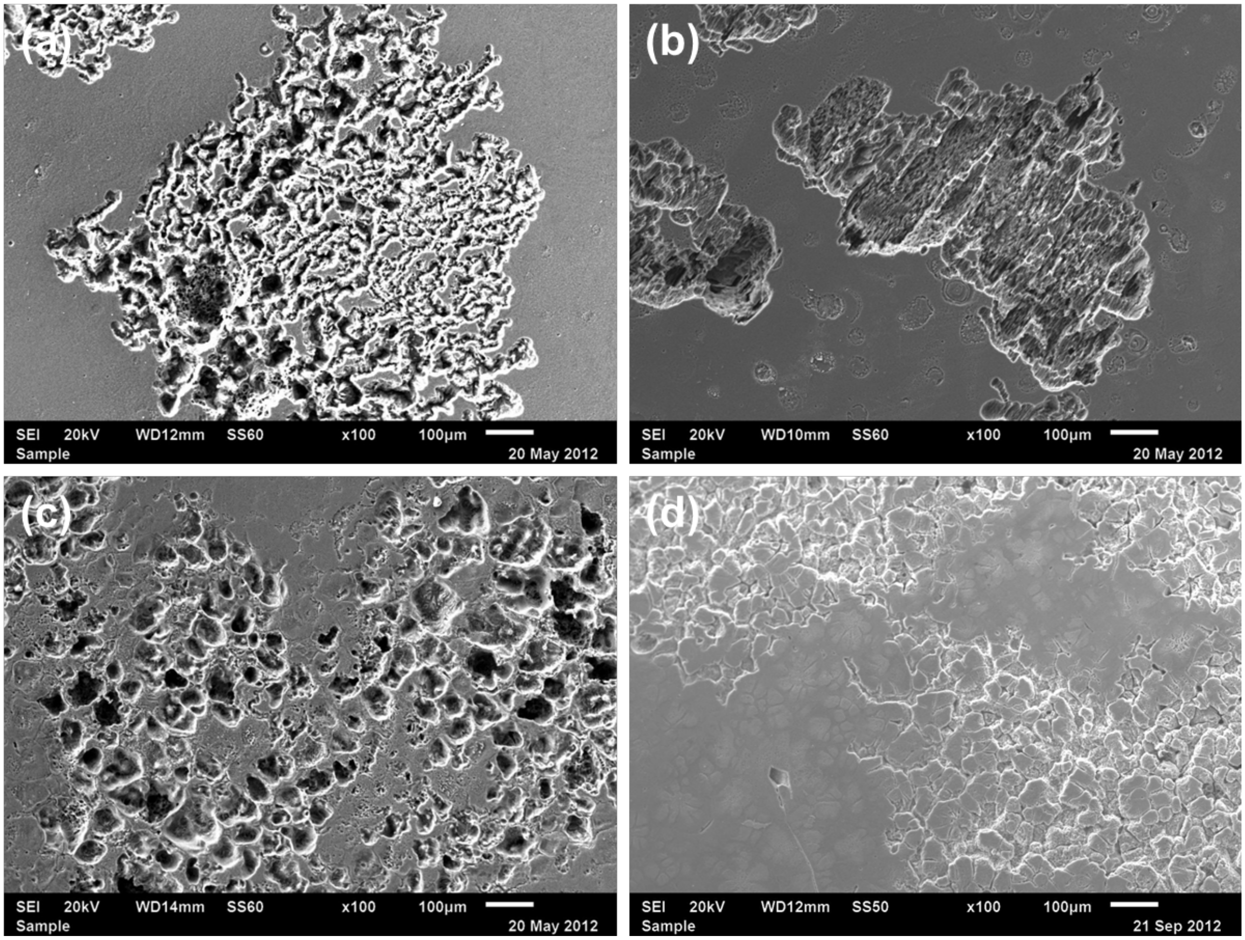

Figure 3.6 SEM micrographs of (a) pure Mg (b) AZ31 (c) as-cast ZK40 (d) T4-treated ZK40 surfaces after potentiodynamic polarization measurements. Samples were cleaned with CrO_3/$AgNO_3$ solutions for 10 min.

Figure 3.6 shows the corrosion morphology evolved during potentiodynamic polarization test of the samples, after the corrosion products were correspondingly cleaned by CrO_3 and $AgNO_3$ treatment. Previous scientific studies have shown that in a multi-phase alloy, the corrosion rate is primarily controlled by the following factors: a) purity, b) the composition of matrix, c) composition of second phase(s) and its distribution in the microstructure (105, 106). Since, in the case of pure Mg, there is no second phase present, the corrosion mechanism was primarily governed by the total impurity present and the presence of weak grain boundary regions. Figure 3.6(a) shows that, mainly irregular localized corrosion pits was evident which was laterally spread over the whole surface. The presences of small, discrete pits in the microstructure suggest that the presence of impurities do play a role for localized corrosion in case of pure magnesium. On the contrary, in the case of AZ31 sample, $Mg_{17}Al_{12}$ (β-phase) is the predominant second phase present along the grain boundaries. The presence of second phase will accelerates the corrosion of adjacent α-Mg matrix. Figure 3.6(b) shows the corroded surface of AZ31 where pitting was the predominant corrosion mechanism evident by the presence of small interconnected pits throughout the corroded surface. Figure 3.6(c) shows the corroded surface of ZK40 sample in the as-cast condition wherein the presence of irregular pits on the surface clearly suggests that pitting was indeed the dominant corrosion mechanism. Microstructural investigation of ZK40 as-cast sample outlined in section 3.3.1 shows that secondary phase(s) of Mg_7Zn_3 and MgZn are present along the grain boundaries likely causing the accelerated corrosion of the α-Mg matrix. However, in the case of solution treated ZK40 sample, the percentage of second phase(s) decreases with solution treatment having a direct consequence on the corrosion rate and morphology as clearly, no surface pits are observed on the corroded surface as shown in Figure 3.6(d).

3.4 CONCLUSIONS

Microstructural analysis of the as-cast and solution treated Mg-4wt%Zn-0.5wt% Zr or ZK40 alloys by optical and SEM suggest the formation of uniform equiaxed grains throughout the microstructures with average grain size of 50±10 μm and 87±10μm, respectively. SEM performed in the back-scattered mode and execution of the EDS analysis of the as-cast ZK40 alloy clearly shows the presence of Mg_7Zn_3 intermetallic phase along the grain boundaries which undergoes eutectic transformation during solution treatment at 300 °C for 1 h resulting in the formation σ-Mg(Zn, Zr) primary phase and MgZn secondary phase contributing to improved corrosion resistance.

4.0 SPECIFIC AIM II: IDENTIFICATION OF THE POTENTIAL OF MAGNESIUM-ZINC BASED ALLOYS AS A BIODEGRADABLE SYSTEM USING IN VITRO CHARACTERIZATION METHODS

4.1 INTRODUCTION

Following the synthesis and materials characterization studies reported in Chapter3, both as-cast and solution-treated Mg-4wt%Zn-0.5wt%Zr (ZK40) were further investigated for their biocorrosion resistance, mechanical properties, and cytocompatibility. Corrosion resistance of ZK40 alloy was further assessed using immersion corrosion test methods. Accordingly, tensile and compressive mechanical properties were investigated using Instron universal test machine. Preliminary cytocompatibility experiments such as a direct (live/dead) and indirect (MTT) assay were performed using a mouse osteoblast-like cell line. Finally, an *in vivo* murine subcutaneous model was used to explore the acute host response after 40 and 70 days of implantation. Results of these studies are described in this chapter.

4.2 MATERIALS AND METHODS

4.2.1 Tensile and compression test

Tension tests were performed for both, the as-cast and T4 treated ZK40 alloys as well as AZ31, and pure Mg in accordance with ASTM standard practice for tensile testing ASTM-E8-04 (107) at room temperature using an MTS11 frame with 50kN load cells and LX500 laser extensometer (MTS Systems Corporation, Eden Prairie, MN, USA) by OrthoKinetic® Testing Technologies. Standard dog bone specimens of 12.7 mm in gauge length and 3 × 3 mm in gauge cross-section were machined and used for the tension tests. Samples were accordingly pulled to failure at the cross-head speed of 1.3 mm/min. Tensile stress-strain curves were utilized to determine the yield strength (YS), ultimate tensile strength (UTS), Young's modulus (E) during tension, and total elongations (%) of each alloy specimens. Averages of 3 sample measurements were reported.

4.2.2 Immersion corrosion measurement

Immersion corrosion measurements were performed in conformation with ASTM G31-72 (108). Pure Mg, ZK40 as-cast and ZK40 T4-treated specimens were prepared in dimension of 10 × 10 × 1 mm and polished up to 1200 grit using SiC paper. Surface area and the weight of each specimen was carefully recorded before the immersion test. The specimens were thoroughly cleaned in acetone using a sonicated bath followed by UV sterilization for 30 min for each side. After sterilization, the specimens were immersed in DMEM + 10% FBS + 100 U/ml penicillin, and 100 μg/ml streptomycin using a fishing line at 37.4 °C in a humidified atmosphere with 5% CO_2. DMEM + 10% FBS media volume to surface area ratio was 20 ml/cm^2 according to the

ASTMG31-72 standard (108). Specimens were removed after 1, 2 and 3 weeks of immersion, rinsed with distilled water and dried at room temperature. Further, the specimens were cleaned with 200 g/L of chromic acid and 10 g/L of $AgNO_3$ solution for 10 min to remove the corrosion products similar to the procedure described in Chapter 3 (94). The difference in weight before and after immersion was recorded and the degradation rates (in units of mm/year) were obtained according to ASTMG31-72 (108). The corrosion rate is thus given by:

$$\text{Corrosion rate} = (K \times W)/(A \times \mathrm{T} \times D) \; \ldots.. \; \text{Eq. (1)}$$

where the time conversion coefficient $K = 8.76 \times 10^4$, W is the weight difference before and after immersion (g), A is the sample area exposed to solution (cm^2), T is the exposure time (h) and D is the density of the material ($g\ cm^{-3}$). The pH value of the solution was also recorded during the immersion tests. Averages and standard deviations of 3 sample measurements were reported and one-way ANOVA was used to determine any significant mean differences with a p-value less than 0.05 for each time point.

4.2.3 Indirect MTT cell viability assay

Pure Mg, ZK40 as-cast, and ZK40 T4-treated specimens were sectioned to exhibit dimensions of 10 x 10 x 1 mm, polished up to 1200 grit SiC paper, sonicated in isopropanol, and sterilized under ultraviolet radiation for 30 min before extract preparation. The specimens were incubated with modified Eagle’s medium alpha (α-MEM) supplemented with 10% fetal bovine serum (FBS), 100 U/ml penicillin, and 100 μg/ml streptomycin at 37 °C in a humidified atmosphere with 5% CO_2 for 72 h. The specimen weight to extraction medium ratio was maintained at 0.2 g/mL in accordance with EN ISO standard 10993:12 (109). This extraction ratio was designated as 100% extract, with less concentrated extracts prepared by diluting the 100% extract into 50%, 25%, and 10% extract solutions, respectively. Extracts were then sterile filtered using 0.2 μm syringe filter before being added to cells.

Further, the murine osteoblastic cell line (MC3T3-E1, American Type Culture Collection, Rockville, MD) was used in *in vitro* cell cytotoxicity experiments, cultured in modified Eagle's medium alpha (αMEM), 10% fetal bovine serum (FBS), 100 U/ml penicillin and 100 μg/ml streptomycin at 37.4 °C in a humidified atmosphere with 5% CO_2. The cells were seeded in a 96-well plate at cell density of 6000 cells/well and incubated for 24h to attach before adding the extraction medium. The controls used as culture medium without extract as the negative control and 10% DMSO cultur**e** medium as the positive control Cell culture media with pre-cultured cell was replaced with the 200 μl extract media at 1x, 2x, 4x, and 10x extract dilution and incubated for 72 h under cell culture condition. The cytotoxicity of the extracts was tested using the MTT assay. Media and extracts were replaced with fresh cell culture medium to prevent interference of the magnesium ions in the extract from interacting with the tetrazolium salt (110). The MTT assay was performed according to the Vybrant MTT Cell Proliferation Kit (Invitrogen Corporation, Karlsruhe, Germany) by first adding 10 μl of 12mM 3-(4,5-Dimethylthiazol-2-yl)-2,5-diphenyltetrazolium bromide (MTT) dissolved in phosphate buffer solution (PBS, pH = 7.4) to each well. MTT salt was dissolved in PBS at the ratio of 5 mg/mL and diluted in phenol red free media in a1:11 ratio to replace the magnesium ion containing media from interfering with the blue formazan measurement. The mixture of MTT solution and phenol red free media replaced the extract media after 72 h culture and was incubated for another 4 h under cell culture condition. Formazan crystals were solubilized using sodium dodecyl sulfide dissolved in 0.01M hydrochloric acid at the ratio of 1mg/10 mL (SDS-HCl). 100ul of SDS-HCl was added to each well and incubated for 12 h under cell culture condition. The well plate was then analyzed by a

ELISA microplate reader at a wavelength of 570 nm with a reference wavelength of 635nm. Averages and standard deviations of 3 sample measurements were reported and one-way ANOVA was used to determine any significant mean differences with a p-value less than 0.05 for each dilution factors of the extract media.

4.2.4 Live/dead cell viability assay

The murine osteoblast-like cell line MC3T3 was cultured in Dulbecco's modified eagle medium (α-MEM) with 10% fetal bovine serum (FBS), 100 U/ml penicillin, and 100 μg/ml streptomycin at 37.4 °C in a humidified atmosphere of 5% CO_2. Cells were seeded onto specimen surfaces at cell density of 4×10^4 cells/mL and each well contained 2mL of media to completely cover the specimen. After 72 h of incubation, the live/dead assay was performed using commercially available LIVE/DEAD viability/cytotoxicity kit (Invitrogen Inc. Karlsruhe, Germany) to stain the live and dead cells to glow in green (ethidium homodimer-1) and red (calcein-AM) respectively, under fluorescence microscopy at the excitation wavelength of 495 nm. After fluorescence imaging, cells on the specimens were fixed by 2.5% glutaraldehyde for 15 min and dehydrated by immersing the specimens in 70, 80, 90, 95, and 100% diluted ethanol for 15 min per dilution factor subsequently. Specimens with fixed cells were air dried and captured by SEM.

4.2.5 *In vivo* murine subcutaneous study

In vivo murine subcutaneous study was conducted to explore any acute host response of pure Mg, as-drawn AZ31, and as-cast ZK40 samples. Mice implantation was performed at

University of Cincinnati with an approval of its Animal Care and Use Committee (IACUC) in collaboration with Dr. Zhonghyun Dong. For this study, discs of 5 mm diameter and 1.4 mm thickness were sectioned from as-cast ZK40, pure Mg, and AZ31 alloy specimens. The disc samples were than sonicated in acetone, air-dried, and further sterilized by UV radiation. Healthy nude mice were housed under controlled conditions and maintained with a standard diet and water. Mice were anesthetized by isoflurane and a small skin incision was made for implantation of the disc in the subcutaneous regions. Surgical staples were used to close the incisions. After 40 and 70 days, the animals were sacrificed using a CO_2 gas chamber and disc samples were removed followed by the cervical dislocation. The disc implants with surrounding tissue were recovered, carefully separated from the tissue, cleaned, air-dried, and weighed. The surrounding subcutaneous tissue was harvested and fixed using 10% formalin in PBS, paraffin-embedded, and sectioned (4 μm/section) for hematoxylin-eosin (H&E) staining.

4.3 RESULTS AND DISCUSSION

4.3.1 Mechanical properties of Mg-Zn-Zr alloy

Table 4.1 summarizes the mechanical properties of both, the as-cast and solution treated Mg-4%Zn-0.5%Zr (ZK40) alloys as well as pure Mg, and commercial as-drawn AZ31 studied for the present work along with a direct comparison made with natural bone (111). It is worthy to mention here as discussed earlier for the corrosion response as well, that compared to pure Mg, the addition of zinc and small amount of zirconium has a dramatic effect on the values of tensile strength. Yield strength and ultimate tensile strength (UTS) for the as-cast Mg-4%Zn-0.5%Zr was 96 MPa, and 176 MPa respectively. However, there was a little drop in the yield strength and UTS values of solution treated Mg-4%Zn-0.5%Zr alloy compared to as-cast alloys likely due to increase in the average grain size which invariably reduces the yield strength as is well-known in the physical metallurgy literature (112, 113). As-drawn AZ31 showed the highest yield strength of 55 MPa and UTS of 202 MPa among all the alloys studied here. Elastic Modulus of the pure magnesium was low ~5 GPa, however, Mg-4%Zn-0.5%Zr alloys demonstrated excellent modulus (~ 64 GPa) suggesting that the alloy possesses high strength under tensile testing. Similarly, the as-drawn AZ31 also display a high stiffness value. It should be noted that all the alloys studied here possess a high modulus values compared to natural bone except pure magnesium. The total elongation to failure (%) for pure magnesium and as-drawn AZ31 samples were 7 and 12%, respectively.

Table 4.1. Mechanical properties of the as-drawn AZ31, pure Mg, ZK40, and ZK60 alloys (n=3, *buckling noticed during the measurement due to the mismatch between sample size and load cell).

Alloy	Density (g/cm^3)	Modulus (GPa)	Yield Strength (MPa)	Ultimate Tensile Strength (MPa)	Compressive Yield Strength (MPa)	Elongation (%)	References
Cortical bone	1.8-2.0	5-23	104.9-114.3	35-283	164-240	1.07-2.1	(111)
Cancellous bone	1.0-1.4	10-1570 (MPa)	---	1.5-38	---	---	(111)
As-drawn AZ31	1.78	55	202	268	105	12	Present study
Pure Mg	1.74	5*	19	66	140	7	Present study
As-cast ZK40	1.80	64	96	176	125	4	Present study
ZK40 solution treated	1.80	68	92	134	92	3	Present study
As-cast ZK60	---	---	150	210	120	6	(85)
ZK60 extruded	---	---	290	335	250	16	(85)

In contrast, total elongation to failure under tension of Mg-4%Zn-0.5&Zr alloys in the as-cast and solution treated conditions was observed to be 4 and 3%, respectively. The low value of elongation to failure for both the as-cast and solution treated Mg-4%Zn-0.5%Zr alloy is likely due to the presence of second phase (Mg_7Zn_3) which increases the hardness and strength of the alloy while undermining the total elongation to failure. Similar observation was reported by Cai et al. (75) who observed that addition of more than 5 wt% zinc has a negative effect on the mechanical properties of the alloy due to the presence of number of MgZn intermetallic phase(s) which precipitate along the grain boundary during solidification. Commercial as-drawn AZ31 alloy displayed a higher yield and tensile strengths compared to all the alloys studied here. Increase in yield value and tensile strength with the addition of 4% zinc and 0.5% zirconium to the pure magnesium mainly originates from the strong grain refinement efficacy of zirconium on the alloy microstructure which is based on Hall-Petch relationship (112, 113). According to the Mg-Zn establish phase diagram (114), the maximum solubility of zinc is 1.6 wt% in magnesium at room temperature. Thus zinc mainly dissolve in primary α-Mg and imparts solid solution strengthening improving the castability of the alloy (111, 115). It is also important to note that the presence of Mg_7Zn_3 intermetallic along the grain boundary regions in Mg-4%Zn-0.5%Zr alloys hinders the dislocation movements during plastic deformation causing an increase in the strength of the alloys at the expense of desired plasticity. However, the discontinuous precipitates formed along the grain boundaries may sometimes act as stress concentrators leading to brittle fracture of the alloy under tensile loading.

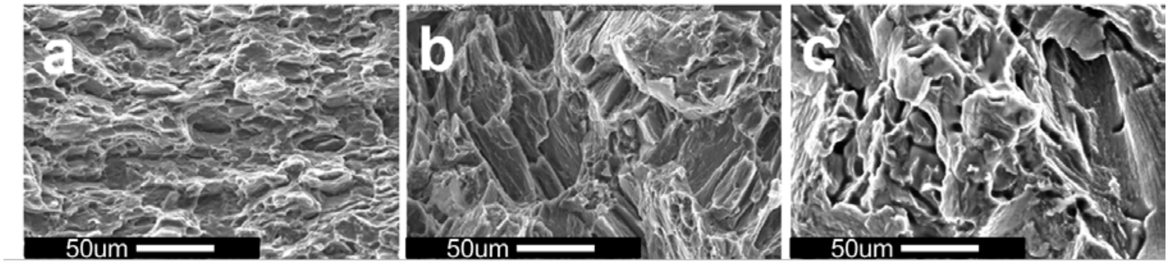

Figure 4.1 Fractographs of (a) as-drawn AZ31, (b) as-cast ZK40, and (c) Solution treated ZK40 alloys.

Figure 4.1 provides the fractographs of the cross-sectional surfaces after tensile testing. The fracture surface of the as-drawn AZ31 alloy specimen (see Figure 4.1a) shows a ductile mode fracture with the presence of dimples throughout the fracture surface. On the other hand, the as-cast ZK40 tensile specimen in Figure 4.1b illustrates a mixed fracture mode including inter-granular cracks and cleavage patterns. The presence of cleavage and quasi cleavage patterns are common for Mg-4%Zn alloy which have been verified by others (116-118). The presence of intermetallic phase along the grain boundaries leads to crack propagation under tensile loading which may result brittle failure. However, solution treated ZK40 alloys exhibited both brittle-ductile fracture mode together supported by the presence of cleavage planes and dimples. The number of dimples observed on the fracture surface (Figure 4.1c) was minimal and possibly appeared when the second phase was dissolved back in to the $\alpha-$Mg matrix during solution treatment, causing grain softening leading to possible ductile mode failure.

4.3.2 Immersion corrosion properties of Mg-Zn-Zr alloy

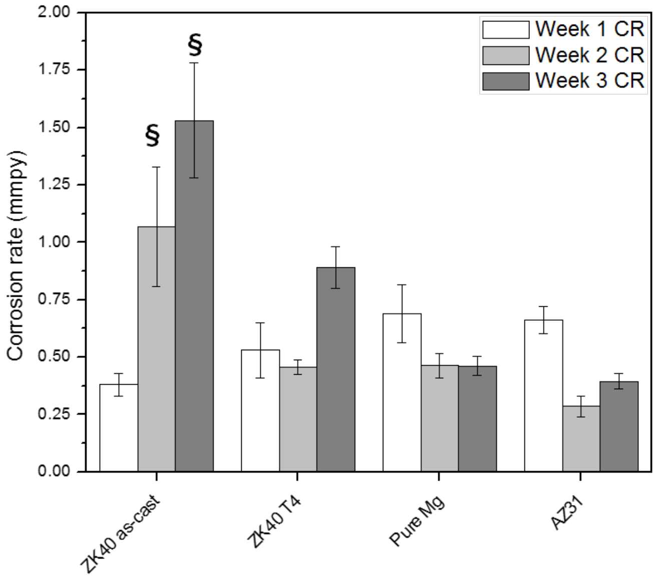

Figure 4.2 Corrosion rate of pure Mg, as-cast ZK40, and T4-treated ZK40 by mass loss after 7, 14, and 21 days immersion in DMEM + 10%FBS (n = 3, §p<0.05 denotes a significant difference with all other groups).

The average weight loss of pure Mg, as-drawn AZ31, as-cast and solution treated ZK40 alloys are displayed in Figure 4.2. The average corrosion rate for pure Mg and AZ31 was determined to be 0.69±0.13 and 0.66±0.05 mm/year, respectively, after 7 days of static immersion in DMEM + 10%FBS. The corrosion rate was decreased further during 14 days and 21 days immersion test which is in agreement with the reported values in literature (119). The decrease in the average weight loss rate was likely due to the formation of a passivation layer on the surface which retarded further corrosion. However, in the case of as-cast and solution treated ZK40 samples opposite trends were observed. The corrosion rates were increased in the order of 7, 14, and 21 days static immersion in DMEM + 10%FBS. The average weight loss of the as-cast and T4 treated ZK40 alloys after 7 days of immersion were

0.39 ± 0.05 and 0.53 ± 0.12 mm/year, respectively. The corrosion rate was dramatically increased to 1.07 ± 0.26 and 1.53 ± 0.25 mm/year for the as-cast ZK40 sample during 14 days and 21 days immersion, respectively.

The increase in corrosion rate suggests that the protective layer [$Mg(OH)_2$] which forms on the surface during static immersion was not stable and contributed to further corrosion. The above finding was in agreement with electrochemical corrosion study where it was determined that the breakdown potential, E_b (-1.41 V) of as-cast ZK40 alloy was close the corrosion potential, E_{corr} (-1.49 V) which resulted in rapid corrosion and dissolution of the corroded product simultaneously. The average corrosion rate for solution treated ZK40 alloy was slightly reduced from 0.53 ± 0.12 mm/year, to 0.46 ± 0.03 mm/year from 7 days to 14 days but again increased to 0.89 ± 0.09 mm/year after 21 days static immersion. The exact reasons for this anomalous corrosion rate are still unknown and subject of further investigation. A possible explanation could be the nature of the hydroxide formed due to the solution treatment causing dissolution of Zinc into the α-phase of Mg and formation of MgZn intermetallic. It is possible that the stability of the Mg-hydroxide due to incorporation of Zn is altered at the 21 day time period probably leading to fine precipitates forming likely increasing the solubility causing an inrease in the corrosion rate observed. These are however, largely speculatory at present warranting further study.

Surface morphology of the corroded surfaces as-cast and solution treated ZK40 alloys after 21 days static immersion was shown in Figure 4.3. It appears that both as-cast and solution treated ZK40 alloys were uniformly corroded. However, the presence of large holes was likely due to severe pitting corrosion along the grain boundary regions which were weak spots due to presence of second phase(s) precipitates that was more prone to attack locally by

Cl^-, HCO_3^-, SO_4^{2}, ions etc. present in the cell culture media (75, 120).

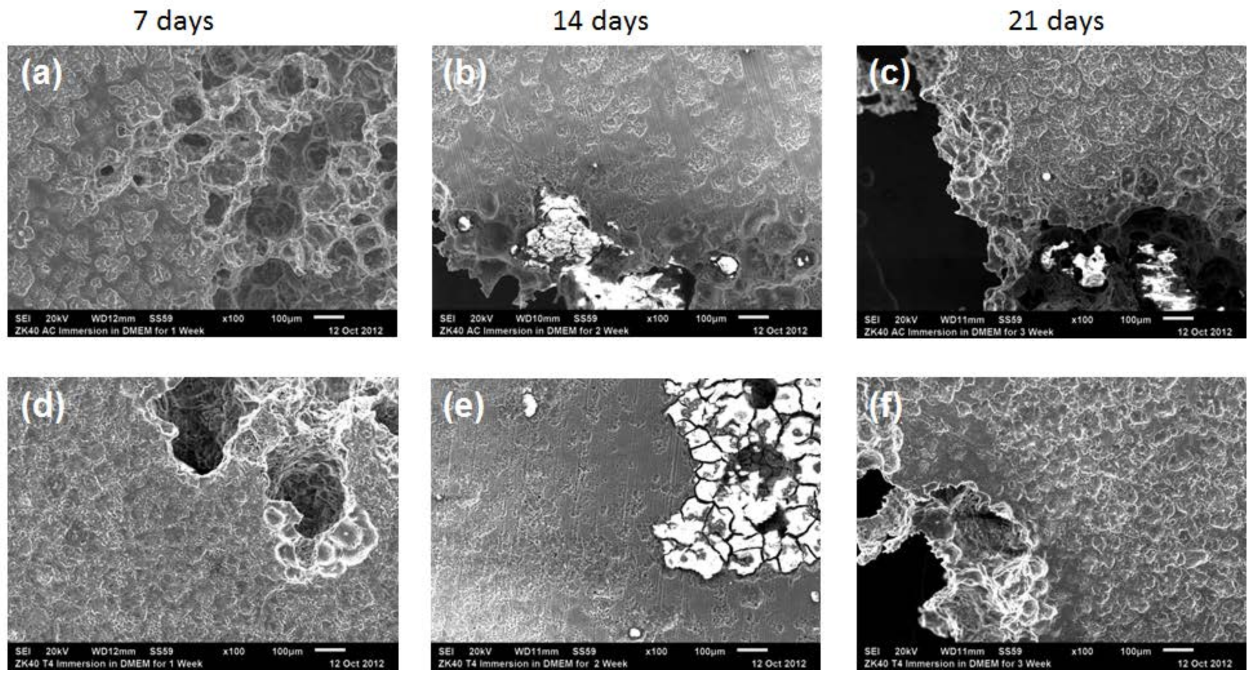

Figure 4.3 SEM micrographs of as-cast ZK40 alloy after exposure of (a) 7 days, (b) 14 days, (c) 21 days, and T4-treated ZK40 after (d) 7 days, (e) 14 days, (f) 21 days of immersion in DMEM+10% FBS+1% P/S physiological environemnt at 37.4 °C 5% CO_2 atmosphere.

4.3.3 Cytocompatibility of Mg-Zn-Zr alloy

4.3.3.1 Direct MC3T3 cytocompatibility using Live/dead assay

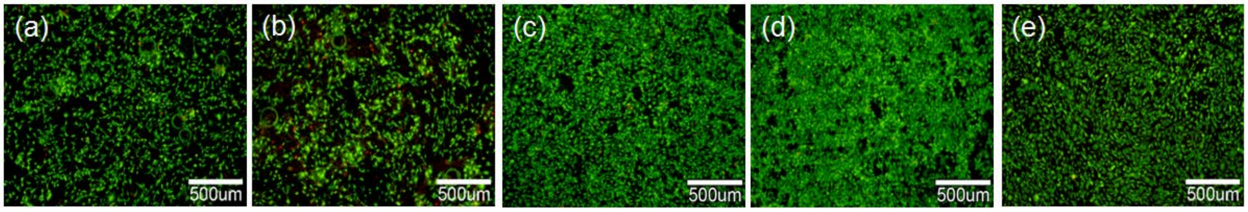

Figure 4.4 Fluorescent images of live (green) and dead (red) MC3T3-E1cells attached on the polished surfaces of (a) AZ31 (b) pure Mg (c) as-cast ZK40 (d) T4-treated ZK40 (e) cell culture plastic after 3 days culture.

Cell viability was studied for the pure Mg, AZ31, as-cast and solution treated ZK40 samples with the 3 day cell culture time with extracts. Figure 4.4 shows the osteoblastic MC3T3-E1 cells cultured in direct αMEM + 10% FBS for 3 days and then stained with calcein-AM and EthD-1. Live cells convert calcein AM to the green fluorescent calcein through intracellular esterase activity, while EthD-1 enters cells with compromised membranes where it binds with nucleic acids and produces a bright red fluorescence. As-cast as well as solution treated ZK40 sample show improved cell viability when compared with AZ31 and pure magnesium as the cell density is clearly seen to be more and evenly distributed. There was no significant difference in the shape of the live cells (green) between the control and the studied samples groups. Only a few apoptotic cells (red fluorescence in the nuclei) were seen in each group.

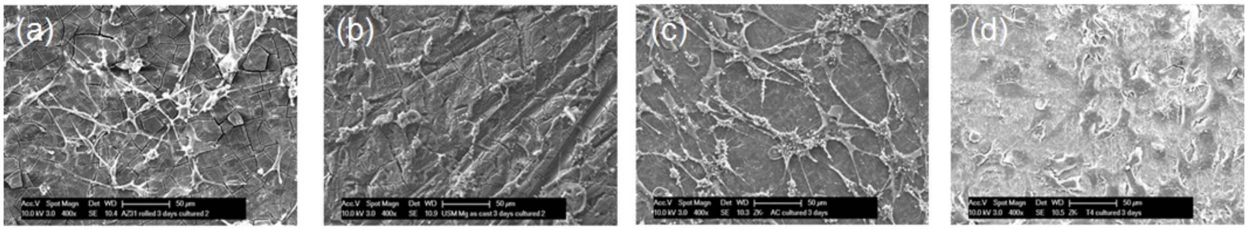

Figure 4.5 SEM micrographs of MC3T3 cells fixed on (a) AZ31 (b) pure Mg (c) as-cast ZK40 (d) T4-treated ZK40 after 3 days culture followed by live/dead cell viability assay.

Figure 4.5 shows the morphology of the fixed MC3T3-E1 cells in 2.5% glutaraldehyde solution for 15 min after 3 days incubation in the α-MEM. The cells can be seen to attach to the surface of the sample and it is also evident that the cells start to proliferte on the surface. The cell spreading can be seen to be uniform with filopodia formations suggesting that the Mg-Zn-Zr sample are stable in the physiological environment and likely forming a protective layer which retards the released ion cocentrations (Mg^{2+}, Zn^{2+}) facilitating cell growth and proliferation.

4.3.3.2 Indirect MC3T3 cytocompatibility using MTT assay

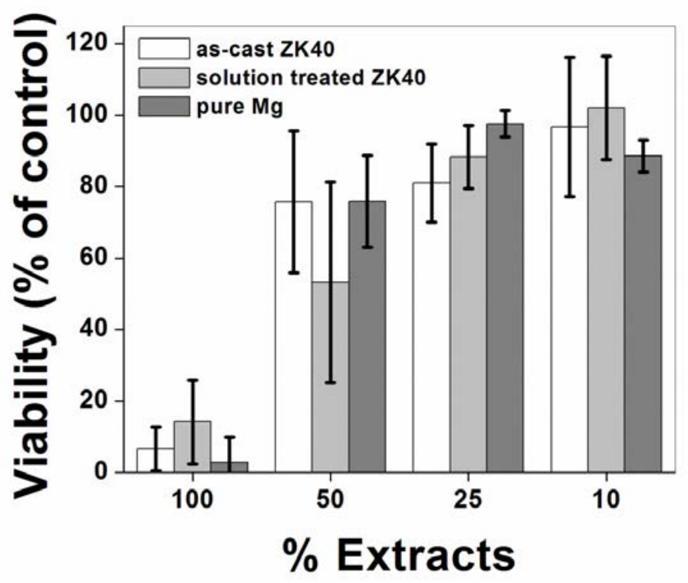

Figure 4.6 Indirect cytotoxicity of MC3T3 cells cultured for 3 days in extract media from pure Mg, as-cast ZK40, and T4-treated ZK40 alloys. Viability is taken as percent of negative control (n =3).

Figure 4.6 shows the indirect cytotoxicity results performed using MC3T3-E1 cells and the MTT assay for 3 days extract. For 3 days culture periods, cell viability was almost non-existent with undiluted extract (100%) concentration compared to negative control. However, cell viability was increased as the extract of the corrosion media was diluted to 50%, 25% and 10% and fresh media was added to the cell. The cell viability level was recorded as ~ 80% for as-cast and pure Magnesium level at the 50% dilution level suggesting the good cell compatibility of ZK40 alloy. The cell compatibility level was further improved with 25% extract dilution. All the three samples of as-cast and solution treated ZK40 and pure Mg showed greater than 75% cell viability level at 50% and 25% extract dilution with respect to the negative control. The above finding are in good agreement with the recent findings reported in the literature which show higher extract concentrations are highly cytotoxic in nature leading to osmotic shock due to the released ion concentration, suggesting that a 10-fold extract dilution will be more suitable and likely sufficient to determine the cytotoxicity level among various magnesium alloys (121). The ISO protocol of cytotoxicity test also identified 75% or higher cell viability as indicator for non-cytotoxicity (122) and thus the results here suggests the biocompatibility of the studied ZK40 alloy material.

4.3.4 In vivo biocompatibility of Mg-Zn-Zr

Figure 4.7 exhibits the histological image of local sites of implants harvested in murine subcutaneous tissue surrounding as-cast ZK40, pure Mg, and AZ31 after 40 and 70 days. Some visible amount of gas pocket was observed around as-cast ZK40 implantation after 40 days and a significant mass loss of as-cast ZK40, compared to pure Mg and AZ31, was measured after sacrificing the animals and explanting the alloy specimen. Moderate inflammatory response was observed in the H&E histology results (see Figure 4.7). Abundant population of fibroblasts was observed around the Mg alloy samples. Degradation of as-cast ZK40 was observed to be more progressively pronounced than pure Mg and as-drawn AZ31 (see Figure 4.8). An acute inflammatory response was however, not apparent in the specimens though analysis of long term responses along with degradation analysis is required to provide a more detailed, accurate and plausible explanation. These studies are planned in the near future.

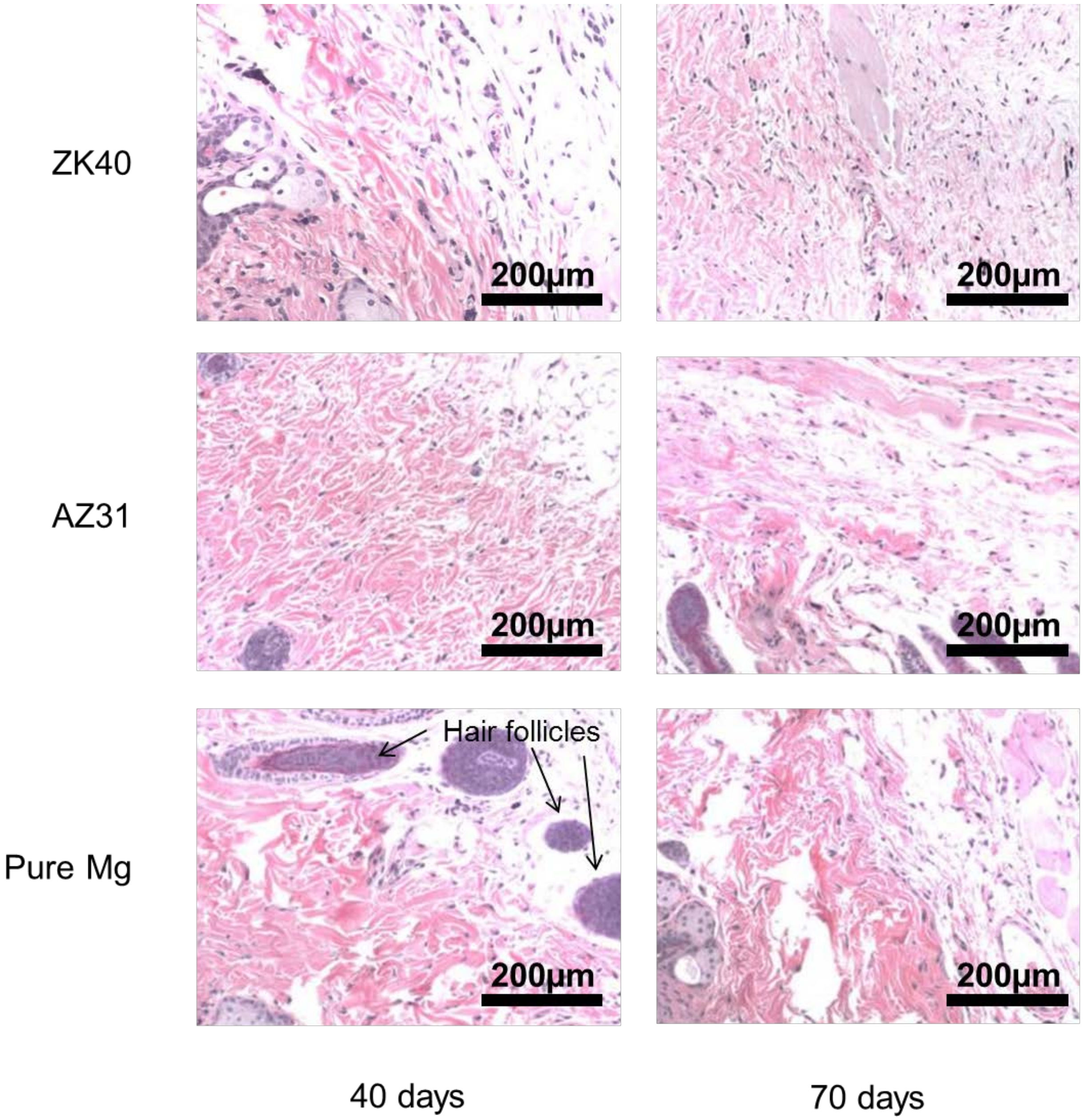
ZK40
AZ31
Pure Mg
Hair follicles
200µm
200µm
200µm
200µm
200µm
200µm
40 days
70 days

Figure 4.7 H&E staining of murine subcutaneous tissue in contact with pure Mg, as-drawn AZ31, and as-cast ZK40.

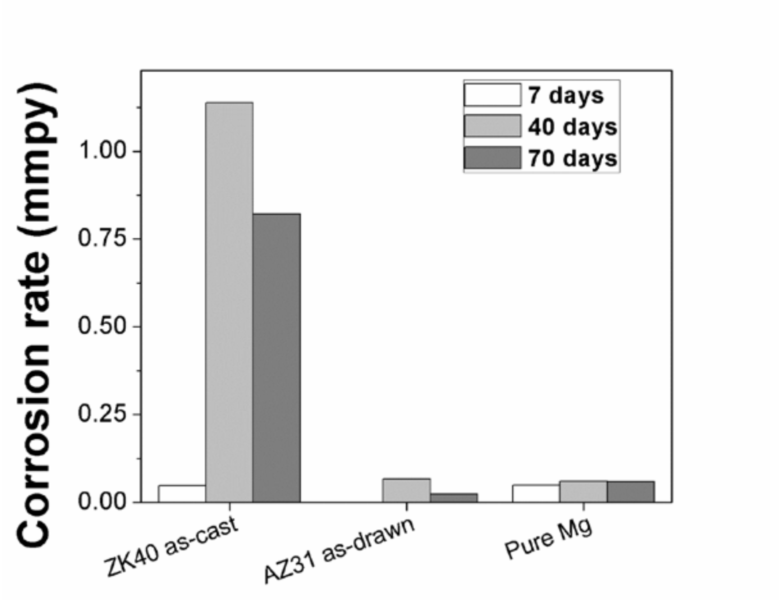

Figure 4.8 Corrosion rate of pure Mg, AZ31, and as-cast ZK40 by mass loss after 40 and 70 days of pellet implantation in murine subcutaneous tissue **(n =1).**

4.4 CONCLUSIONS

In the present studies, as-cast and solution treated ZK40 alloys were investigated as a potential biodegradable alloys for possible orthopedic and craniofacial applications. Potentiodymamic polarization test in DMEM + 10% FBS discussed in Chapter 3 shows that the ZK40 alloy has a comparable corrosion rate with pure Mg and as drawn AZ31. Long term corrosion by static immersion technique however, shows that the corrosion trends for as-cast and solution treated ZK40 alloys are in fact, opposite than pure Mg and AZ31. The average weight loss rate for pure Mg and AZ31 was observed to be stabilized after 7 days immersion and decreased gradually following 14 days and 21 days static immersion, whereas the average weight loss rate for as-cast ZK40 alloy shows an increse in average weight loss rate likely due to formation and dissolution of protective layers simultaneously on the corroded surface. *In vitro* analysis by direct live-dead assay and indirect MTT assay using murine osteoblast MC3T3 cells show good cell viabiltity compared to pure Mg and AZ31. Direct implanatation of as-cast ZK40 samples in mice subcutaneous model also shows no acute inflammatory response and healthy fibroblast formation along the implantation site after 40 and 70 days, suggesting that ZK40 alloy could be a potential biodegradable implant. Preliminary *in vitro* and *in vivo* results suggest that long term testing and animal experiments are however, necessary to understand the degradation behavior, loss of mechanical strength, and immune response under *in vivo* environment. Further, extrusion/rolling, and equal channel angular pressing at elevated temperature have been reported to be capable of removing the voids, solidification shrinkage, etc. present in the as-cast ingots and improve the mechanical strength and corrosion characteritics (123-125). Thus, hot extrusion or hot rolling will be explored as a potential steps for the use of Mg-Zn-Zr alloy as a potential biodegradable implant material in the near future. Extrusion in fact, has been attempted and the results have been discussed as part of an in vivo fixation device study explained in more details in Chapter 6.

5.0 SPECIFIC AIM III: EFFECTS OF ADDITION OF STRONTIUM AND CERIUM ON THE DEGRADATION, MECHANICAL AND BIOLOGICAL PROPERTIES OF MAGNESIUM-ZINC-ZIRCONIUM ALLOYS

5.1 INTRODUCTION

As discussed all along in the previous chapters, Mg and Mg-based (Mg) alloys have been widely researched as a potential degradable metallic biomaterial with suitable mechanical properties and biocompatibility (126). Corrosion however, is the major degradation mechanism of biodegradable Mg alloys which need to be controlled or monitored to achieve the optimal device resorption rates desired by devices for different applications (38). Corrosion of Mg alloys as outlined in the earlier chapters is controlled by modifying various alloying elements and also adjusting the melting-casting as well as post processing conditions to alter the microstructure of the alloyed systems. Controlled degradation is indeed the major cornerstone ultimately desired requiring proper design of the alloy composition as well as the processing conditions and parameters to maintain the optimal metal ion release rates to be within the accepted tolerable ranges. These ranges are very much needed for fabricating the particular medical devices which will result in elimination of hydrogen gas pockets once implanted in the animal models (127).

Advanced clinical synergy is also anticipated when biodegradable Mg alloys is used as bone fixation devices. Mg alloys are attractive as outlined earlier primarily due to the excellent match of density and mechanical properties of Mg alloys to natural human bone. Bone fixation devices while being very essential are also not preferred to remain in the body once bone healing and desired remodeling has been achieved. Permanent metallic devices are often removed from patients in case of corrosion and wear of the devices. However, such a removal is more forced due to complications or rejection of the implanted hardware leaving the patient very much compromised without a proper remedial treatment of the original medical problem. In most cases, once a solution has been provided and there is healing of the bone with the implanted inert and biocompatible hardware, the hardware is in general kept inside the patient due to the stiffness mismatch with normal bone causing residual stress and stress shielding problems. Removal surgery is more common in pediatric patients to avoid any interference or conflict with growing inherent pediatric bone plates with the implanted hardware causing major complications that run the risk of creating permanent damage. However, such removal surgeries as outlined earlier have their own share of associated risks of recurring fracture, inflammation and other complications. Hence the option of having a degradable metal with mechanical properties matching natural bone renders the concept very attractive and highly lucrative.

Biodegradable Mg-based bone fixation screws have therefore recently received considerable attention and also been recently approved by regulatory agencies in South Korea and Europe (128). These screws are made of Mg-Ca-Zn (129) and Mg-Y-Re-Zr (58) alloys that have exhibited the desired slow corrosion rates. In addition to these alloys, Mg-Zn-Zr alloys also exhibited favorable corrosion resistance, mechanical properties, and cytocompatibility (62, 130, 131). Zn is known for its grain boundary strengthening effect when used up to 5 wt. % as an alloying element in magnesium alloys. Zirconium up to 0.48 wt. % acts as a grain refiner that serves as initial grain forming cite and reduces grain sizes (132, 133).

Mg-Zn-Zr alloys have been available commercially as ZK series alloys. Microstructure of Mg-Zn-Zr can also be suitably monitored to control the corrosion and mechanical properties. Effects of various micro-alloying elements have been researched to achieve higher mechanical properties and corrosion resistance by altering the phase and content of the precipitates. Rare earth elements such as Y, Nd , RE, and Gd are also investigated as additional alloying element to improve the mechanical properties of Mg-Zn-Zr alloys (134-136).

In this regard, Ce is known for providing stable oxide layer coating on Mg alloy when used as an alloying element. Mischmetal is widely used in Mg alloys for improving corrosion resistance and 50% of the Mischmetal content is normally comprised of Ce. Ce is known to affect osteogenic differentiation of hMSC and thus, it is of high interest as an alloying element for biodegradable Mg alloys (91, 92). Sr also promotes osteogenic differentiation of hMSC (137). Mg-Sr, Mg-Zn-Sr and Mg-Sr-Zr has thus been reported as biodegradable Mg alloys exhibiting good cytocompatibility and corrosion resistance (41, 138, 139). Both Ce and Sr however, tend to form secondary phases along the grain boundary. These T-phase precipitates along the grain boundary as any other grain boundary phases are not desirable since they are deleterious as they are notorious for enhancing corrosion and lowering the corrosion resistance.

The present study is thus exploring the use of Sr and Ce as additional micro alloying element in the parent Mg-Zn-Zr alloy discussed earlier in Chapter 3 and 4. Accordingly, as-extruded Mg-Zn-Sr-Zr and Mg-Zn-Ce-Zr alloys have been synthesized to examine the corrosion and mechanical properties. In addition, the effect of Ce and Sr ions along with Mg ions has been investigated in terms of osteogenic differentiation of human mesenchymal stem cells which are new in the field of biodegradable magnesium alloys. Results of these studies are presented and discussed in this chapter. It is reported that 10 mM $MgSO_4$ supplementation in differentiation media enhanced the osteogenic differentiation of hMSC. Hence, in the present study, 0.1 and 1 mM $SrCl_2$ and $CeCl_3$ salts were supplemented in addition to 10 mM $MgSO_4$ to explore the osteogenic ability of the relevant concentration of Sr and Ce ions based on the alloy compositions of the Mg-Zn alloys.

5.2 MATERIALS AND METHODS

5.2.1 Design and synthesis of alloys

Table 5.1 Abbreviated notation and chemical composition of the Mg-Zn alloys.

Alloys	*Mg*	*Zn*	*Sr*	*Ce*	*Zr*
Mg-Zn-Zr	Bal	4	-	-	0.5
Mg-Zn-0.25Sr-Zr	Bal	4	0.25	-	0.5
Mg-Zn-1Sr-Zr	Bal	4	1	-	0.5
Mg-Zn-0.25Ce-Zr	Bal	4	-	0.25	0.5
Mg-Zn-1Ce-Zr	Bal	4	-	1	0.5

Table 5.1 tabulates the abbreviated notation and chemical composition of the Mg-Zn alloys that are studied in the current chapter. Mg-Zn-Sr-Zr and Mg-Zn-Ce-Zr (Sr, Ce = 1, 0.25) alloys were melted in a mild steel crucible using an electrical resistance furnace and casted in a mild steel mold preheated at 500 °C. Pure elemental ingots of Mg (US magnesium Inc. 99.97%), Zn shots (Alfa-Aesar 99.99%), and Mg-30Sr/Mg-30Ce master alloys were weighed accordingly and homogenized at 700 °C to synthesize Mg-Zn-Sr-Zr and Mg-Zn-Ce-Zr alloy in 250g batch size. At equilibrium, Zirmax® Mg-33.3 wt% Zr (Magnesium Elektron, UK) was added to the molten mixture. Stirring for 10 s after 1 min and 5 min was performed to achieve uniform dispersion and

dissolution of zirconium particles in the melt. Finally, the temperature was maintained at 700 °C for 30 minutes and then casted. Following the solution treatment at 300 °C for 1 hour, hot extrusion was performed using an extrusion ratio of 30:1 at North Carolina A&T University (Greensboro, NC).

5.2.2 X-ray diffraction

X-ray diffraction (XRD) phase analysis was performed using Philips XPERT PRO system employing the Cu K_α (λ=1.54056 Å) radiation source with a Si-detector. X-ray generator was operated at 45 kV and 40 mA at a 2θ range of 10-80°. X'Pert HighScore Plus version 3.5 software was used to identify the XRD patterns comparing to ICSD database.

5.2.3 ICP analysis

Elemental analysis on the alloy compositions of was performed using inductively coupled plasma optical emission spectrometry (ICP-OES, iCAP duo 6500, Thermo Scientific). ZK40, ZJ40/41, and ZY40/41 alloy specimens were dissolved in 1% nitric acid. The solutions were then analyzed for the concentration of Mg, Zn, Zr, Ce, Sr, Fe, Mn, Ni, Al, and Cu using known standards.

5.2.4 Microstructure analysis

The microstructure of heat-treated (T6) and extruded ZK40, ZJ40/41, and ZY40/41 alloys were mounted in epoxy (EpoxiCure, Buehler), and mechanically polished with 9, 3, and 1 μm diamond slurry followed by 0.5 µm colloidal silica to obtain a mirror-like finish using semi-automatic polishing system (Vector, Buehler). Specimens were then subjected to chemical etching in a solution of 5 mL acetic acid, 6 g picric acid, 10 mL water, and 100 mL ethanol followed by washing immediately using isopropanol to clean the surface. The microstructure of the heat-treated (T6) and extruded ZK40, ZJ40/41, and ZY40/41 alloys were observed using optical microscopy (Nikon, Japan). The polished and etched microstructure of ZK40, ZJ40/41, and ZY40/41 alloy specimens were also analyzed using a scanning electron microscop (JSM 6610LV, JEOL, Japan) equipped with an energy dispersion spectrometer (INCA, Oxford Instruments) to identify the secondary precipitates within the grain boundaries. Computer tomographic (Phoenix Nanotom-m 180 kV / 15 W X-ray nanoCT® system, GE) images were also captured with a minimum voxel resolution ~ 80 um to analyze presence of any inclusions, voids, and secondary precipitates in the as cast, annealed ingots.

5.2.5 Immersion corrosion measurement

Immersion corrosion properties of heat-treated (T6) and extruded ZK40, ZJ40/41, and ZY40/41 alloys were assessed in conformation with ASTM G31-72 (71). Heat-treated (T6) and extruded ZK40, ZJ40/41, and ZY40/41 alloys were prepared in disks, 5 mm in diameter and 1.5 mm in thickness. These disks were polished up to 1200 grit using SiC paper. Surface area and the weight of each specimen were measured prior to the immersion tests. The specimens were then cleaned in acetone using a sonicator bath and sterilized under UV for 30 min each side. After sterilization, the specimens were immersed for 1, 3, and 5 weeks in Hank's Balanced Salt Solution (HBSS) at 37.4 °C. The HBSS media volume to surface area ratio was maintained at 20 ml/cm^2. The immersed specimens were subsequently removed from HBSS media at each time point, rinsed with distilled water, and dried at room temperature. Further, the degradation product of each specimen was cleaned with 200 g/L of chromic acid and 10 g/L of $AgNO_3$ solution for 10 min to assess the mass loss (56) similar to the procedure described in Chapter 3 and 4. The difference in mass before and after immersion was recorded, and the degradation rate were calculated using the mass loss, density and surface area according to ASTMG31-72 (71). Averages and standard deviations of 3 sample measurements were reported and one-way ANOVA with Tukey's post-hoc test was used to determine any significant mean differences with a p-value less than 0.05 for each time point.

5.2.6 Tensile testing

Tensile testing was conducted in accordance with ASTM-E8-04. ZK40, ZJ40/41, and ZY40/41 alloys were machined into a standard dog-bone shape with a gauge length of 13.5mm, width of 3mm, and thickness of 3mm. Uniaxial tensile testing was performed using an Instron machine employing a 5kN load cell at room temperature at a cross-head speed of 1.3mm/min. Yield strength (YS), ultimate tensile strength (UTS), Young's modulus (E), and percent elongation (%) were obtained from the stress-strain curve obtained for each specimen. Young's modulus was also determined from the initial linear portion of the curves. Average and standard deviations of these 3 sample measurements are reported in the results sections to follow. Averages and standard deviations of 3 sample measurements were reported and one-way ANOVA with Tukey's post-hoc test was used to determine any significant mean differences with a p-value less than 0.05 for each time point.

5.2.7 MTT cell viability test

In order to study the cytocompatibility of extruded ZK40, ZJ40/41, and ZY40/41 alloys, murine osteoblast-like cell line, MC3T3 (ATCC, Rockville, MD), was cultured with the extract media prepared by immersing the alloy specimens in culture medium and incubating them for 72h. Modified Eagle's medium alpha (αMEM) with 10% FBS and 100 U ml^{-1} penicillin–streptomycin was used as cell culture media. The alloy specimens were machined into disks,10 mm diameter and 5 mm thickness, and polished up to 1200 grit using SiC paper. The ratio of culture media volume to specimen weight was maintained at 1 mL to 0.2 g in conformation with EN ISO 10993:12. The extract media was filtered using 0.2 μm membrane with this original extract being considered as 100% extract. The chemical concentration of Mg, Zn, Zr, Sr, and Ce in the 100% extract was then measured using an inductively coupled plasma – optical emission spectroscopy (ICP-OES) similar to the procedure described earlier in Chapters 3 and 4. The 100% extract was further diluted to 50%, 25%, and 10% extract solutions. MC3T3 cells were seeded in a 96-well plate with a cell density of 6,000 cells per well and incubated for 24 h. The MC3T3 cells were further incubated with the 100%, 50%, 25%, and 10% extract media. After 72 h of incubation, Vybrant MTT Cell Proliferation Kit (Invitrogen Corporation, Karlsruhe, Germany) was used to assess the cell viability. Prior to the MTT assay, the extract media was replaced with fresh culture media to prevent any interaction between Mg ions and 3-(4,5-dimethylthiazol-2-yl)-2,5-diphenyltetrazolium bromide (MTT). 110 μL of 1.2 mM MTT in phosphate buffered saline (PBS) was then added to each well and incubated for 4 h of incubation. Sodium dodecylsulfate–hydrochloric acid solution solution was then added and incubated for 12 h to solubilize the formazan crystal. The absorbance of formazan dye was then measured at a wavelength of 570 nm using Synergy 2 microplate reader (BioTek Instruments, Winooski, VT) similar to the procedure described earlier. Averages and standard deviations of 3 sample measurements were reported and one-way ANOVA was used to determine any significant mean differences with a p-value less than 0.05 for each dilution factors of the extract media.

5.2.8 Human mesenchymal stem cell culture with salt solution

Human mesenchymal stem cells (Lonza, Allendale NJ) were used to assess the effect of Mg, Sr, and Ce ions on the osteogenic differentiation of hMSCs. The third passage cells were cultured with both growth and differentiation media that contain Mg, Ce, and Sr ions. Modified Eagle's medium alpha (αMEM) with 20% FBS and 100 U ml^{-1} penicillin–streptomycin was used as the growth media. 100 nM dexamethasone, 50 μM ascorbic acid, and 10 mM β-glycerophosphate were further added to the growth media to generate the osteogenic media. Additionally, 10 mM $MgSO_4$, 0.1/1 mM $SrCl_2$, or 0.1/1 mM $CeCl_3$ were added to the differentiation media as tabulated in Table 5.2. hMSCs were seeded at the cell density of 6000 cells per cm^2, and cultured with the growth media for 7 days. Following this, the growth media was replaced with the sample media and cultured for another 7 and 14 days to investigate the alkaline phosphatase activity and osteogenic gene expression. Averages and standard deviations of 3 sample measurements were reported and one-way ANOVA with Tukey's post-hoc test was used to determine any significant mean differences with a p-value less than 0.05 for each time point.

Table 5.2 Abbreviated notation and chemical formulation of sample media.

Abbreviated notation for sample media	Sample media formulation
GM	Growth media
DM	Differentiation media
DM-Mg	10 mM $MgSO_4$ in the differentiation media
DM-Mg-0.1Sr	10 mM $MgSO_4$ and 0.1 mM $SrCl_2$ in the differentiation media
DM-Mg-1Sr	10 mM $MgSO_4$ and 1 mM $SrCl_2$ in the differentiation media
DM-Mg-0.1Ce	10 mM $MgSO_4$ and 0.1 mM $CeCl_2$ in the differentiation media
DM-Mg-1Ce	10 mM $MgSO_4$ and 1 mM $CeCl_2$ in the differentiation media

5.2.8.1 Alkaline phosphatase measurement

Alkaline phosphatase (ALP) activity was assessed using an enzymatic assay measuring the conversion of p-nitrophenyl phosphate (pNPP) as a phosphatase substrate. hMSC cells were washed with PBS and lysed using a lysis buffer (CelLytic M, Sigma Aldrich) to prepare the cell lysate containing ALP. pNPP substrate solution was added to the cell lysate to assess the enzymatic reaction. After 30 m incubation, 0.3N NaOH solution was then supplemented to stop the enzymatic reaction, and measure the absorbance at 405 nm. pNPP standard solutions with different concentrations were prepared by diluting the pNPP substrate solution with 0.02N NaOH solution. The ALP activity was determined by comparing the absorbance to the standard curve, and normalized by total double-stranded DNA.

5.2.8.2 Gene expression study using qRT-PCR

Table 5.3 Primer sequences of GAPDH, ALPL and OPN of hMSC.

	Forward Primer (5’-3’)	**Reverse Primer (5’-3’)**
GAPDH	ATGGGGAAGGTGAAGGTCG	TAAAAGCAGCCCTGGTGACC
Alkaline phosphatase (ALPL)	GACCCTTGACCCCCACAAT	GCTCGTACTGCATGTCCCCT
Osteopontin (OPN)	CTCAGGCCAGTTGCAGCC	CAAAAGCAAATCACTGCAATTCTC

hMSCs were cultured with growth media and differentiation media with the different alloying element salts mentioned above in the section 5.2.8. RNA isolation was performed on these hMSCs using a commercially available RNA extraction kit (Nucleospin RNA Extraction Kit, Macherey Nagel). RNA concentration was measured using a microplate reader (Synergy 2, BioTek Instruments) at the wavelength of 260 and 280 nm. Approximately 50 ng of RNA was used for each reverse transcription reaction. Reverse transcription was performed using a commercially available kit (Improm-II Reverse Transcription Kit, Promega). After that, complementary DNAs were subjected to qPCR reactions using SYBR green mastermix (Brilliant II, Agilent) and the primers as listed in Table 5.3.

5.3 RESULTS

5.3.1 Phase and elemental analysis

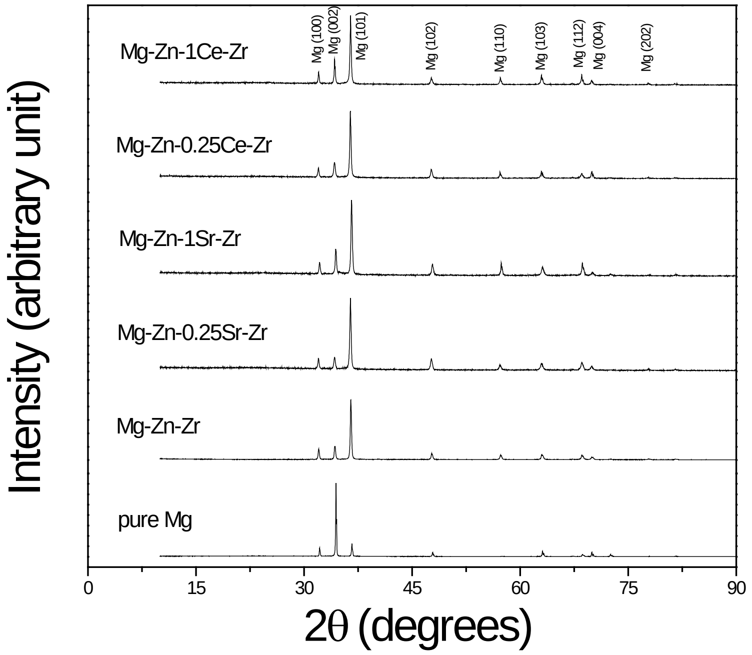

Figure 5.1 X-ray diffraction patterns of as-extruded**.**Mg-Zn-Zr, Mg-Zn-Sr-Zr, and Mg-Zn-Ce-Zr.

Figure 5.1 shows x-ray diffraction (XRD) patterns of the base alloy Mg-Zn-Zr (ZK 40), Mg-Zn-Sr-Zr, and Mg-Zn-Ce-Zr alloys after extrusion. The patterns were identified as a single phase α-Mg matrix with hcp crystal structure of pure Mg. Mg-Zn-Zr, Mg-Zn-Sr-Zr, and Mg-Zn-Ce-Zr alloys exhibited presence of no distinct intermetallic phases in combination with Mg, Zn, Ce, Sr, or Zr. The XRD patterns clearly exhibits that α−Mg solid solution single phase was formed in all of the different alloy systems and no detectable amount of any intermetallic content was observed. However, unlike pure Mg, the highest peak intensity for Mg-Zn-Zr, Mg-Zn-Sr-Zr, and Mg-Zn-Ce-Zr alloys was observed for the (101) pyramidal plane. This observation suggests that the orientation of the $\alpha-$Mg solid solution single phase was altered during alloy synthesis and processing.

Back-scattered electron (BSE) microscopy was employed to observe the microstructure of the extruded Mg alloys to show the influence of the various alloying elements and perform elemental analysis on the alloy matrix and precipitates. In Figure 5.2, the BSE images of the Mg alloys analyzed in the matrix indicated as M and in the precipitates indicated as P revealed the presence of intermetallic precipitates as high contrast areas along the grain boundaries. Increase in precipitate amounts were observed with an increase in Sr and Ce amount (Figure 5.2a vs. 5.2b-e). Mg-Zn-Zr showed the formation of solid solution close to its nominal composition and Zn-rich Mg_7Zn_3 precipitates similar to the case described in Chapter 3 for the ZK40 alloy. 0.25 wt.% Sr addition to Mg-Zn-Zr had no effect on the alloy matrix but caused the presence of Sr and less Zn contents in the precipitate (Figure 5.2b). Further increasing the Sr content to 1 wt.% Sr addition did not seem to alter the composition of the solid solution or precipitates much showing similar composition range. However, an increased number of precipitate sites were observed (Figure 5.2d). Cerium addition also exhibited similar effect on the precipitate indicating presence of Ce and decreased amounts of Zn compared to Mg-Zn-Zr (Figure 5.2c,e). Mg-Zn-Ce-Zr exhibited more precipitates compared to Mg-Zn-Sr-Zr (Figure 5.2b,d vs. 5.2c,e). Thus, Ce addition was observed to cause more precipitates compared to Sr addition due to the higher solid solution limits of Ce with Mg.

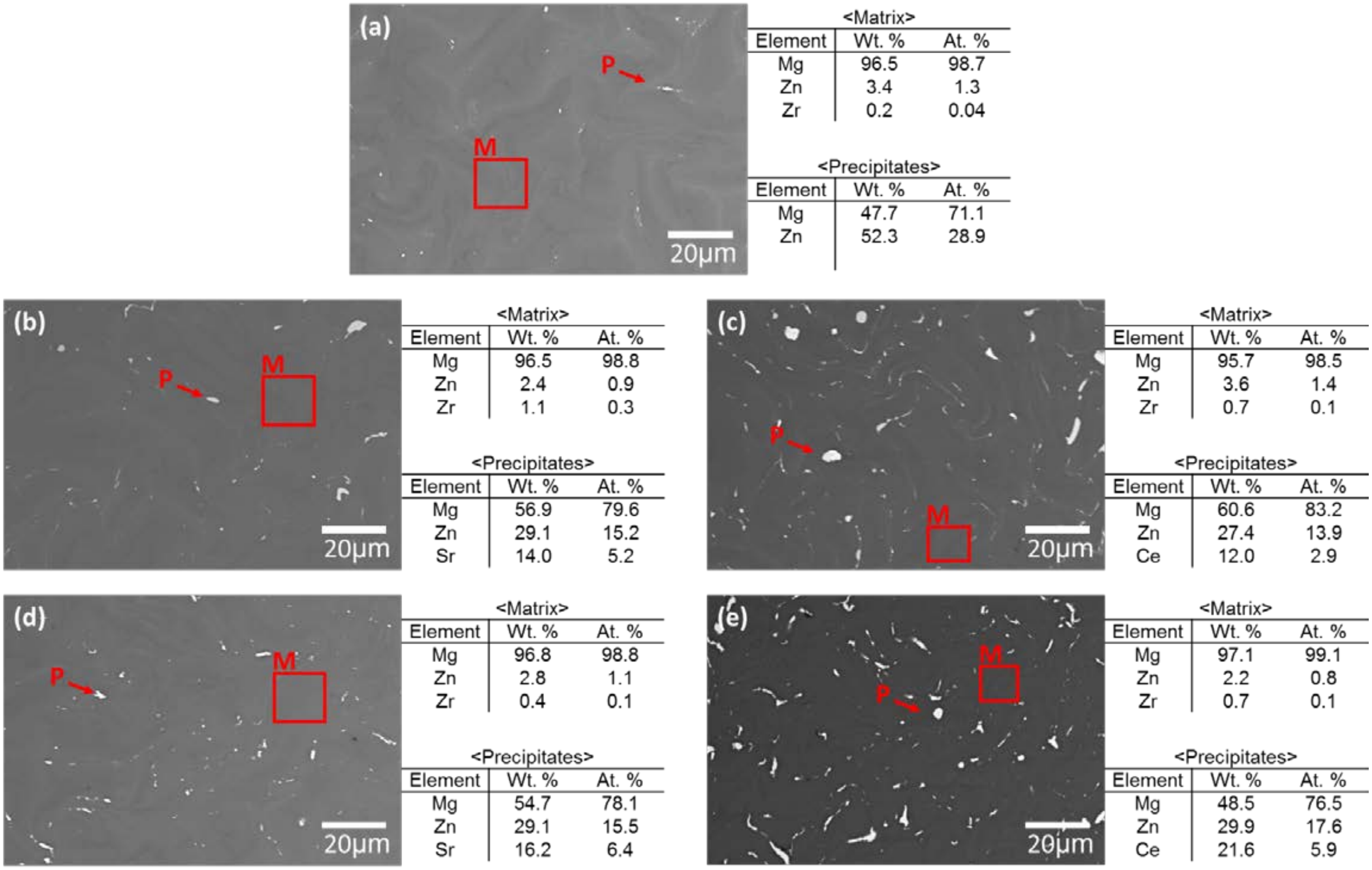

(a)

<Matrix>

Element	Wt. %	At. %
Mg	96.5	98.7
Zn	3.4	1.3
Zr	0.2	0.04

<Precipitates>

Element	Wt. %	At. %
Mg	47.7	71.1
Zn	52.3	28.9

(b)

<Matrix>

Element	Wt. %	At. %
Mg	96.5	98.8
Zn	2.4	0.9
Zr	1.1	0.3

<Precipitates>

Element	Wt. %	At. %
Mg	56.9	79.6
Zn	29.1	15.2
Sr	14.0	5.2

(c)

<Matrix>

Element	Wt. %	At. %
Mg	95.7	98.5
Zn	3.6	1.4
Zr	0.7	0.1

<Precipitates>

Element	Wt. %	At. %
Mg	60.6	83.2
Zn	27.4	13.9
Ce	12.0	2.9

(d)

<Matrix>

Element	Wt. %	At. %
Mg	96.8	98.8
Zn	2.8	1.1
Zr	0.4	0.1

<Precipitates>

Element	Wt. %	At. %
Mg	54.7	78.1
Zn	29.1	15.5
Sr	16.2	6.4

(e)

<Matrix>

Element	Wt. %	At. %
Mg	97.1	99.1
Zn	2.2	0.8
Zr	0.7	0.1

<Precipitates>

Element	Wt. %	At. %
Mg	48.5	76.5
Zn	29.9	17.6
Ce	21.6	5.9

Figure 5.2 Back-scattered electron microscopy of (a) Mg-Zn-Zr, (b) Mg-Zn-0.25Sr-Zr, (c) Mg-Zn-0.25Ce-Zr, (d) Mg-Zn-1Sr-Zr, and (e) Mg-Zn-1Ce-Zr.

5.3.2 Immersion corrosion measurement

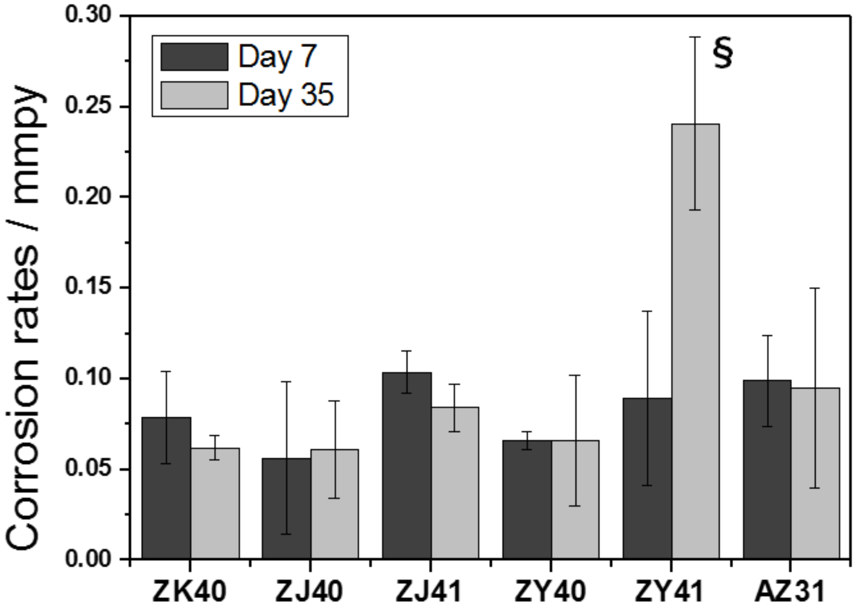

Figure 5.3 Immersion corrosion rates of Mg-Zn-Zr, Mg-Zn-Sr-Zr, and Mg-Zn-Ce-Zr (n = 3, §$p<0.05$ denotes a significant difference with all other groups).

An effect of adding Ce and Sr as micro alloying elements on the corrosion resistance of Mg-Zn-Zr alloy was investigated using immersion corrosion measurement in HBSS for 7 and 35 days. In Figure 5.3, mass loss of the Mg alloys were converted to immersion corrosion rates in millimeter per year (mmpy) as described in earlier chapter 4. Mg-Zn-Sr-Zr alloys does not exhibit any significant difference in the corrosion rate compared to Mg-Zn-Zr. On the other hand, Mg-Zn-1Ce-Zr exhibits a significant increase in corrosion rate after 35 days of immersion whereas Mg-Zn-0.25Ce-Zr still maintained comparable corrosion resistance with other Mg alloys. As observed and discussed in section 5.3.1 in the BSE images, more secondary phase contents in the case of Mg-Zn-1Ce-Zr results in a catastrophic corrosion initiated from the Mg-Zn-Ce mixtures along the grain boundaries. Overall, the addition of 0.25 and 1 wt.% of Sr as well as 0.25 wt.% of Ce did not deteriorate the corrosion resistance significantly compared to commercial AZ31.

5.3.3 Tensile mechanical properties

Mechanical properties of the different alloys was determined using tensile tests, the results of which as tabulated in Table 5.4. Mg-Zn-Zr alloy (ZK 40) exhibited an elastic modulus of 45.8 GPa, yield strength of 286.6 MPa (YS), and an ultimate tensile strength of 327.2 MPa (UTS), and 9.3% elongation. Addition of 0.25 wt. % and 1 wt. % Sr to the Mg-Zn-Zr only resulted in a slight decrease in UTS to 317.3 MPa and 320.9 MPa. There were no significant difference in modulus, YS, and elongation. On the other hand, addition of 0.25 wt. % and 1 wt. % Ce to Mg-Zn-Zr exhibited a significant increase in UTS to 335.2 MPa and 341 MPa, respectively. A significant decrease in elongation from 9.3% to 7.6% was also observed in the case of Mg-Zn-1Ce-Zr.

Table 5.4 Tensile properties of Mg-Zn-Zr, Mg-Zn-Sr-Zr, and Mg-Zn-Ce-Zr alloys (n=3, §$p<0.05$ denotes a significant difference with all other groups).

Materials	Modulus (GPa)	Yield Tensile Strength (MPa)	Ultimate Tensile Strength (MPa)	Elongation (%)
Mg-Zn-Zr	45.8±5.2	286.6±8.0	327.2±6.2	9.3±3.5
Mg-Zn-0.25Sr-Zr	42.4±3.6	292.8±6.2	317.3±2.4	12.6±2.1
Mg-Zn-1Sr-Zr	41.0±2.5	292.7±9.5	320.9±1.9	9.5±1.0
Mg-Zn-0.25Ce-Zr	39.7±4.0	271.9±7.1	335.2±0.4 §	10.2±1.0
Mg-Zn-1Ce-Zr	45.9±4.3	282.5±3.3	341.7±2.9 §	7.6±1.1 §

5.3.4 MTT assay

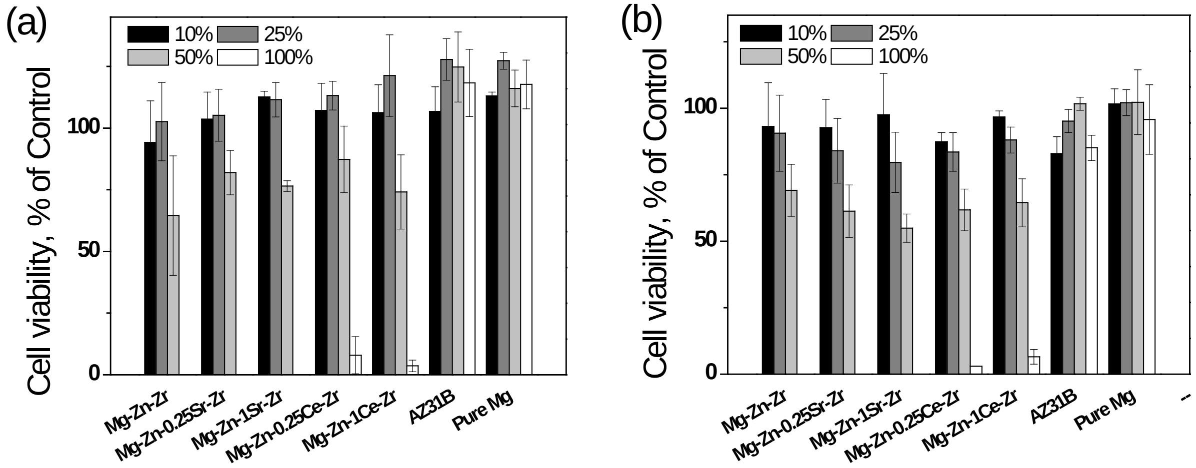

Figure 5.4 MC3T3 cell viability of Mg-Zn-Zr, Mg-Zn-Sr-Zr, and Mg-Zn-Ce-Zr after (a) 1 day and (b) 3 days (n=3).

MC3T3 cell viability was assessed using MTT assay after culturing the cells for 1 and 3 days with extract media containing the degradation products of Mg-based alloys. Compared to the growth media as negative control, the MTT assay result was plotted as shown in Figure 5.4. 100% extract media of Mg-Zn-Zr, Mg-Zn-Sr-Zr, and Mg-Zn-Ce-Zr alloys, as expected in contrast to commercially available AZ31B or pure Mg, exhibited less than 10% cell viability immediately even after 1 day culture (Figure 5.4a). The cell viability of these alloys was however restored to ~50% with 50% extract media and increased to ~90% with 25% and 10% extract media. Figure 5.4b showed similar cell viability pattern for the MTT assay after 3 days of culturing the MC3T3 with the extract media. Fischer et al. (121) suggested 10% extract media is suitable to determine the cytotoxicity of biodegradable Mg alloys due to the nature of the static culture causing cell necrosis induced by osmotic shock of total metal salt concentration as discussed in Chapter 4. ISO 10993:5 protocol determines that achieving 75% or higher cell viability is generally considered non-cytotoxic. Hence, the cell viability of 10% extract media suggests that these alloys are indeed cytocompatible with the MC3T3 cell line.

5.3.5 ALP activity measurement

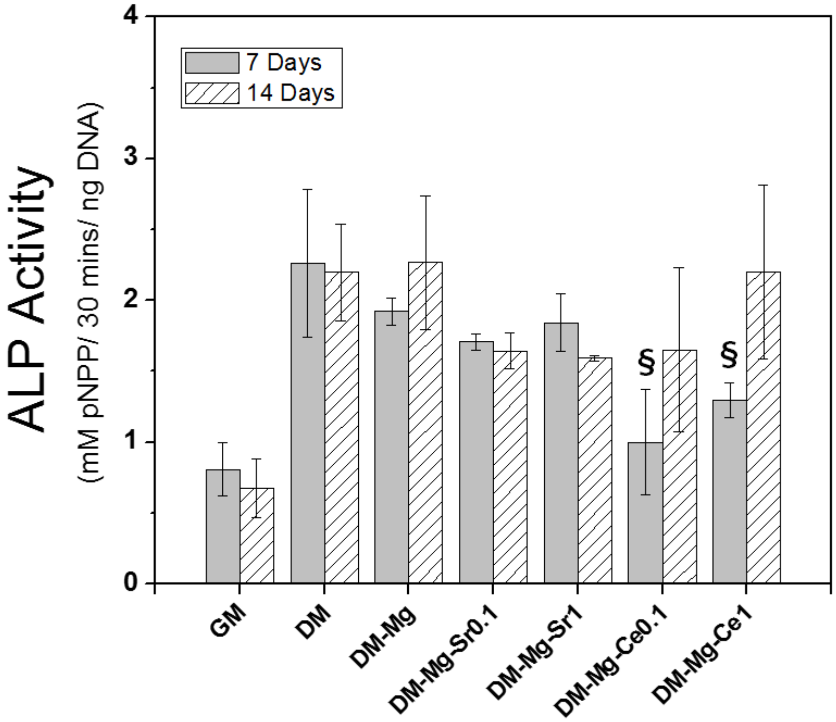

Figure 5.5 ALP activity of hMSCs cultured for 7 and 14 days with osteogenic media supplemented with Mg, Sr, and Ce ions (n=3, §$p<0.05$ denotes a significant difference with differentiation media control).

Human mesenchymal stem cells were (hMSC) cultured with growth media for 7 days. ALP expression levels were measured after 7 and 14 days of culturing the hMSCs with osteogenic differentiation media containing alloying elements (Figure 5.5). Although higher ALP level was observed compared to growth media for all the salt concentrations, there was no significant improvement in ALP expressions in the differentiation media groups with the addition of the alloying element salts. Lower level of ALP activity was observed in differentiation media containing $CeCl_3$ after 7 days but the ALP level was restored compared to differentiation media after 14 days. No other significant difference in ALP expressions was caused by the addition of Mg and Sr ions

5.3.6 Gene expression

Alkaline phosphatase (ALPL) and osteopontin (OPN) gene expression are shown in Figure 5.6. Fold changes of ALPL and OPN was obtained by subtracting GAPDH housekeeping gene expression and subtracting the average of the growth media groups. ALPL expression exhibited a significant increase in DM-Mg-1Sr group. In the case of OPN, Mg, 0.1/1 mM Sr, and 0.1 mM Ce supplemented media exhibited significantly enhanced expression level whereas Ce supplemented media exhibited no significant improvement.

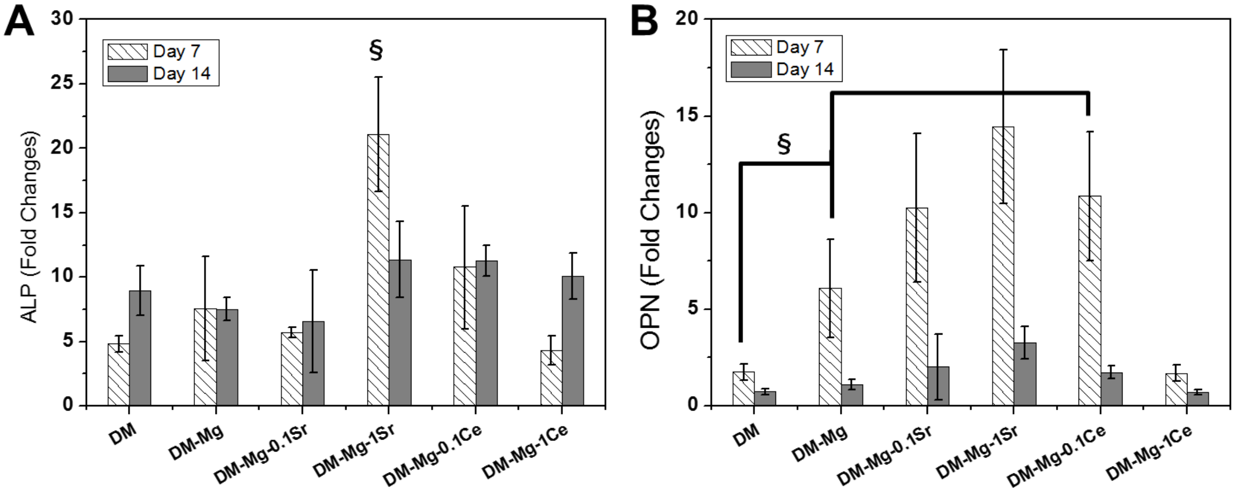

Figure 5.6 (a) ALPL and (b) OPN gene expression of hMSC cultured for 7 and 14 days with osteogenic media supplemented with Mg, Sr, and Ce ions (n=3, §$p<0.05$ denotes a significant difference with differentiation media control).

5.4 DISCUSSION

5.4.1 Effect of Sr and Ce on corrosion resistance and mechanical properties

The present study has been conducted with one of the primary goals being to explore the effect of Sr and Ce additions to Mg based alloys particularly, the Mg-Zn-Zr system. Additionally, the goal is to study the corrosion resistance, mechanical properties, cytocompatibility and more importantly, also investigate the osteogenic response of incorporation of gradually adding Sr and Ce to biodegradable Mg-Zn-Zr alloys. As discussed in the earlier Chapters 3 and 4, Mg-Zn-Zr is a commercially available Mg alloy system that was developed and used for structural applications. Its potential use as a biodegradable metal was identified as discussed in Chapters and 3 and 4 primarily owing to its suitable corrosion resistance, mechanical properties and cytocompatibility. As discussed in Chapter 3 and 4, Mg-Zn (Mg_7Zn_3) secondary phase precipitates are observed to form in the grain boundary area. These precipitates are vulnerable to galvanic corrosion and serve as initiators for pitting corrosion. Hence, as discussed in Chapter 2 in the specific aims section, Sr and Ce have been selected as microalloying elements to alter the composition of these precipitates. Strontium (Sr) refines the grain sizes of Mg alloys and Ce can form stable oxides due to the higher bond energies and bond strengths and affinity of Ce to form cerium oxides thus serving to protect the Mg-Zn-Zr alloy from corrosion. In addition, Sr and Ce have been reported to have a positive effect on the proliferation and osteogenic differentiation of human mesenchymal stem cells.

Strontium (Sr) and Cerium (Ce) were both used as micro alloying elements in the amount of 0.25 wt.% and 1 wt.%. Only small amount of Sr and Ce were used due to the low solubility limit of these alloying elements exceeding which can form more secondary phase precipitates which can deteriorate corrosion resistance leading to galvanic corrosion. Phase analysis was performed on the Mg-Zn-Sr/Ce alloy system using an x-ray diffraction. As shown in Figure 5.1, no distinct second phase or unalloyed single elements or multiphase alloys or compounds were observed in the Mg-Zn-Zr, Mg-Zn-Sr-Zr, and Mg-Zn-Ce-Zr alloy systems. However, presence of second phase precipitates along the grain boundaries of the Mg alloys were still revealed under back-scattered scanning electron (BSE) microscopy as shown in Figure 5.2 possibly due to the processing conditions of melting and casting not allowing enough time for complete homogenization of the melt or possibly during extrusion of the alloy, the time, temperature and reduction ratios selected exacerbated causing instabilities to the precipitates leading to further break down and distribution of the precipitate particles within and around the grain boundaries.

The composition of the precipitates in the Mg-Zn-Zr alloy system thus transformed the precipitate compositions to ternary mixtures of Mg, Zn, and Sr/Ce in Mg-Zn-Sr/Ce-Zr alloy systems thus leading to precipitates of Mg-Zn-Sr in the case of Mg-Zn-Sr-Zr system and Mg-Zn-Ce in the Mg-Zn-Zr-Ce system. Although the chemical composition of the precipitates were more similar to the composition of the base alloy (Mg-Zn-Zr (ZK 40) system) in each alloy, more number of precipitates were observed in the BSE images. Ce addition was more prone to form grain boundary precipitates compared to Sr addition (See Figure 5.2b, d vs. 5.2c, d). As a result of these precipitates from Sr and Ce addition, the immersion corrosion measurements exhibited no significant improvements in corrosion resistance. Except for Mg-Zn-1Ce-Zr alloy composition, the corrosion rates in general for all the other compositions and additions of Sr and

Ce were comparable to commercially available AZ31 without displaying any significant difference. Mg-Zn-1Ce-Zr in fact, demonstrated increase in corrosion rates after 35 days of immersion due to the higher volume of precipitates formed as seen in the BSE images.

Precipitates at the grain boundary can also serve to impede dislocation movement as is well-known in the literature leading to improvement in the mechanical strength of Mg alloys. It is well-known from physical metallurgical principles, precipitation hardening is routinely used to increase precipitation of second phase precipitates from alloying elements or inclusions or impurity phases by performing heat treatment above the melting point of a specific alloying element via the time-temperature-transformation (TTT) diagrams. Although such optimizations were not performed in this study, the initial results presented here clearly show that such optimizations can be conducted to indeed reap the potential of these optimization studies of the addition of Sr and Ce. Nevertheless, it can be seen that the addition of Sr to Mg-Zn-Zr exhibited no significant difference in tensile properties. On the other hand, the ultimate tensile strength was significantly improved to 335 MPa and 342 MPa with Ce – 0.25 wt% and 1 wt% additions, respectively. However, as is usually the case with the 1 wt.% of Ce addition, a decrease in elongation was obtained to offset the grain boundary strengthening.

5.4.2 Cytocompatibility and osteogenic potential of Sr and Ce additions to Mg-Zn-Zr alloys

Toxicity of biomaterials are often examined using *in vitro* experiments prior to initiation of *in vivo* experiments. In this regard, ISO 10993 protocols have been developed and used for screening polymeric and metallic biomaterials based on the cell viability shown using the MTT assay (140). Fischer et al. initially reported that MTT assay followed by direct cell culture with

Mg alloy materials can result in a false positive due to Formazan salt conversion by actively corroding Mg ions serving to interfere with the assay results (110). Fischer et al. also addressed that osmolality issue of Mg ions causing osmotic shock to the cells although Mg alloys implanted in the animal exhibits no significant tissue damage (121). Hence, in this study the work has focused on the indirect MTT assay results indicating cell viability with 10% extract media serving as a better acceptable indicator to rank the toxicity of Mg alloys. It has been widely accepted that *in vitro* degradation and cytocompatibility exhibited by Mg during the static immersion tests do not really represent the *in vivo* implantation response of biodegradable Mg alloys (110, 141). Mg alloys on the other hand, tend to degrade in a much slower rate during *in vivo* implantation and hence, exhibit minimal inflammatory response.

Cytocompatibility of the Mg alloys have been examined using MC3T3 cell line in compliance with the ISO standard with modifications. MTT assay after 3 days of culturing MC3T3 cells with the 10% extract media exhibited good cytocompatibility in all the Mg alloys studied compared to pure Mg. Pure Mg and commercial AZ31 were used as experimental control groups and exhibited the cell viability higher than 75% when using 100% extract media.

In addition to cytocompability, osteogenic effect of the alloying elements such as Mg, Sr, and Ce was investigated by culturing the human mesenchymal stem cells (hMSC) with osteogenic media supplemented with $MgSO_4$, $SrCl_2$, and $CeCl_3$. However, Zr or Zn ions were not considered for this study since there are no reports on their influence on osteogenic differentiation of hMSCs. Concentration of $MgSO_4$ was maintained at 10mM as reported to be optimal for hMSC proliferation (142). $SrCl_2$ and $CeCl_3$ are dissolved in the osteogenic media with 10mM $MgSO_4$ to reach concentrations of 1 or 0.1 mM since Sr and Ce content in Mg-Zn-Sr/Ce-Zr alloys is limited to 1 wt.% in the present study. Further, hMSC is used instead of

MC3T3 since hMSC has the ability to differentiate into multiple lineage whereas MC3T3 is already in the early stage of osteoblast. Confluent hMSCs were cultured with the supplemental media for 7 and 14 days as mature osteoblast can be obtained after 14 days of culturing hMSC in osteogenic media (143).

Alkaline phosphatase was measured after culturing hMSC for 7 and 14 days since it is an early marker for osteogenic diffentiation of hMSC (144). Compared to growth medium, osteogenic media and supplemented media exhibited higher ALP activity. However, no significant improvement in ALP activity was observed with osteogenic media supplemented with Mg, Sr, or Ce (see Figure 5.5). Hence, the gene expression was quantified using qRT-PCR to investigate any osteogenic effect of these elements. ALPL expressions normalized by GAPDH housekeeping gene seemed to be significantly upregulated with 1mM Sr containing media as shown in Figure 5.6. Overall, osteogenic media supplemented with Mg, Sr, and Ce ions however, exhibited no additional improvement in ALP activity and mRNA expression.

5.5 CONCLUSIONS

The effect of adding Sr and Ce as micro alloying element to biodegradable Mg-Zn-Zr alloy has been studied in terms of corrosion and mechanical properties as well as biological influence of these alloying elements contributing to mineralization and exhibiting any osteogenic potential. Using these micro alloying elements, it was observed that second phase precipitates were formed. The precipitates appeared to be successfully formed owing to the solubility of Sr and Ce in the binary Mg-Zn phase system to correspondingly form Mg-Zn-Sr/Ce ternary phase precipitates in the presence of Zr as well. Unfortunately, it appears that the introduction of additional alloying elements induced formation of more precipitates along the grain boundaries. Thus, a significant improvement in corrosion resistance was not observed though anticipated. On the other hand, the mechanical properties were improved due to the large volume of precipitates formed confirmed by the back scattered SEM analysis showing formation of Mg-Zn-Sr and Mg-Zn-Ce precipitates for Sr and Ce addition. Cytocompatibility of Mg-Zn-Zr was found to be not affected by adding Sr or Ce. Zn however, exhibited low tolerance in the cell viability after culturing MC3T3 cells with different alloying element in the form of chloride salts dissolved in the culture media. Thus, similar cell viability in MTT assay was obtained due to the constant Zn content in Mg-Zn-(Sr/Ce)-Zr alloys. ALP activity and ALPL gene expression exhibited no significant improvement whereas OPN gene exhibited some improvement after culturing hMSCs with osteogenic media supplemented with Mg, Sr, and Ce salts signifying that the alloying elements do not have any potential adverse contribution to the mineralization potency of the alloy system. However, *in vivo* studies would be required to ascertain the true osteogenic potential of these alloy systems containing Sr and Ce in addition to Zn and Zr.

6.0 SPECIFIC AIM IV: RAT FEMORAL FRACTURE REPAIR USING INTRAMEDULLARY PINS OF MAGNESIUM-ZINC-STRONTIUM-ZIRCONIUM ALLOY

6.1 INTRODUCTION

Magnesium alloys have been developed for their potential use as biodegradable fracture fixation devices (FFD) (145). Thus far to date, permanent metals such as titanium (Ti), cobalt-chromium (Co-Cr), and stainless steel (SS) have been widely used for fracture fixation in the clinical settings. Although high mechanical strength of these materials is beneficial for load-bearing application, a mismatch in mechanical properties compared to the cortical bone often cause stress shielding effects that tend to damage the surrounding tissues (13, 14). In addition, debris formation from corrosion and wear due to constant use can initiate inflammatory response and foreign body reaction (FBR) that is now synonymous with these bioinert systems (16-18). On the other hand, biodegradable Mg alloys appear to be a paradigm shift in the arena of degradable materials, a term that was more commonplace with polymeric systems. These materials are designed to degrade with degradation products that are also biocompatible and exhibit mechanical properties much closer to the natural bone (38). Furthermore, Mg ions exist in bone naturally and contribute to osteoblast proliferation (142). In order to bringing these benefits of using Mg alloys for orthopedic applications, research and development that has burgeoned significantly over the past decade has focused on identifying and development of biodegradable

Mg alloys that exhibit controlled corrosion and more importantly, demonstrating the true biosafety aspects of Mg and the various alloying elements added to Mg to improve its corrosion and mechanical properties.

Corrosion is the degradation mechanism common to biodegradable Mg alloys. During the reaction of magnesium with water, magnesium hydroxide and hydrogen gas are produced. Rapid corrosion of Mg alloys can develop gas pockets near the implantation site which leads to considerable patient level discomfort and pain due to the consequent pH change and the imminent hydrogen gas evolution state (146). Also, rapid corrosion can cause immature mechanical failure of the devices during the initial fracture healing process, loosening of the device and hardware a ubiquitous problem (147). In order to overcome rapid corrosion of magnesium, altering alloy compositions and the microstructure by choice of the alloy system and the processing conditions have typically been employed (76, 129). Mg-Zn (59-62), Mg-Al (49, 63-65), Mg-Y(66, 67), and Mg-Y (67-70) based alloys have demonstrated their suitable corrosion resistance, mechanical properties, and biocompatibility demonstrating their potential use as a biodegradable metal.

Biosafety of biodegradable Mg alloys have been examined using *in vitro* and *in vivo* experiments. However, a discrepancy between *in vivo* and *in vitro* degradation characteristics of Mg alloys have typically caused a mismatch in the cell viability results and the expected versus actually observed *in vivo* biocompatibility (148). Static culture is limited to mimic physiological conditions for testing Mg alloys. Cell viability is highly dependent on the osmolality of Mg ions in the culture medium (110). Osmotic shock of Mg ions can cause cell necrosis during *in vitro* studies. Also, Mg ions in Mg alloys conflict with Formazaan salt-based assays for *in-vitro* cell viability tests (149). Therefore, *in vivo* studies have been preferred to *in vitro* studies. Toxicity and degradation of biodegradable Mg alloys have been reported using various animal models (57, 131, 150). A few clinical trials of biodegradable Mg-based fixation screws have been also been reported to date. Syntellix AG and U&I corporation have also conducted clinical trials and earned regulatory approvals in Europe and South Korea, respectively (58). Although there are approved non-load bearing fixation devices of biodegradable Mg alloys, more research is critically needed to develop Mg devices for use under load-bearing conditions.

The objective of this study was therefore to investigate the degradation effects, local tissue response, and systemic toxicity of Mg-4Zn-0.25Sr-0.5Zr pins that are implanted in the intramedullary region of the fractured rat femurs. Mg alloys are not intended for use as femoral rods. However, rat femoral fracture model has been selected for this study to primarily understand the degradation profile of Mg-Zn pins and examine the toxicity of Mg-Zn pins under load-bearing conditions. Corrosion of metal is known to be accelerated when mechanical stress is applied commonly termed as stress-corrosion cracking (SCC). In the present study, ZK40 alloy was modified by adding 0.25 wt. % of Sr to improve corrosion resistance as discussed in the earlier Chapter 5. Mg-4Zn-0.5Zr (ZK40) exhibited comparable corrosion resistance and mechanical properties as other biodegradable Mg alloys such as Mg-Y or Mg-Al alloys. Sr also has been reported to stimulate osteoblast proliferation and osteogenic differentiation of human mesenchymal stem cells although the present work was focused primarily on *in vivo* biocompatibility.

6.2 MATERIALS AND METHODS

6.2.1 Alloy processing and fabrication of femoral pins

Mg-4Zn-0.1Sr-0.5Zr (Mg-Zn) alloy was synthesized using an electrical resistance furnace (Wenesco Inc.). Pure Mg (US magnesium Inc. 99.97%), Zn shots (Alfa-Aesar 99.99%), Mg-30Sr master alloy were melted in a mild steel crucible. The total melt amount was 250 g. Melting process was performed using 0.5% SF6 + balance Ar protective gas atmosphere to protect the molten magnesium alloy from oxygen as outlined in Chapters 2-4. The molten mixture of Mg, Zn, and Sr were homogenized at 700 °C and zirconium content was added using Zirmax® (Mg-33.3 wt% Zr) master alloy (Magnesium Elektron Ltd.). After 1 and 5 minutes, the liquid melt was further homogenized by stirring for 10 seconds to dissolve and disperse the zirconium particles uniformly. The melt was maintained at 700 °C for 30 min, following which the molten liquid was poured into a mild steel mold (Ø 44.5 mm × 82.5 mm) preheated at 500 °C.

The middle part of the as-cast Mg-Zn-Sr-Zr (Mg-Zn) alloy following removal of the top, sides and the bottom as outlined in Chapter 2 was machined to a dimension of 37.6 mm diameter and 60 mm height by using a lathe. The as-cast Mg-Zn-Sr-Zr (Mg-Zn) alloy was then heat-treated at 300 °C for 1 hour, quenched in oil, and annealed at 205 °C for 12 hours. Following heat treatment, hot extrusion was performed using an extrusion ratio of 30:1 at North Carolina A&T University (Greensboro, NC).

6.2.2 Animal study design

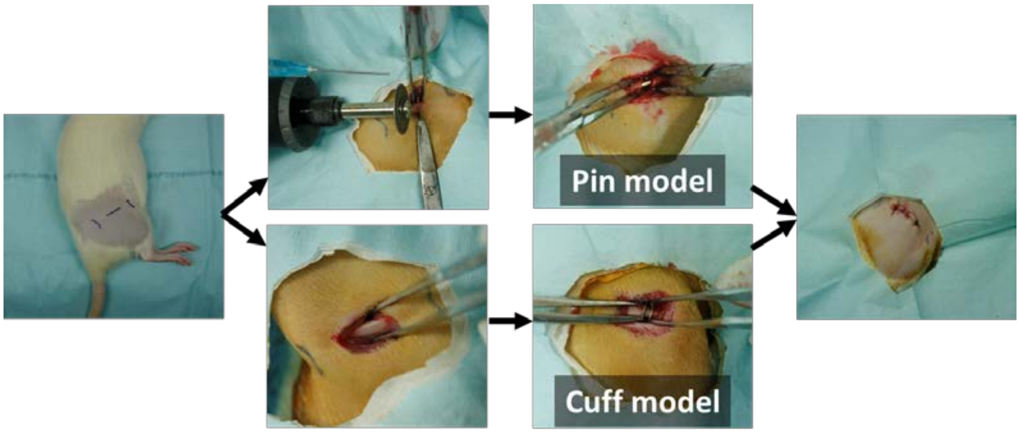

Figure 6.1 Pin and cuff implantation in rat femurs.

The animal study was conducted in accordance with a protocol approved by Animal Care and Use Committee (IACUC) at the University of Pittsburgh. A schematic of the surgical procedure executed is displayed in Figure 6.1. Groups, time points, and number of animals involved in the current chapter are explained in Table 6.1. 30 Sprague-Dawley rats of approximately 250 g of body weight were used. 15 rats were randomly selected for Ti alloy implantation and the other rats were implanted with Mg alloy pins. For each implant material, 10 rats were implanted with pins for 2 and 14 weeks and 5 rats were implanted with the cuff for 14 weeks. For each pin implanted, the right femur of each rat was approached laterally and an osteotomy was performed in the middle of the femur using a dremel drill with a diamond wheel blade. A pin of Ti or Mg alloy was inserted into the intramedullary region to achieve a stable reunion of the fractured femur. 5 rats from both Ti and Mg groups were sacrificed for fracture healing and toxicity analysis after 2 or 14 weeks of implantation. For each cuff implantations, a cuff of Ti or Mg-Zn alloy was implanted around the unfractured femur for toxicity analysis after 14 weeks.

Table 6.1 Groups, time points, and number of animals used for Ti and Mg-Zn device implantation

Group	Time point	N / time point
Ti alloy pins	2 and 14 weeks	5
Mg-Zn pins	2 and 14 weeks	5
Ti alloy cuffs	14 weeks	5
Mg-Zn cuffs	14 weeks	5

6.2.3 Radiographic imaging and computer tomography analysis

X-ray images of all animals were obtained after 7 days to observe implant location and alignment of fractured femurs. The Mg-Zn alloy pins before implantation were scanned using micro-computed tomography (microCT) (VivaCT40; Scanco Medical, Switzerland). The harvested femurs were also scanned using microCT after embedding in plastic. Analysis of the microCT images were performed using Mimics (Materialise, Belgium) to calculate the degradation rate of the Mg alloy pins and assess fracture healing. Averages and standard deviations of 5 sample measurements were reported and t-test was used to determine any significant mean differences with a p-value less than 0.05 for Mg-Zn pin groups at different time points.

6.2.4 Blood test

Blood samples were obtained before operation and after euthanasia at 2 and 14 weeks. The samples collected in K2-EDTA were sent to Marchfield Labs (Cleveland, OH) for hematologic analysis. Red blood cell count, hemoglobin, hematocrit, platelet count, and white blood cell count were analyzed using a Sysmex XT2000i Automated Hematology Analyzer (Sysmex Corporation, Japan). For biochemical analysis, the blood samples were maintained at room temperature to clot for 30 minutes and centrifuged at 2,000 rpm for 10 minutes. The supernatant serum samples were analyzed using an Olympus AU chemistry analyzer (Olympus Corporation, Japan). Alanine aminotransferase (ALT), alkaline phosphatase (ALP), total protein, albumin, total and direct bilirubin, cholesterol, glucose, urea, creatinine, phosphorus, chloride, potassium, sodium, and magnesium were accordingly measured. Averages of 3 sample measurements were reported and compared to the reference ranges for each parameter.

6.2.5 ICP analysis

Harvested liver and kidney tissues were dried in an oven at 70 °C overnight. Dried tissue samples were then ground using a mortar and pestle. 0.5 g of ground tissues were dissolved in 5 mL of concentrated nitric acid that was kept heated at 130 °C for 14 hours, and supplemented with 1 mL of 30% hydrogen peroxide (151, 152). Sample solutions were then diluted 10 times and measured using an inductively coupled plasma optical emission spectroscopy (ICP-OES, iCAP duo 6500 Thermo Fisher, Waltham, MA) with standard solutions of the various elements being analyzed. Averages and standard deviations of 3 sample measurements were reported and one-way ANOVA was used to determine any significant mean differences with a p-value less than 0.05 for all other groups.

6.2.6 Soft tissue histology

Harvested liver and kidney tissues were fixed in 10% neutral buffered formalin for 48 hours. The fixed tissues were sectioned in small pieces, dehydrated in ethyl alcohol series from 70% to 100%, cleaned using xylene substitute and embedded in paraffin. Paraffin tissue blocks were then sectioned using a rotary microtome. Tissue slices were accordingly dewrinkled on a warm water bath, and transferred to glass slides. After drying, tissue slides were imaged using an optical microscope after staining with hematoxylin and eosin (dyes) and mounted using a mounting solution.

6.2.7 Bone tissue histology

Undecalcified embedding was used to perform histology analysis of the harvested femurs with implants. Harvested femurs were fixed in 70% ethyl alcohol for 72 hours. The fixed femurs were then dehydrated in diluted ethyl alcohol from 70% dilution to 100% consecutively. The femurs were cleaned in xylene and embedded in poly methyl methacrylate (PMMA) (OsteoBed, Life Technology). 7 to 10 um tissue sections were obtained from the embedded femurs using a rotary microtome with a tungsten carbide blade. Sections were adhered to tape to prevent shattering during sectioning. Sections were subjected to Goldner’s Masson Trichrome and alkaline phosphatase staining. The stained sections were mounted on a glass slide using a glycerol solution and observed under an optical microscope.

6.3 RESULTS

6.3.1 *In vivo* degradation of the magnesium-zinc-zirconium-strontium (Mg-Zn-Zr-Sr) alloy pins

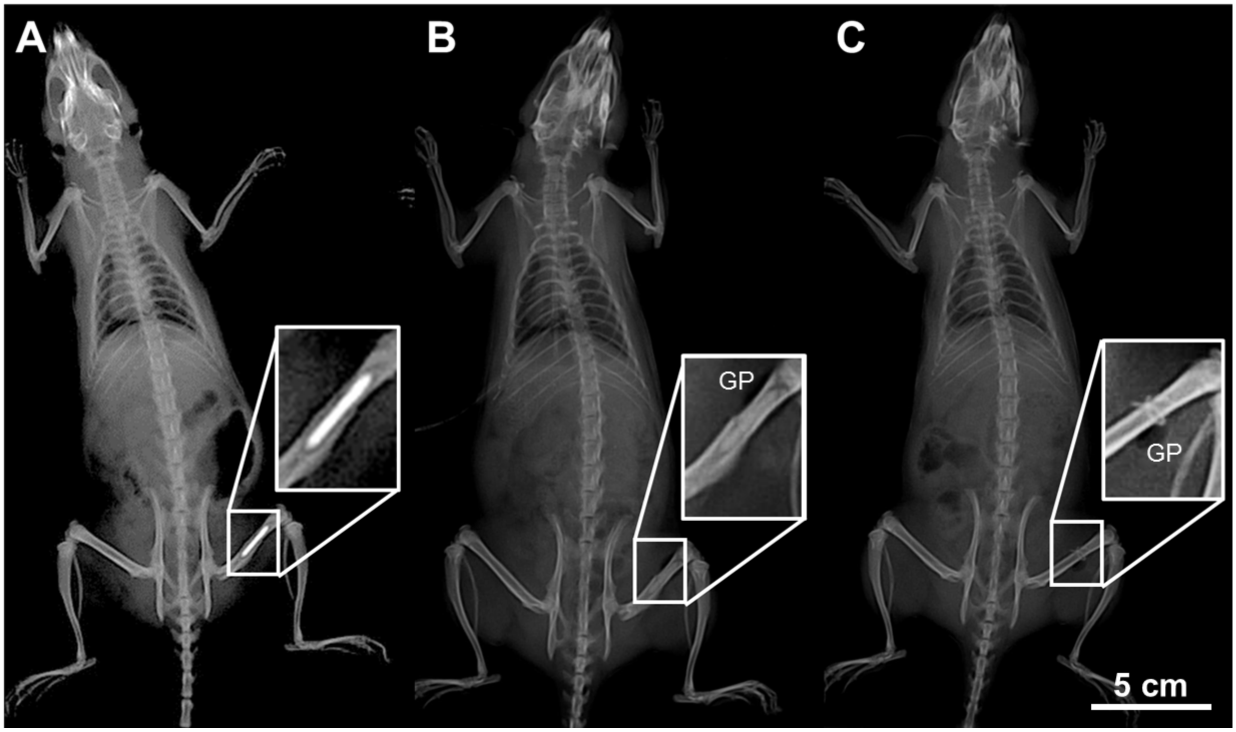

Figure 6.2 X-ray radiograph image of (a) Ti pin, (b) Mg-Zn pin, and (c) Mg-Zn cuff pin implanted rats after 1 week (GP: gas pocket).

Figure 6.2 exhibits representative x-ray radiograph images of Ti and Mg-Zn pin implanted rats after 1 week of osteotomy surgery. The images were used to determine the time point for euthanizing each animal based on the quality of fractured femur fixation. In the x-ray image, some visible hydrogen gas evolution was observed around the Mg-Zn implants as shown in Figure 6.2b and 6.2c. Rats implanted with both Ti and Mg-Zn pins exhibited normal movement and ambulatory behavior.

Harvested femurs exhibited normal fracture healing response with intramedullary pins. Callus formation was observed around the wound. Callus formed on the femurs with both Ti and Mg-Zn pins exhibited no visible difference. However, the callus formed on the femurs after 8 and 12 weeks of implantation was more hardened compared to the callus after 2 weeks of implantation. The fracture femurs with Mg-Zn pins was not aligned as straight as the femurs with Ti pins.

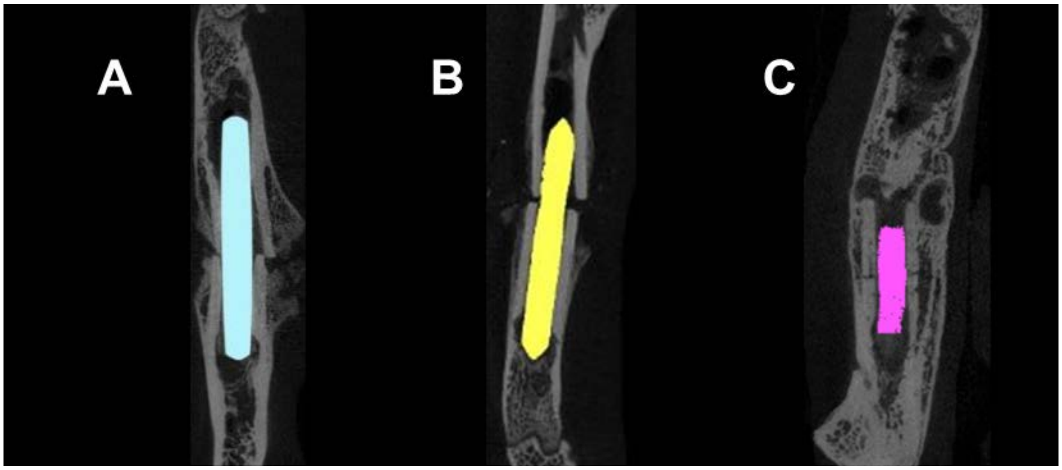

Figure 6.3 Micro CT analysis image of (a) Ti pin at 14 weeks and Mg pins at (b) 2 weeks, and (c) 14 weeks.

Figure 6.3 shows the representative micro-computed tomography (micro-CT) images of rat femurs with Ti or-Mg-Zn pins after plastic embedding. Femur with a broken Mg-Zn pin resulted in a misalignment of fractured bones. At 2 weeks, 3 out of 5 Mg-Zn pins were fractured into 2 pieces. Ti pins on the other hand, exhibited no fracture or damage due to the load. Mal-union of the femurs with broken Mg-Zn pins can lead to a significant difference in the fracture healing. However, the micro-Ct images for 14 months for both Ti and Mg-Zn pins implanted shown in Figure 6.3 indicated that the fracture healing process was not completed. More hydrogen gas bubbles were evolved around Mg-Zn pins following 2 weeks of implantation not distinguishable in micro CT but was noticeable in the histology as discussed later. After 14 weeks, the gas bubbles were however, not distinguishable in the micro-CT images.

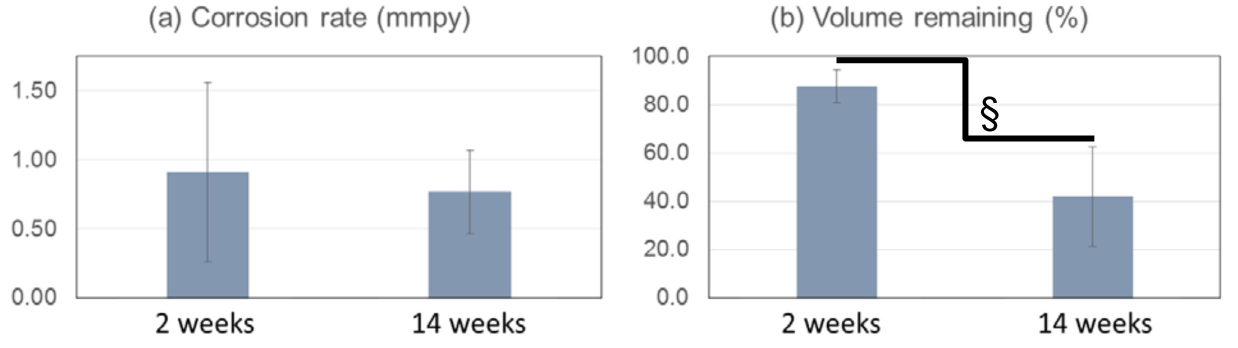

Figure 6.4 (a) Corrosion rate and (b) volume remaining of Mg-Zn pins implanted after 2 and 14 weeks (n=5, §$p<0.05$ denotes a significant difference between groups).

The remaining volume of Mg-Zn pins in the intramedullary region was analyzed from the micro-CT images (see Figure 6.4b). The remaining volume of Mg-Zn pins after 2 weeks of implantation was 87.7%. After 14 weeks, the remaining volume was significantly decreased to 42.0%. Corrosion rates of Mg-Zn pins were calculated from the volume loss and original surface area as shown in Figure 6.4a. Mg-Zn pins for 2 weeks of implantation exhibited the corrosion rate of 0.91±0.65 mmpy. The corrosion rate at 2 weeks was anticipated to be higher than the other time points since the Mg-Zn pins was exposed to the largest mechanical stress at the 2 week time point. The Mg-Zn pins for 14 weeks of implantation continued to degrade with larger surface area being exposed which resulted in the corrosion rate of 0.77±0.30 mmpy.

6.3.2 Blood test results

Table 6.2 summarizes blood test results of rats before and after osteotomy surgeries for 2 and 14 weeks of Ti and Mg-Zn pins/cuffs implantation. Red blood cell, hemoglobin, and platelet count exhibited no significant difference in the groups for the different implants and the different time durations. White blood cell count after 2 weeks of Ti pin implantation was significantly higher compared to the Mg-Zn group. However, it still remained within the reference range.

Biochemical analysis results rats before and after osteotomy surgeries for 2 and 14 weeks of Ti and Mg-Zn pins/cuffs implantation are listed in Table 6.3. ALT after 2 weeks of implantation for both Ti and Mg-Zn pins exhibited significantly higher level compared to the implants for the other time points. However, these ALT values still remain within the reference range. For ALP, TBIL, TP, ALB, UA, CR, and GLB, all groups exhibited no significant difference between implants and implantation duration suggesting no signs of liver or kidney damage due to degradation of Mg-Zn pins.

Calcium, sodium, chloride, phosphorous, and magnesium ion levels in the serum before and after implantation are listed in Table 6.4. No significant difference in these ion levels were found between implants or implantation duration. All values remained within the reference range suggesting that there were no changes to the systemic ion concentration due to implantation and the consequent degradation of the Mg-Zn-Zr-Sr alloy pins.

Table 6.2 Hematologic analysis results from blood panel test after Ti pin (2 and 14 weeks), Mg-Zn pin (2 and 14 weeks), and Mg-Zn cuff (2 weeks) implantations.

Name	Implantation time	Red Blood Cell Count	Hemoglobin	Platelet Count	White Blood Cell Count
Units		10^6/uL	g/dL	10^3/uL	10^3/uL
Ref. ranges		(7.00-9.00)	(13.7-16.8)	(680-1280)	(1.1-7.5)
Pre-operation		7.4	14.1	618.3	6.8
Ti pin	2 weeks	7.8	14.9	656.0	9.0
Mg-Zn pin	2 weeks	7.4	14.1	547.0	3.7
Ti pin	14 weeks	7.5	14.0	563.0	5.9
Mg-Zn pin	14 weeks	7.3	13.7	598.0	4.5
Ti cuff	14 weeks	7.6	13.8	637.0	5.8
Mg-Zn cuff	14 weeks	7.2	13.4	537.0	6.2

Table 6.3 Biochemical analysis on blood serum after Ti pin (2 and 14 weeks), Mg-Zn pin (2 and 14 weeks), and Mg-Zn cuff (2 weeks) implantations.

Name	Implantation time	Glucose	ALT (GPT)	ALP	Total Bilirubin	Total Protein	Albumin	Urea N	Creatinine	Globulin	A/G Ratio
Units		mg/dL	U/L	U/L	mg/dL	g/dL	g/dL	mg/dL	mg/dL	g/Dl	
Ref. ranges		(70-308)	(59-166)	(232-632)	(0.0-0.1)	(5.8-7.1)	(3.2-3.7)	(13-19)	(0.3-0.5)	(2.6-3.5)	
Unoperated		181.2	55.8	175.2	0.17	5.7	3.3	20.7	0.37	2.4	1.4
Ti pin	2 weeks	322.0	132.6	151.2	0.14	6.2	3.3	17.6	0.42	2.9	1.1
Mg-Zn pin	2 weeks	293.0	123.0	140.0	0.18	6.7	3.5	20.5	0.53	3.2	1.1
Ti pin	14 weeks	229.5	56.8	187.0	0.18	6.3	3.7	21.8	0.52	2.6	1.4
Mg-Zn pin	14 weeks	124.2	57.8	181.8	0.20	6.3	3.6	22.2	0.56	2.7	1.3
Ti cuff	14 weeks	154.4	50.2	163.6	0.18	6.2	3.6	19.6	0.52	2.6	1.4
Mg-Zn cuff	14 weeks	203.0	59.4	190.4	0.16	6.5	3.8	23.2	0.52	2.7	1.4

Table 6.4 Electrolyte levels of blood serum after Ti pin (2 and 14 weeks), Mg-Zn pin (2 and 14 weeks), and Mg-Zn cuff (2 weeks) implantations.

Name	Implantation time	Calcium	Sodium	Chloride	Phosphorous	Magnesium
Units		mg/dL	mmol/L	mmol/L	mg/dL	mg/dL
Ref. ranges		(9.5-13.9)	(146-151)	(98-104)	(5.6-16.8)	(3.8-5.5)
Unoperated		9.8	138.2	100.5	5.5	2.0
Ti pin	2 weeks	11.5	143.8	100.2	9.7	3.4
Mg-Zn pin	2 weeks	12.1	141.3	100.3	12.0	3.7
Ti pin	14 weeks	12.2	145.2	99.0	9.6	3.6
Mg-Zn pin	14 weeks	11.3	146.8	100.6	9.4	3.3
Ti cuff	14 weeks	11.6	147.6	99.6	9.2	3.3
Mg-Zn cuff	14 weeks	12.2	148.0	99.8	8.7	3.5

6.3.3 ICP analysis on liver and kidney

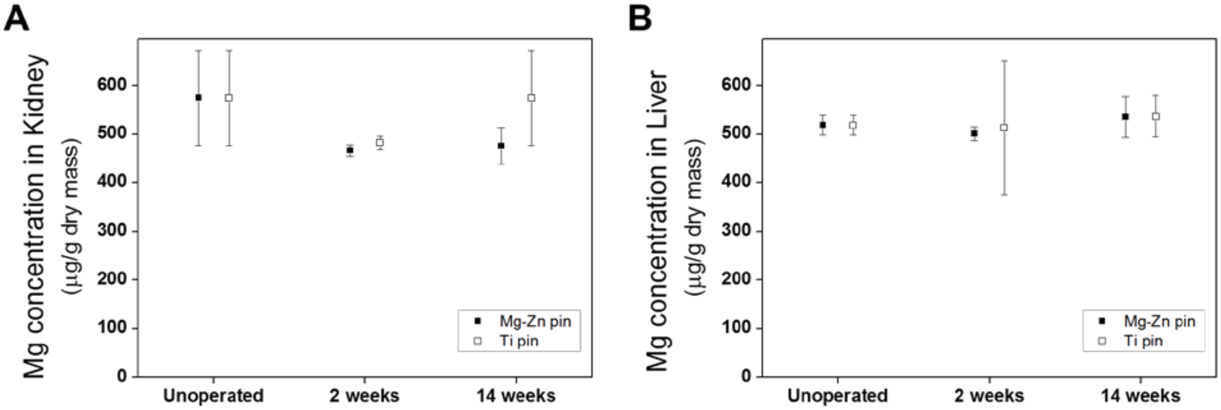

Figure 6.5 Mg concentration of (a) liver and (b) kidney using ICP analysis (n=5).

ICP analysis of the liver or kidney was performed to examine any form of Mg accumulation in the organs after implantation of the Mg-Zn alloy pins and cuffs in comparison to the Ti control. In Figure 6.5a, Mg concentration determined in the kidney harvested from the experimental groups containing Mg-Zn implants exhibited no accumulation of Mg when compared to the concentration of kidney from the non-operated groups. Figure 6.5b shows Mg concentration observed in the liver tissue from the non-operated controls to be in the range of 521 μg of Mg per gram of dried tissue. Regardless of implantation time, Mg-Zn alloy groups implanted with pin did not show any significant difference with the control level in Mg concentration of liver samples. The observation was consistent with blood test results indicating that implantation of the Mg-Zn alloy pins and cuffs in the rate femoral model outlined above exhibited no systemic toxicity.

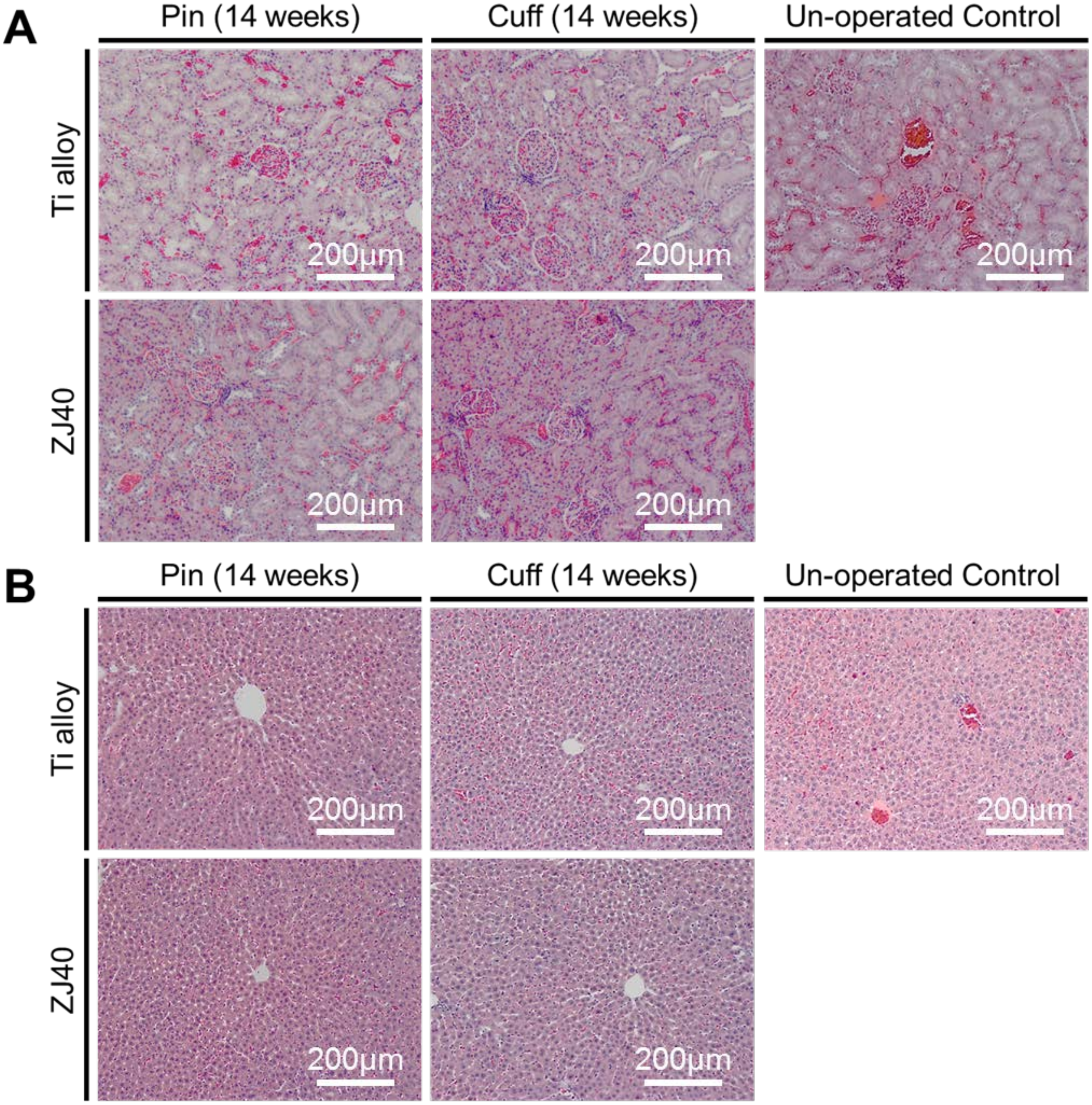

Figure 6.6 Hematoxylin and eosin staining of harvested (a) liver and (b) kidney**.**

6.3.4 H&E staining of liver and kidney

Hematoxylin and eosin staining of liver and kidney tissue sections were performed to visualize any histological differences in tissue morphology due to Ti and Mg-Zn pins implantation. Liver sections of both Ti and Mg-Zn groups after 2 and 14 weeks of implantation shown in Figure 6.6 exhibited a normal distribution of hepatocytes with clearly visible nuclei and central vein. In the kidney histology, no visible difference in glomeruli morphology, Bowman's space, capillaries, and convoluted tubules was observed between Ti control and Mg-Zn groups following 14 weeks of implantation. Histological morphology of liver and kidney tissues of all experimental groups displayed similar morphology as the non-operated control, and no difference was observed in between the groups or at different time points although data is not shown. In addition to ICP and blood test results, the H&E staining confirmed no damage to vital kidney and liver organs due to degradation following implantation of the biodegradable Mg-Zn pins. Although the H&E staining cannot be used to determine any accumulation of Mg, the fact that the histology shows normal and functional tissue serves to indicate that it is likely that there is no accumulation related damage of the kidney and liver tissue and it is possible that with time, there will be certainly removal of Mg following the normal excretory process prevalent in the body. More advanced techniques will however be needed to ascertain the definitive accumulation of Mg, Zn, Zr, and Sr present in the alloy pins that were implanted.

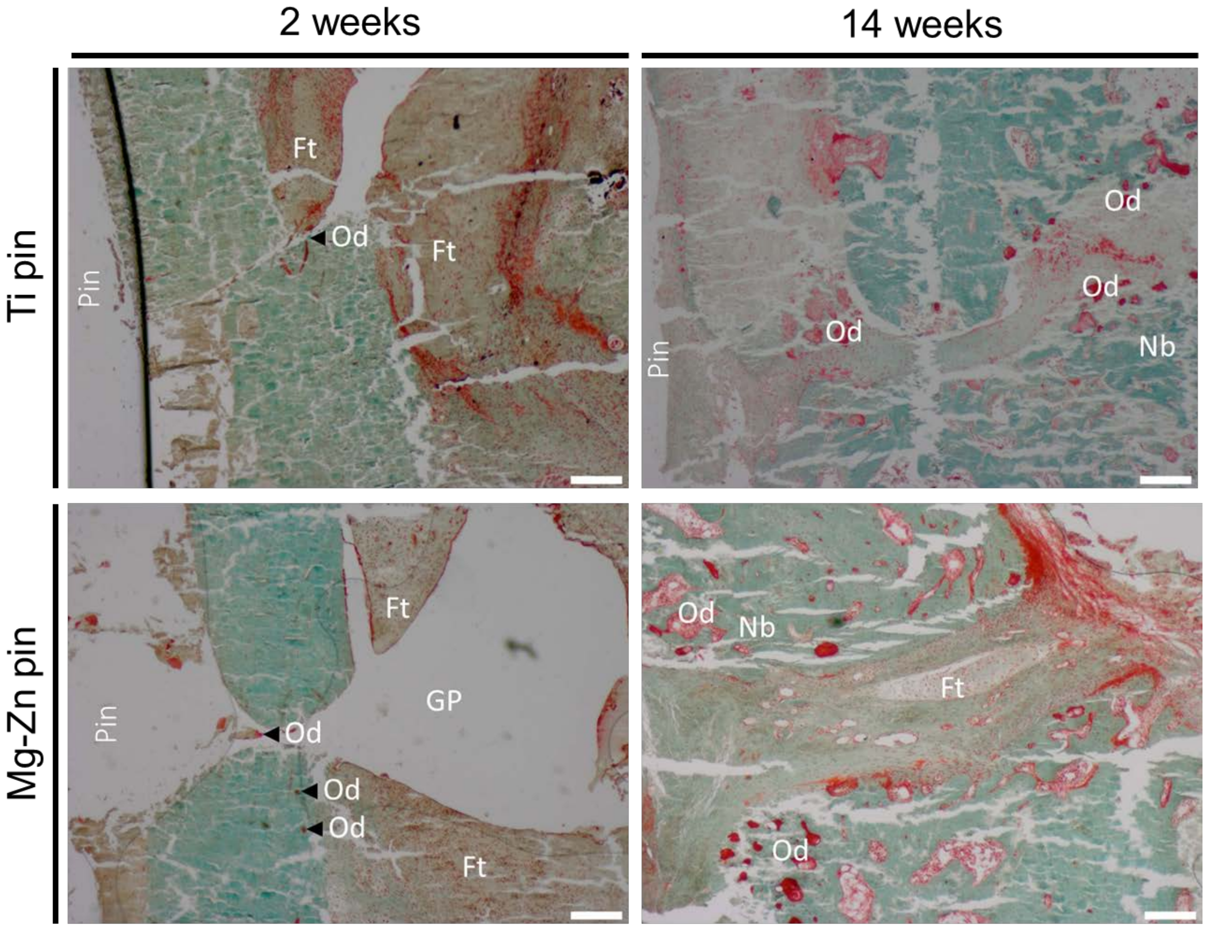

Figure 6.7 Goldner's Masson Trichrome staining of rat femurs after implantation of Ti and Mg-Zn pins for 2 and 14 weeks (Ft: Fibrous tissue; Od: Osteoid; Nb: New bone; GP: Gas pocket; Scale bar = 200 µm).

6.3.5 Bone tissue histology

Goldner’s Masson Trichrome staining of rat femoral sections after plastic embedding revealed a typical fracture healing response as shown in Figure 6.7. After 2 weeks of implantation, the femurs with Ti and Mg-Zn alloy pins exhibited endochondral bone development and fibrous tissue formation around the fracture. Bone tissue section of the femur with Mg-Zn alloy pins after 2 week of implantation exhibited a gas pocket due to the degradation of Mg-Zn pins. After 14 weeks of implantation however, femurs with both Ti and Mg-Zn alloy pins exhibited bone remodeling and intramembraneous bone formation. In addition, the gas pocket of femurs with Mg-Zn pins was filled with fibrous tissues. In any event, fracture repair of either Ti or Mg-Zn groups was not completed after 14 weeks of implantation.

6.4 DISCUSSION

Biodegradable Mg alloys have gained considerable attention as discussed earlier for its potential to provide comparable or even improved benefits in fracture repair and for bone fixation compared to biodegradable polymer and permanent bioinert metallic devices. Mg is characterized by mechanical properties being matched to natural human bone. Hence alloys are designed to exhibit mechanical properties with better match to natural bone while exhibiting the desired timely corrosion rates with more biocompatible degradation products as compared to biodegradable polymers that tend to provide acidic by-products while also additionally lacking the desired osteogenic potential to function as an acceptable bone scaffold system. The rapid corrosion of biodegradable Mg alloys can cause hydrogen gas evolution and immature mechanical failure warranting the need for improved alloy design and other surface engineered strategies to control the corrosion rates while preserving the mechanical strenghths. Hence, *in vivo* degradation and toxicity of Mg alloys have been widely studied to demonstrate the much desired biosafety and efficacy as candidate biomaterials for implantable devices. Orthopedic devices are often used in load-bearing conditions and metals often tend to corrode more rapidly when stress is applied via the well-known stress corrosion mechanisms. This is a common fixture and often the mode of much observed problems to date in permanent metal devices which also reveal stress induced corrosion, wear, and debris formation.

The current study is aimed to test degradation properties and biocompatibility of Mg-Zn-Sr-Zr alloys under load-bearing condition. Mg alloys are not intended for use as a femoral rod since they are known to degrade in the body. However, a femoral fracture model using intramedullary pins can exert a significant load on the implant material to cause a stress-induced corrosion for examining relevant physiological response such as bone healing, inflammatory response, and systemic toxicity thus serving as an ideal model system to study healing under the presence of stress. Thus using this fracture model, a group of rats were implanted with femoral cuffs for 14 weeks to compare any difference in systemic toxicity due to implantation site.

In vivo degradation of Mg-Zn pins and cuffs was assessed using x-ray radiographs after 1 week of surgery. It is widely accepted that hydrogen gas bubble evolves in the earlier time points and tend to kinetically slowdown in 2~3 weeks (127). Mg alloys implanted in bone without a significant load also are reported to show slow degradation exhibiting no gas bubbles while Mg alloys in subcutaneous region exhibit significant gas bubbles due to the surrounding vascularization and presence of blood flow (153). Both Mg-Zn alloy pins and cuffs were observed to be surrounded with hydrogen gas in the surrounding tissue. Bone histology results were also consistent with the x-ray images showing gas pockets near the fracture site in the image following 2 weeks of Mg-Zn pin implantation (see Figure 6.2). Both x-ray radiograph and bone histology results indicate that the corrosion of Mg-Zn alloy implants in rat femurs were rapid enough to create gas bubbles. However, the gas bubbles appear to be eliminated after 14 weeks of implantation as shown in the bone tissue histology image.

Computed tomography was used to perform fracture healing and determine quantitatively the degradation rate. Failure of the Mg-Zn alloy pins were observed in fractured femurs after 2 weeks of implantation. After 14 weeks however, callus formation and bone remodeling around the fracture site were exhibited. Femurs with both Ti and Mg-Zn alloy pins revealed similar bone repair response. Rat femoral fracture model typically require up to 5 months to complete the fracture healing process (154). 3 out 5 rat femurs with implantation of Mg-Zn pins for 14 weeks were observed with a malunion that might have resulted from the breakage of the pins due to the excessive stress experienced by the animals following immediate surgery and allowing the rats to ambulate subjecting the area to significant load serving as a classic stress corrosion fracture model. Despite this, it should be noted that the implants showed acceptable and favorable bone healing response as indicated by the other femurs in union exhibiting better bone healing with more bone remodeling and united callus formation over the cortical bones. This result serves to demonstrate the potential safety and efficacy of the alloy system for potential orthopedic applications. Accelerated corrosion rates of Mg-Zn alloy pins obviously as explained earlier result from stress corrosion. Mg-Zn alloy alloys are in fact, known to degrade with higher corrosion rates compared to Mg alloys under non-load bearing condition according to the literature (155). Based on the analysis reported here and discussed above, rapid corrosion of Mg-Zn alloy pins under load-bearing condition did not significantly affect the fracture repair in terms of adverse local tissue response. However, mechanical strength of Mg alloys decreases with corrosion (156, 157) and the Mg-Zn alloy pins therefore underwent failure which could have affected the fracture healing outcome negatively although not necessarily serving to negate the potential applicability of the system for orthopedic application with further optimization of the alloy and the processing parameters.

Systemic toxicity of rats with Mg-Zn alloy pins were assessed after 2 and 14 weeks of implantation when 15% and 55% of total volume of the implants were resorbed (see Figure 6.4). In addition, a group of the Mg-Zn alloy cuffs were assessed to evaluate the toxicity of Mg-Zn alloy in contact with both bone and muscle. After 14 weeks, the cuffs were fully resorbed. Blood and serum examination was focused on hematologic and biochemical analysis to detect any disruption in blood, liver and kidney tissue state. Blood cell count and biochemical parameters were maintained within the reference ranges and there were no significant difference among Ti, Mg-Zn, and control groups. Recent publications also reported no significant abnormality in blood test results following *in vivo* degradation of Mg alloys (153, 158). BUN, CR, and UA from serum analysis also indicates no significant changes in the renal function. No accumulation of Mg in liver and kidney were also found following the inductively couple plasma analysis conducted on the digested tissues. Histology of liver and kidney also displayed histomorphology pattern mirroring healthy tissue. Excess Mg in body is known to excrete in urine after renal filtration (159). Bodily Mg concentration beyond the tolerance limit can however, cause renal failure (122). Based on the published literature to date, the toxicity test methods described herein are effective since high Mg dose in body does not cause local accumulation in a specific organ other than liver or kidney. In order to track localized Mg accumulation in other organs, biosensors or quantum dot staining methods can be considered to locate the exact location as well as the amount of accumulation. Overall, the observations from blood test, Mg concentration, and histology results consistently indicate that the Mg-Zn alloy implant considered here and their degradation products are indeed biocompatible for potential use as possible orthopedic implants under load-bearing conditions.

6.5 CONCLUSIONS

Mg-Zn alloy, in comparison to Ti alloy as a control, was examined as femoral pins under load-bearing condition using a rat femoral fracture model. Accelerated degradation of the Mg-Zn alloy pins occurred due to stress corrosion. Hence, hydrogen gas pockets were observed initially and some pins tend to lose their mechanical stability in the early stages of 2 week implantation. However, normal bone healing was displayed following bone histological analysis. No fibrous capsule formation or adverse immune response was observed in local tissues around the Mg-Zn alloy implant devices as well. Furthermore, degradation of Mg-Zn implants caused no significant changes in hematologic or biochemical markers assessed using blood panel tests. Magnesium concentration of liver and kidney demonstrated no accumulation of Mg in these organs as well following elemental analysis of the tissue for the specific alloying elements. Histology of liver and kidney also displayed no organ damages due to the Mg-Zn alloy implants. Overall, the results suggest that Mg-Zn alloy demonstrates favorable biocompatibility under load-bearing conditions. Further improvement of the alloy design and experimentation is required to improve the alloy mechanical stability particularly, during degradation of the hardware devices to achieve even more desirable bone healing and fracture repair.

7.0 GENERAL CONCLUSIONS AND FUTURE WORK

The four chapters discussed herein have shown by virtue of the four relevant specific aims the efficacy of two primary Mg based alloys, Mg-Zn-Zr and Mg-Zn-Sr-Zr alloys for potential orthopedic applications. Accordingly, Mg-Zn-Zr alloy was initially studied to explore the potential of its use as a biodegradable metal for orthopedic applications. Both as-cast and solution treated Mg-Zn-Zr was synthesized by melting in an electric resistant furnace, casting in a mild steel mold, and post-processing of heat treatment in a box furnace. X-ray diffraction patterns of as-cast and solution-treated Mg-Zn-Zr exhibited α-Mg phase without any distinct intermetallic peaks. However, back-scattered electron microscopy revealed Mg/Zn intermetallic precipitates along the grain boundaries. Solution treatment of Mg-Zn-Zr was performed to cause phase transformation of these precipitates to reduce the galvanic corrosion between Mg-Zn precipitates and α-Mg matrices. Mg-Zn precipitates were successfully transformed to Mg-Zn-Zr phase mixture which is more close to the nominal composition of the alloy. However, no significant improvement in the corrosion potential or current density was exhibited in the potentiodynamic polarization measurement.

As-cast and solution-treated Mg-Zn-Zr were then subjected to in vitro assessments in terms of corrosion resistance, mechanical properties, and cytocompatibility. Corrosion of Mg-Zn-Zr was improved after solution treatment due to the phase transformation of precipitates. Immersion corrosion rates of solution-treated Mg-Zn-Zr was observed to be lower than that of as-cast Mg-Zn-Zr. Tensile and compressive strengths of both as-cast and solution-treated Mg-Zn-Zr were observed to be higher than pure Mg but not comparable to commercial as-drawn AZ31. Cytocompatibility of Mg-

Zn-Zr alloys was assessed using ISO 10993 standards with modifications for biodegradable metals. Good cell viability of MC3T3 murine pre-osteoblast cells was exhibited by both as-cast and solution-treated Mg-Zn-Zr alloys. Promising preliminary *in vivo* degradation and tissues compatibility results were also exhibited by these alloys when as-cast Mg-Zn-Zr pellets were subcutaneously implanted in nude mice models.

Addition of Sr and Ce as micro alloying element to Mg-Zn-Zr alloys were investigated to further improve corrosion resistance by reducing Zn-rich intermetallic phase in grain boundary precipitates. Microstructure analysis using back-scattered electron microscopy clearly exhibited the phase transformation of precipitates. Unfortunately, an introduction of micro alloying element created more precipitates although only 0.25% and 1% addition were introduced into the Mg-Zn-Zr system due to the inherent low solubility of Sr and Ce in Mg. Ce was more prone to form precipitates along the grain boundaries compared to Sr due to the higher melting point of Ce required for homogenization of alloy melts before casting and extrusion. Overall, the corrosion resistance of Mg-Zn-0.25Sr-Zr, Mg-Zn-1Sr-Zr and Mg-Zn-0.25Ce-Zr did not exhibit a significant difference compared to Mg-Zn-Zr. However, Mg-Zn-1Ce-Zr exhibited higher corrosion rate after immersed in Hank’s buffered solution for 35 days. In tensile testing, as-extruded Mg-Zn-Zr, Mg-Zn-Sr-Zr, and Mg-Zn-Ce-Zr outperformed commercial AZ31. Ultimate tensile strength increased with Ce addition since more precipitates contributed to dislocation impediment leading to increased strengths. Mg-Zn alloys also exhibited good cytocompatibility with MC3T3. Tolerance of Mg, Zn, Sr, and Ce ion levels were studied using MC3T3 and low Zn tolerance up to 0.1 mM was observed. Osteogenic differentiation ability of Mg, Sr, and Ce were further studied with human mesenchymal stem cells. ALP activity and ALPL gene expression did not exhibit any significant change compared to the differentiation media control. However, OPN gene expression exhibited some improvements with addition of Mg, Sr, and Ce ions in the differentiation media.

In order to demonstrate biocompatibility of Mg-Zn alloys, Mg-Zn-0.25Sr-Zr (Mg-Zn) alloy was selected for rat femoral fracture model intended to create stress corrosion environment. Intramedullary pins of Mg-Zn and Ti alloy control were implanted after osteotomy to assess the degradation and toxicity under load-bearing condition. Accelerated corrosion of Mg-Zn alloy due to stress corrosion was anticipated due to the model selected to test the toxicity of Mg-Zn alloy and its degradation products in an extreme stress corrosion environment. X-ray images after 1 week of Mg-Zn pin implantation exhibited hydrogen gas pockets around the implantation site due to rapid corrosion. Micro computed tomography analysis exhibited higher corrosion rate of Mg-Zn pin compared to in vitro corrosion rate of the Mg-Zn alloy. However, bone histology and CT analysis after 14 weeks of implantation revealed that the gas pockets around Mg-Zn pins were filled with fibrous tissue and normal fracture healing was observed compared to Ti alloy control. Cuffs of Mg-Zn-0.25Sr-Zr and Ti alloy were implanted on rat femurs to investigate any difference in local tissues response or systemic toxicity when these implants are in contact with both bone and soft tissue. In both scenarios, no adverse toxic response was observed in blood panel tests as well as hematoxylin & Eosin staining of liver and kidney after 2 and 14 weeks of Mg-Zn and Ti device implantation. No accumulation of Mg in liver and kidney was confirmed by using inductively coupled plasma analysis on digested organs. Thus by virtue of all the four specific aims, the study essentially shows that the Mg-Zn alloy system is indeed quite promising and when effectively processed could exhibit improved corrosion, tailored mechanical strengths and also likely expected osteogenic potential with the addition of controlled amounts of Sr and Ce.

Based on the studies conducted in this thesis, it can be construed that the Mg-Zn alloy has been developed quite effectively and the desired biosafety of Mg-Zn alloys has also been clearly demonstrated under both *in vitro* and *in vivo* conditions. Despite the promising results, further development is clearly warranted to evaluate the efficacy of a specific Mg-Zn device for technology transition and regulatory approval. More specific animal studies with appropriate models selected and suitably designed with proper processing conditions are needed to clearly understand the correlation between the expected and desired biomechanical tissue and materials response matching the ultimate healed tissue and the desired degradation. These optimal design considerations can be brought to fruition by matching theoretical first principles density functional theory studies implemented along with finite elements and continuum mechanics modeling studies combined with robotic assisted evaluation. Such modeling studies conducted in combination with proper processing conditions of the alloys will help in clearly delivering theoretically predicted alloying elements combined with simulation results to experimentally generate as predicted alloys with the expected physical, chemical and biological response. Also, various coating techniques such as micro artic oxidation (MAO), layer by layer (LbL) polyelectrolyte coatings, use of synthetic and natural polymers, and a variety of metallic coatings can explored as coating strategies that can be applied to the biodegradable Mg-Zn devices. These strategies can help to prevent rapid corrosion and premature mechanical failure while also augmenting delivery of growth factors and signaling molecules to generate a ‘smart’ scaffold and implant system serving as a scaffold as well as drug and biological molecule delivery system. These studies can be hopefully conducted in the near future.

APPENDIX A

BIODEGRADABLE IRON-MANGANESE-CALCIUM/MAGNESIUM ALLOY DEVELOPMENT FOR BINDER-JETTING 3D PRINTING OF PATIENT-SPECIFIC CRANIO-MAXILLOFACIAL SCAFFOLDS

A.1 INTRODUCTION

Fixation screws, plates, and meshes have been widely used to reconstruct skull or facial fractures (160). In most cases, these treatments result in a successful reunion of the remaining bone fragments. However, the treatments tend to fall short when there are civilians who have succumbed to severe automotive accidents, traumatic battlefield injuries, and bone cancer conditions. Injuries such as these often involve a critical-sized bone defect (CSBD) that has a large region or gap of missing bone that the body's own homeostatic healing prowess alone is incapable of providing the healing. As a result, the defect needs to be either filled with a synthetic bond void filler or a synthetic or naturally derived bone graft taken from the patient alone or from another donor, all of the approaches suffering from limitations (161, 162). Newer approaches particularly, based on additive manufacturing technologies appear very promising. The technology is particularly novel since it involves matching the geometry of the bone graft to that of the affected area which is indeed necessary in order to obtain satisfactory results.

Intraoperative adjustments have been widely used to prepare an autograft or allograft for reconstructive surgery (11). These surgical procedures although innovative on its own accord boasting of much desirable success are very much depended on existing materials which do not really match or fit the patient's specific bone or defect configuration, shape or size. As a result, many times complicated machining methods are needed to fit the defect size or in many cases, the materials or implants that are available in certain specific sizes would need to be force fit into the defect site. As a result, additional materials may be needed to put the device in place or in some cases, the implant would need to be force fit into place. In either case, the degree to which the geometry is accurately replicated is referred to as the geometrical fit of the device. Efforts have been made to improve the geometrical fit of the device by utilizing CAD/CAM technologies and stereolithography techniques (163, 164). Recently, 3-dimensional printing (3DP) has been explored as a fabrication method for patient-specific devices utilizing existing biomaterials such as PEEK (165), titanium (166), Co-Cr (167), and hydroxyapatite (168) which have been discussed in Chapter 1 as well. These synthetic scaffolds have been widely used as they eliminate the need for a donor site; thus reducing the risk of complications and lowering the chance of patient infection or device rejection compared to traditional bone grafting (169). However, conventional synthetic biomaterials have some limitations. Ceramic or polymeric scaffolds for example, exhibit insufficient mechanical properties or tend to undergo slow *in vivo* degradation (170). Non-degradable metallic biomaterials such as Ti6V4Al, Co-Cr, and stainless steel on the other hand, as outlined in Chapter 1 possess the desired sufficient strength, but often cause stress shielding and undergo corrosion, wear, and debris formation when used for long-term (171, 172). As a result, other complications eventually surface such as metallosis, as well as delayed type hypersensitivity which can lead to rejection of the implant causing the need to remove the implant or other related complications which can have untoward irreversible complications and risks that can be harmful to the patient.

Biodegradable metals such as Mg-based or Fe-based alloys have gained significant attention in recent years due to their degradation characteristics and higher mechanical strength compared to biodegradable polymers and ceramics (38) while also providing the flexibility to match the mechanical properties to natural human bone. 3D printing of biodegradable metals has the potential to deliver patient-specific biodegradable scaffolds to individuals with traumatic injuries as well as providing customized patient specific geometries eliminating the problems of machining and other mismatch of the hardware to the patient desired geometry and configuration of the defect. Further, depending on the required properties of the scaffold at different implantation sites, a porous structure of the scaffold can be designed and fabricated by 3-D printing. At the same time, the design can engineered to specifically load any bone grafting materials, engineered tissues, or drugs. Hence, bone regeneration is often desired to replace the biodegradable scaffold with newly mineralized tissue obviating the need for removal of the implanted hardware at any later point in time putting the patient at risk. Generating and fabricating such degradable materials that also have osteogenic potential by 3-D printing to manufacture customized patient specific implants would offer a novel pathway to bone tissue engineering and regenerative medicine of mineralized tissue.

In this regards, Mg-based alloys have been widely studied for orthopedic and cardiovascular applications. Improving the purity of cast ingots and refining the grain sizes of the alloy as discussed in the earlier Chapters allows for controlled corrosion of these Mg-based alloys (173). Homogeneous ingots with low levels of impurities have exhibited gradual degradation rates. Additionally, the use of post-processing methods such as hot extrusion, rolling, and equal channel angular pressing (ECAP) have been proven to improve corrosion resistance and mechanical strength by refining the microstructure (79, 80). Compression screws made of the magnesium-based alloy WE43 have obtained the CE conformity marking in Europe, and 26 patients have already been recruited and have participated in a clinical trial (58). Human clinical trial of cardiovascular stents is also ongoing in Europe. The potential synergy between biodegradable metals and 3D printing has also initiated much needed research in selective laser melting (SLM) to achieve 3D printing of magnesium powder (174). The high vapor pressure and low melting points of magnesium tend to be major barriers to fabrication of quality parts of accurate dimensions, although lasers can break the oxide layer of magnesium particles effectively leading to fusion and sintering. Indeed, post-processing methods such as hot extrusion, ECAP, or rolling are not applicable for 3D-printed magnesium parts with complex shapes, whereas the microstructure refinement is a key to overcoming the rapid pitting corrosion of magnesium.

Fe-based alloys, on the other hand, tend to degrade too slowly, and thus, research had been focused on increasing the degradation rates. An iron-manganese binary composition was introduced as a biodegradable Fe-based alloy with enhanced corrosion rate and reduced ferromagnetic properties (175). Various alterations of the Fe-Mn system have been studied. Addition of 6 wt. % Si in Fe-30 wt. % Mn induced a shape memory effect (176). Addition of 1 wt.% of Pd to Fe-10 wt.% Mn resulted in a 10-fold faster corrosion compared to low carbon steel (177). Fe-Pd and Fe-Pt have also exhibited faster degradation rates compared to pure iron, and also exhibited minimal cytotoxicity in an indirect MTT cytocompatibility test with L-929 and ECV304 cells after 4 days of culture (178). Fe-W and Fe-CNT composites have also exhibited no toxicity with L929 and ECV304 cells as well as good hemocompatibility (179). Fe-Mn-C (-Pd) alloy was developed and evaluated in both *in vitro* and *in vivo* conditions (180, 181). Unlike *in vitro* degradation, *in vivo* degradation of Fe-Mn-C (-Pd) however resulted in little degradation although no sign of inflammation or local toxicity was reported. Recent literature reports thus suggest that higher degradation rate still remains a major challenge and a primary limitation preventing the development of biodegradable Fe alloys for medical device applications.

Researchers in the current group studied the feasibility of binder-jet 3D printing of a Fe-30 wt.% Mn binary mixture to fabricate biodegradable scaffolds (182). Binder-jet 3D printing of the Fe-Mn mixture exhibited micropores with favorable effects on in vitro degradation and cell attachment. A porous structure with an open porosity of 36% was obtained after sintering of 3D-printed (3DP) specimens. 3DP Fe-Mn specimens exhibited a significantly higher corrosion rate when compared to pure Fe using potentiodynamic polarization tests due to the perceived porosity induced by 3DP. Cell infiltration was also observed in the open pores of the 3DP Fe-Mn specimens during cytocompatibility tests using the MC3T3-E1 pre-osteoblast cell line.

In the present study, the research was focused on developing Fe – (35 - y) wt.% Mn – y wt.% X (X = Ca, Mg, and y = 0, 1, 2) employing a CALPHAD theoretical model to predict the alloy composition with enhanced degradation properties. In order to test the hypothesis, Fe-Mn-X alloy powders were synthesized using high energy mechanical alloying (HEMA), and assessed in terms of degradation properties and cytocompability. Furthermore, Fe–35 wt.% Mn and Fe–34 wt.% Mn–1 wt.% Ca were selected for 3D printing study based on their cytocompatibility and degradation characteristics. The 3DP specimens of Fe–35 wt.% Mn and Fe–34 wt.% Mn–1 wt.% Ca alloys were evaluated to confirm if the enhanced degradation and cytocompatibility characteristics observed following milling and conventional sintering are indeed maintained after the 3D printing approach.

A.2 MATERIALS AND METHODS

A.2.1 Methodology for CALPHAD studies

To evaluate the effect of different alloying elements on the corrosion stability of the alloys a prior study was conducted that focused on evaluating of the thermodynamic driving force of the overall hydrolysis reaction of magnesium and its alloys in pure water (183). Using the Density Functional Theory (DFT) approach, the heats of the aqueous chemical reactions calculated for Mg alloys have been compared with that corresponding to the reaction of pure Mg with water. The heats of reactions are dependent upon the chemical compositions of the alloys, for this study the role of Ca, Zn, Y, Al, and Fe on the aqueous chemical stability and reactivity of these Mg-alloys has been discussed.

The first-principles calculations require substantial computational resources, making their applications to multi-component and multiphase systems a formidable task. In addition, the calculations were carried out at 0 K, a temperature at which the relevant phase stabilities may deviate from those at the body temperature of 310 K.

To overcome difficulties of the first-principles study of the thermodynamic parameters of the hydrolytic reactions the less physically-grounded but yet much more efficient CALPHAD technique (184) could be used. This technique can be used to investigate the thermodynamic stability of various metals and alloys in various aqueous environments. With the help of several well-developed thermodynamic databases, this approach provides the flexibility to investigate the corrosion behavior of alloys with arbitrary compositions in aqueous phases with environmental conditions (temperature and pressure, etc.) matching the authentic human blood media, thus compensating the limitations of the first-principles approaches.

In a previous paper (183), researchers involved in this study suggested focusing on a change in enthalpy δΔHRdop in their actual first-principles calculations in order to assess whether the alloying element retard (δΔHRdop > 0) or promote (δΔHRdop < 0) the corrosion process. Accordingly, in the current study, the same criterion was employed for evaluation of the corrosion stability of Fe–35 wt.% Mn alloys doped with small amounts of Ca and Mg. In essence, the following two aqueous reactions were considered; the Gibbs free energy ΔGR was calculated for each reaction and the difference between them (δΔGR) was plotted as a function of the chemical composition of the materials.

$$\mathrm{Fe(s)} + 2\mathrm{H_2O(l)} \Rightarrow \mathrm{Fe(OH)_2(s)} + \mathrm{H_2(g)} \qquad (1)$$

$$\mathrm{[Fe\text{-}Mn\text{-}Ca/Mg](s)} + 2\mathrm{H_2O(l)} \Rightarrow \mathrm{[Fe\text{-}Mn\text{-}Ca/Mg](OH)_2(s)} + \mathrm{H_2(g)} \qquad (2)$$

Reaction (1) is the hydrolytic reaction for pure Fe in water, while the reaction (2) represents the same process for various considered Fe-based alloys.

In the present study the thermodynamic software Thermo-Calc (185) has been employed to conduct the calculations using SSUB4 database for chemical substances such as oxides, hydroxides and gas phases (186), and TCFE7 for solid Fe-Mn-Ca/Mg alloy phases (72). All the calculations have thus been conducted at temperature T = 370 °C and pressure P = 1 atm.

A.2.2 Powder preparation

Pure iron powder, pure manganese powder, and pure calcium granules were used to synthesize Fe – (1 - y) wt.% Mn – y wt.% X (X= Ca, Mg, and y = 0, 1, 2) alloy powder. Milling balls and pure elemental powder mixtures were weighed at a mass ratio of 10:1 and subjected to high energy mechanical alloying (HEMA). The milling vial was sealed under ultra-high purity (UHP) argon atmosphere within a glove box in order to prevent any oxide formation. A P5 planetary mill (Fritsche, Idar-Oberstein, Germany) was used to perform up to 16 h of dry milling followed by 8 h of wet milling cycles with toluene. The Fe-based alloy powder was collected and sieved using -325 mesh. The alloyed powders were imaged using scanning electron microscopy (SEM; JSM-6610, JEOL, Tokyo, Japan) for particle morphology. Phase analysis was performed using X-ray diffraction employing X'pert Pro system (Philips, Netherlands) with CuKα radiation (λ = 1.5418 Å) and Si-detector (X'celerator) operated at 45 kV and 40 mA.

A.2.3 3D parts fabrication

3D parts were fabricated using two methods: cold isostatic pressing (CIP) followed by sintering and binder-jet 3D printing followed by also binder burn out and subsequent sintering in order to study the effect of Ca and Mg addition on the degradation properties of the Fe-Mn system. The mechanically alloyed powders were consolidated using cold isostatic pressing (CIP) followed by sintering at 1200 °C under a gettered ultra-high purity (UHP) argon atmosphere. For further studies, Fe-Mn and Fe-Mn-1Ca were selected to fabricate 3D printed specimens using an Ex-Lab machine (The ExOne Company, LLC, North Huntingdon, PA) with a water-based organic binder. The 3D-printed parts were cured at 200 °C for 2 h under air. The cured parts were then heat-treated at, 430 °C for 0.5 h, 620 °C for 0.5 h, and 1200 °C for 3 h to achieve binder burn-out and subsequent sintering of the Fe-Mn and Fe-Mn-1Ca alloys.

A.2.4 Physical properties

Absolute density of the 3D-printed parts corresponding to dimension of 10 x 10 x 4 mm, was measured using an AccuPyc II 1340 helium pycnometer (Micromeritics, Norcross, GA). The envelope density of the 3D-printed parts was then measured using a GeoPyc 1360 (Micromeritics). Using these density values, percent open porosity was calculated using the following equation:

Open porosity (%) = ((absolute density – envelope density)/absolute density) x 100 Eq. 1

Percentage shrinkage of 3D-printed parts before and after sintering was calculated from the volume as measured by the GeoPyc 1360 of the sintered parts and the measured volumes of the parts before sintering.

A.2.5 Mechanical properties

Tensile test analyses was conducted in accordance with ASTM-E8-04. Bar specimens were printed, cured, sintered, and finally machined into a standard dog-bone shape with a gauge length of 13.5 mm, width of 3 mm, and thickness of 3 mm. Uniaxial tensile testing was performed at room temperature with an Instron machine, using a cross-head speed of 1.3 mm/min and a 5 kN load cell. Yield strength (YS), ultimate tensile strength (UTS), Young’s modulus (E), and percent elongation (%) were determined from the stress-strain curves generated from each specimen. Young’s modulus was obtained by considering the linear portion of the curves.

Average and standard deviations of these 3 sample measurements are reported. Averages and standard deviations of 3 sample measurements were reported and t-test was used to determine any significant mean differences with a p-value less than 0.05.

A.2.6 Electrochemical corrosion test

Potentiodynamic polarization testing was conducted to assess the degradation rates of the 3D specimens. The specimens, with a surface area of ~0.5 cm^2, were connected to a copper wire using a silver epoxy and finally mounted in epoxy resin. The mounted samples were mechanically polished with an increasingly small abrasive size up to 1 μm, sonicated in isopropyl alcohol, and air dried. An electrochemical workstation (CHI 604A, CH Instruments, Inc., Austin, TX) was employed to conduct the test with three-electrode cell setup utilizing platinum as the counter-electrode, Ag/AgCl as the reference electrode and the epoxy-mounted sample as the working electrode. The test was performed using Hank's Balanced Salts Solution (HBSS H1387, Sigma-Aldrich, Canada) with 0.35 g l^{-1} sodium bicarbonate warmed to 37.4 ^{o}C to mimic the physiological conditions. Tafel analysis was used to determine the equilibrium corrosion current, I_{corr}, and the corrosion potential, E_{corr}, obtained as the intersection of the linearly fitted cathodic and anodic branches of the generated Tafel plot similar to the studies conducted in Chapter 3 and 4. Averages and standard deviations of 3 sample measurements were reported.

A.2.7 Live/dead direct cell viability assay

To access the direct cell cytotoxicity, the murine osteoblast-like cell line, MC3T3 (ATCC, Rockville, MD), was cultured on the surface of 3D-printed plate specimens. The 3D-printed specimens with dimensions of 10 x 10 x 1 mm were polished up to 1200 grit using SiC paper, sonicated in isopropyl alcohol, and sterilized using UV radiation for 30 min. Modified Eagle’s medium alpha (αMEM) supplemented with 10% FBS, 100 U ml−1 penicillin and 100 µg ml−1 streptomycin was used as culture medium. MC3T3 cells were seeded onto specimen surfaces at cell density of 4 × 104 cells ml−1 and incubated at 37.4 °C in a humidified atmosphere with 5% CO2. After 72 h of incubation, cell cytotoxicity was assessed by performing live/dead cell viability assay using commercially available kit (Invitrogen Corporation, Karlsruhe, Germany) and following the manufacturer’s protocol. During the assay, the live and dead cells were stained using ethidium homodimer-1 and calcein-AM respectively, which exhibits live cells as green and dead cells as red under fluorescence imaging at the excitation wavelength of 495 and 528 nm similar to studies reported in Chapter 3 and 4. After the assay, the cells were fixed by immersing the specimens with cells in 2.5% glutaraldehyde for 15 min followed by dehydration steps subsequently in 70, 80, 90, 95 and 100% diluted ethanol for 15 min each. Specimens with fixed cells were then air-dried and imaged using scanning electron microscopy.

A.2.8 Indirect MTT cell cytotoxicity assay

MC3T3 cells were also used to assess *in vitro* cytotoxicity of the extract media prepared by immersing 3D-printed specimens in culture medium. Modified Eagle’s medium alpha (αMEM) with 10% FBS, 100 U ml−1 penicillin and 100 µg ml−1 streptomycin was used as this cell culture media. Prior to the extract media preparation, the 3D-printed specimens were fabricated to have dimensions of 10 x 10 x 4 mm and polished up to 1200 grit to match the surface finish used in live/dead direct cell viability testing. The ratio of culture media volume to specimen weight was maintained at 1 mL to 0.2 g, according to EN ISO 10993:12. After 72 h incubation, the extract media was filtered using 0.2 μm membrane, this filtered extract was designated as 100% extract. The 100% extract was subjected to inductively coupled plasma – optical emission spectroscopy (ICP-OES) to measure chemical concentration of Fe, Mn, and Ca. For this, 100% extract was then diluted to 50%, 25%, and 10% extract solutions. MC3T3 cells were seeded in a 96-well plate with a cell density of 6,000 cells per well. After 24 h of incubation, the culture media was replaced with the 100%, 50%, 25%, and 10% extract media and cells were further incubated for 72 h. Vybrant MTT Cell Proliferation Kit (Invitrogen Corporation, Karlsruhe, Germany) was used to assess the cytotoxity of the extract media. After 72 h culture, the extract media was replaced with fresh culture media to prevent any interaction between the metal ions and 3-(4,5-dimethylthiazol-2-yl)-2,5-diphenyltetrazolium bromide (MTT). 12 mM MTT in phosphate buffered saline (PBS) was diluted 10x using culture media and 110 μL of diluted MTT solution was added to each well for 4 h of incubation. Formazan crystal was solubilized using sodium dodecylsulfate–hydrochloric acid solution solution, incubated for 12 h, and analyzed at a wavelength of 570 nm using Synergy 2 microplate reader (BioTek Instruments, Winooski, VT). Furthermore, in order to check the tolerance of metal ion contents from the Fe alloys' degradation products, 0.1, 1, and 10 mM of Fe, Mn, and Ca were prepared by dissolving their chlorides in culture media, applied to MC3T3-E1 cells for 7 days, and followed by MTT assay. Averages and standard deviations of 3 sample measurements were reported and two-way

ANOVA with Tukey’s post-hoc test was used to determine any significant mean differences with a p-value less than 0.05.

A.3 RESULTS

A.3.1 Theoretical and experimental approaches to develop degradable Fe-based powder alloys

CALPHAD results

For evaluation of the effect of Ca and Mg on the corrosion behavior of Fe-Mn alloy, the following compositions have been chosen in the present computational study: Fe65Mn(35-x)(Ca/Mg)x, where x represents the percent composition by weight 0<x<5 wt.%. Hydrolysis of pure Fe has been considered as a reference point.

The resulting dependence of δΔGR on chemical composition of the Fe-Mn alloys is shown in Figure A.1. On this graph, the hydrolysis of pure Fe is set at zero energy and all ΔGR for the alloys was calculated in comparison with ΔGRFe for pure Fe. A horizontal dashed line at -42.0 kJ/mol denotes δΔGR for the Fe65Mn35 alloy composition as the reference.

One can see that all lines representing changes of the free energy for all the Fe-based alloys are located at the negative area of the graph, implying that the effects of all thermodynamic stimuli for the hydrolytic reactions are larger (more negative) than that for hydrolysis of pure Fe. Increased negativity is a result of higher stability of Mn, Ca, and Mg oxides and hydroxides (the hydrolytic products) in comparison with analogous substances of Fe.

This may therefore indicate a lower stability of the Fe-Mn based alloys in the aqueous environment compared to pure Fe suggesting faster corrosion.

Two sloped lines represent δΔGR for Fe-Mn alloys doped with Ca and Mg. One can see that both doping elements increase the overall thermodynamic stimulus of the hydrolysis, although to different extents. Oxides and hydroxides of both Ca and Mg are more stable than that of Mn and thus, partial substitution of Ca and Mg for Mn in Fe-Mn alloy should lead to more negative δΔGR, in turn leading to lower stability of the Fe-Mn-Ca/Mg alloys compared to undoped Fe-Mn suggesting faster corrosion for these Ca and Mg containing Fe-Mn alloys.

Thus, according to the results shown on Figure A.1, the corrosion rate of Fe-Mn doped with Ca and Mg is expected to be higher than the corrosion rate of undoped Fe-Mn alloy. Doping with Mg has a stronger effect on the corrosion rate than doping with Ca, as seen by the higher corrosion rate of the Mg doped alloy compared to the same weight fraction of Ca. Although this computational study considers only thermodynamic aspects of the hydrolysis without taking into account any kinetic parameters of the process. Nevertheless, these qualitative results are in excellent agreement with experimental measurements of the corrosion rates of the materials as will be shown in further sections of the work reported herein.

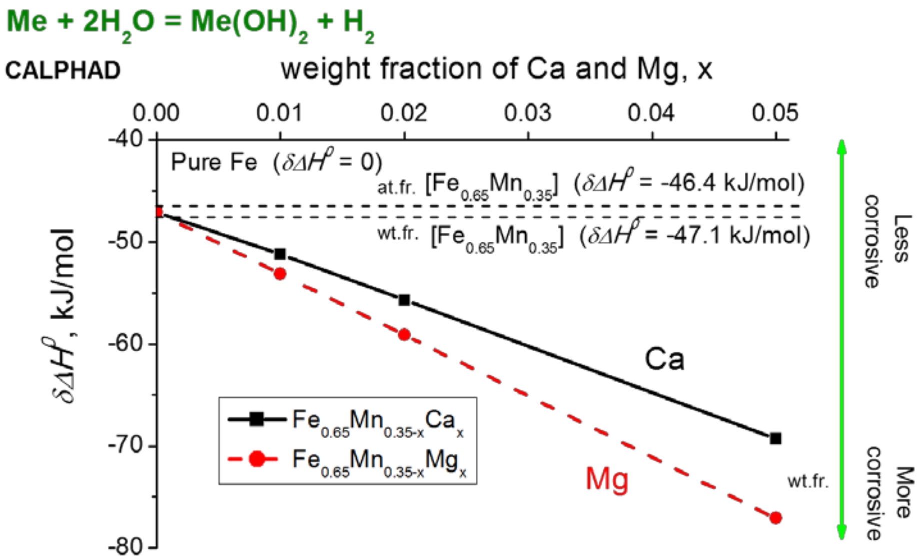

Figure A.1 Results of CALPHAD simulations on the effect of adding Ca and Mg to binary Fe-Mn alloy for enhanced corrosion.

Powder Synthesis

Figure A.2 exhibits the X-ray diffraction patterns of as-milled Fe-Mn-Ca and Fe-Mn-Mg alloy powders. Binary Fe-Mn alloys are known to consist of ɤ-phase austenite and ε-phase martensite phases (187). Mechanically alloyed Fe-Mn also exhibited ɤ- and ε- phase in the diffraction pattern. No undesired phase transformation was observed as an effect of introducing Ca and Mg in the solid solution. Distinct peaks of pure Ca or Mg were also not still observed in Fe-Mn-2Ca or Fe-Mn-2Mg alloy composition prepared by HEMA. Homogeneous solid solutions of Fe-Mn-Ca and Fe-Mn-Mg alloy powders were thus obtained and subjected to further *in vitro* assessment as well as mechanical testing and microstructure evaulation.

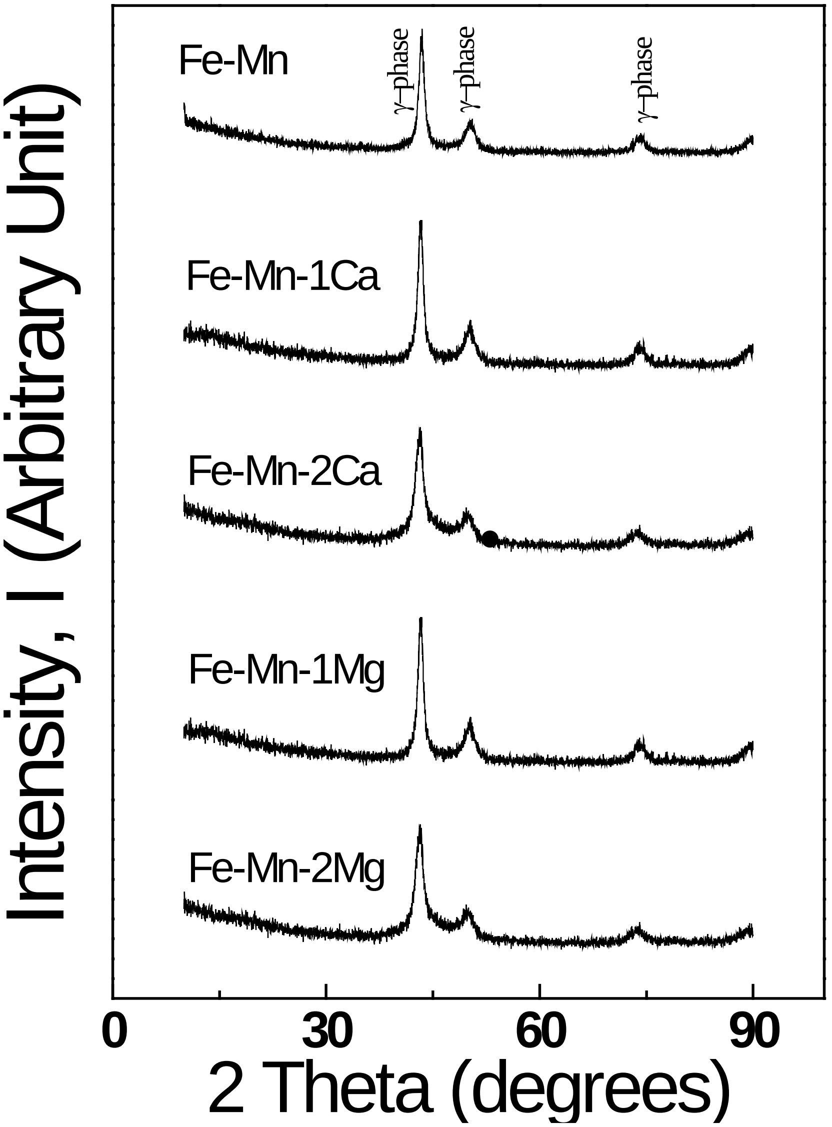

Figure A.2 X-ray diffraction patterns of Fe-Mn, Fe-Mn-Ca, and Fe-Mn-Mg alloy powders.

Electrochemical corrosion of compacted samples

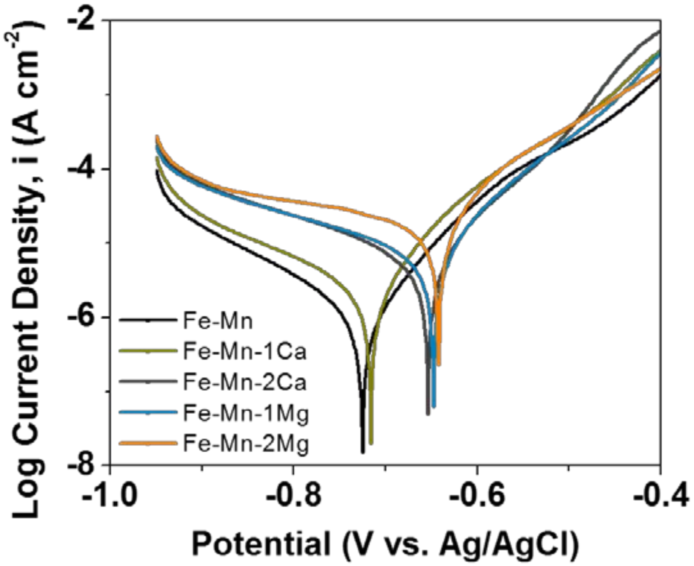

Figure A.3 Tafel curves from potentiodynamic polarization measurements of Fe-Mn, Fe-Mn-Ca, and Fe-Mn-Mg compacted pellets.

The potentiodynamic polarization behavior of sintered Fe-Mn, Fe-Mn-Ca, and Fe-Mn-Mg compacted pellet was recorded at a scan rate of 1 mVs^{-1} and plotted in a Tafel plot shown in Figure A.3. The representative curve for each group of alloy was based on the average corrosion potential and current density after testing multiple samples (N = 6). Tafel plots were used to determine the corrosion current density, corrosion potential, and corrosion rate. Average values of these calculations are tabulated in Table A.1. Addition of Ca or Mg to the Fe-Mn alloys increased both the corrosion potential and the current density to shift toward the positive side. Although the corrosion potential was increased suggesting that the alloy containing Ca and Mg is likely more stable than the pure Fe-Mn alloy, the corrosion current densities indeed reflected higher values suggesting the true corrosion propensity of introducing Ca and Mg into the Fe-Mn alloy system. Thus corrosion current density of the alloys increased from 1.00 μA cm^{-2} to 2.12 μA cm^{-2} and 6.36 μA cm^{-2} after replacing 1 and 2 wt. % of Mn with Ca respectively. Similarly, by introducing Mg into the solid solution, the corrosion current density was increased from 1.00 μA cm^{-2} to 5.89 μA cm^{-2} and 9.16 μA cm^{-2} after replacing 1 and 2 wt. % of Mn. Corrosion current density is linearly correlated with a corrosion rate, and an increase in corrosion current density implies higher corrosion rate. Hence as mentioned above, the present electrochemical test results exhibit enhanced degradation properties of Fe-Mn alloys alloyed with Ca or Mg content.

Table A.1 Corrosion potential and corrosion current density of Fe-Mn, Fe-Mn-Ca, and Fe-Mn-Mg compacted pellets (n=3).

Material	Corrosion potential, E_{corr} [V]	Corrosion current density, i_{corr} [μA cm^{-2}]
Fe-Mn	-0.72±0.04	1.00±0.06
Fe-Mn-1Ca	-0.71±0.02	2.12±0.92
Fe-Mn-2Ca	-0.66±0.02	6.36±1.75
Fe-Mn-1Mg	-0.65±0.02	5.89±0.80
Fe-Mn-2Mg	-0.64±0.03	9.16±1.25

Live/dead cell viability of compacted samples

Fluorescent images of the live/dead assay are obtained, as shown in Figure A.4, after 1 and 3 days of culturing osteoblastic MC3T3-E1 cells on the sintered pellets of Fe-Mn, Fe-Mn-Ca, and Fe-Mn-Mg alloy powders. Live cells are represented by a fluorescent green, a result of intracellular conversion of calcein-AM to calcein. Dead cells glow in red fluorescent due to the compromised cell membrane that permits binding of nucleic acid with ethidium D-1. More live cells were observed in the fluorescent images after 3 days compared to the images after 1 days. Both Fe-Mn-1Ca and Fe-Mn-2Ca exhibited more live cells compared to Fe-Mn or Fe-Mn-Mg specimens suggesting the likely better cytocompatibility of incorporating Ca into the Fe-Mn alloy system in comparison to introduction of Mg.

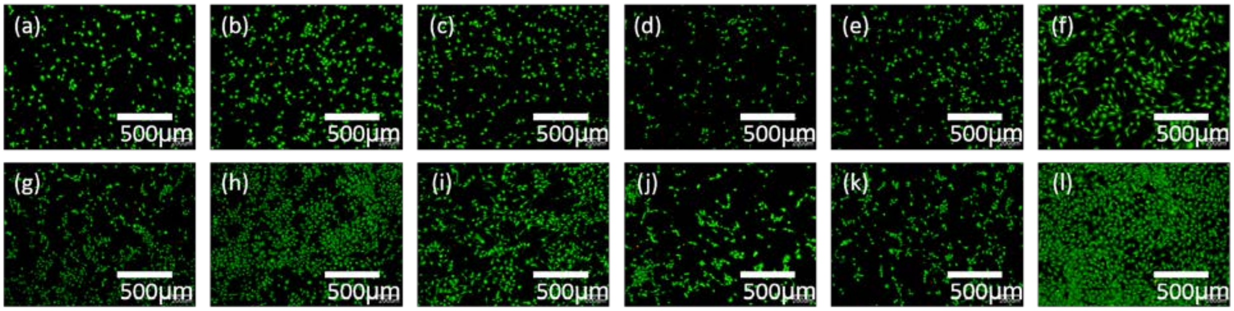

Figure A.4 Fluorescent images of live dead cell viability of MC3T3-E1 cells seeded on the compacted pellets of (a) Fe-Mn, (b) Fe-Mn-1Ca, (c) Fe-Mn-2Ca, (d) Fe-Mn-1Mg, (e) Fe-Mn-2Mg, and (f) cell culture plastic control after 1 day culture. Respective results of the 3 day culture are seen in fluorescence images (g)-(l).

A.3.2 3D printing of Fe-based powder and in vitro assessment

Fabrication of 3D printed specimens

Table A.2 Density, porosity, and shrinkage measurements after sintering of 3DP Fe-Mn and Fe-Mn-1Ca.

	Absolute density [g/cm³]	Envelope density [g/cm³]	Open porosity [%]	Percent of shrinkage [%]
Fe-Mn	7.73	4.69	39.3	31.6
Fe-Mn-1Ca	7.48	3.53	52.9	11.7

In order to validate the effect of adding Ca on 3D printing, Fe-Mn and Fe-Mn-1Ca alloy powders were chosen for comparison. This selection was based on good cytocompatibility of sintered Fe-Mn-Ca pellets compared to the Fe-Mn-Mg pellets as discussed above. Hence, 3D printing of Fe-Mn and Fe-Mn-1Ca alloy powder was performed using the binder-jet 3D printing approach. SEM images of both initial alloy powder and sintered 3D printed specimens were obtained as seen in Figure A.5. Fe-Mn and Fe-Mn-1Ca alloy powders are observed in various sizes with diameters between 5-30μm. Micro pores in the diameter of ~ 5μm are shown on the surface of sintered Fe-Mn and Fe-Mn-Ca specimens. Absolute and envelop density measurement results are tabulated in Table A.2. Higher shrinkage and lower open porosity after sintering was observed for Fe-Mn compared to Fe-Mn-1Ca. SEM images confirmed the powder-powder diffusion after sintering the 3D-printed specimens for both Fe-Mn and Fe-Mn-Ca, although some differences in

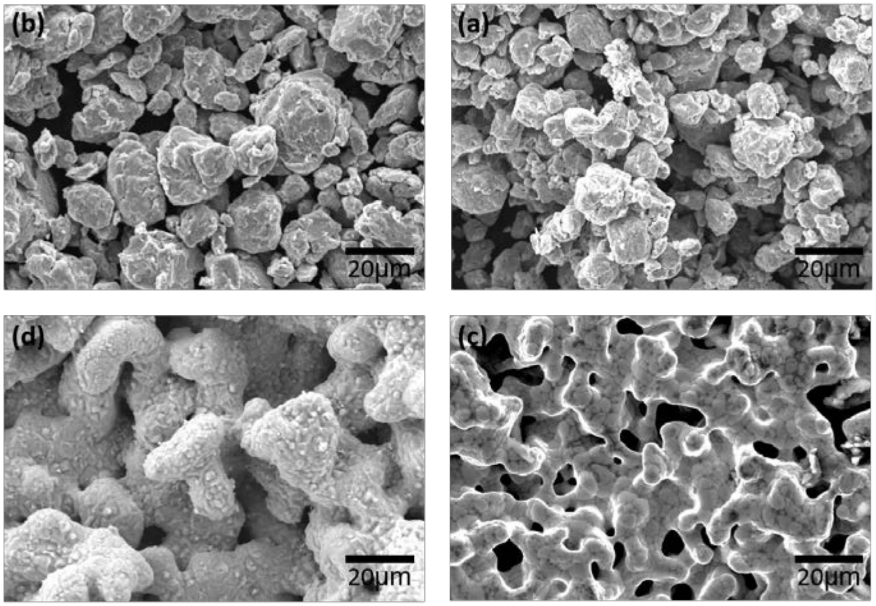

Figure A.5 Morphology of (a) Fe-Mn powders (b) Fe-Mn-1Ca powders, (c) 3DP Fe-Mn sample, and (d) 3DP Fe-Mn-1Ca sample.

densification occurred during the sintering process. Thus, the 3D-printed specimens were further tested in terms of degradation, cytotoxicity, and mechanical properties.

Electrochemical corrosion of 3D printed specimens

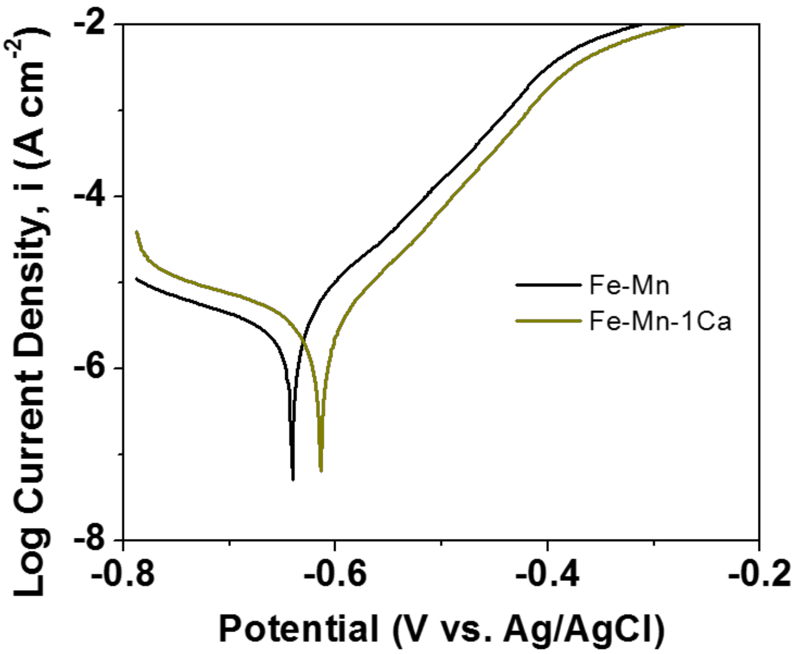

Figure A.6 Representative tafel curves from potentiodynamic polarization measurement of 3DP Fe-Mn, and Fe-Mn-1Ca.

Tafel plots of 3D-printed Fe-Mn, and Fe-Mn-1Ca specimens was obtained through scanning at the rate of 1mV s-1, as shown in Figure A.6. A representative curve is shown for each group based on the average corrosion potential and current density after testing multiple samples (N=4). Tafel plots were used to determine the corrosion current density, corrosion potential, and corrosion rate and the average values are tabulated in Table A.3. Porous morphology of 3D-printed specimens was not considered for these calculations, nominal surface area was instead used to calculate corrosion current density. Corrosion potential of Fe-Mn, and Fe-Mn-1Ca was -0.64 V, and -0.63 V, respectively indicating higher corrosion propensity of Fe-Mn alloy similar to the CIP derived systems discussed earlier. After normalization using surface area, the corrosion current density of 3D-printed Fe-Mn-1Ca was 2.88 µA/cm2 (Table A.3), slightly improved from the corrosion current density of compacted Fe-Mn-1Ca, 2.12 µA/cm2 (Table A.1) and that of the 3D printed Fe-Mn corrosion current density of 2.21 µA/cm2 (Table A.3).

Table A.3 Corrosion potential and corrosion current density of 3DP Fe-Mn and Fe-Mn-1Ca (n=4).

	Corrosion potential, E corr [V]	Corrosion current density, I corr [µA/cm^2]
Fe-Mn	-0.64±0.02	2.21±0.35
Fe-Mn-1Ca	-0.63±0.02	2.88±0.54

Figure A.7 presents the surface morphology after the potentiodynamic polarization test of 3DP Fe-Mn and Fe-Mn-1Ca. Exposed surface areas of both samples exhibited different pore sizes. Although nominal surface area is used to calculate the corrosion current density tabulated in Table A.3, the actual surface area exposed for the testing can be larger due to the porosity of 3DP Fe-Mn and Fe-Mn-1Ca. Corrosion pits were observed on the surface of both samples. The insoluble degradation products correspondingly mainly to iron and manganese oxides that are formed inside of the micropores.

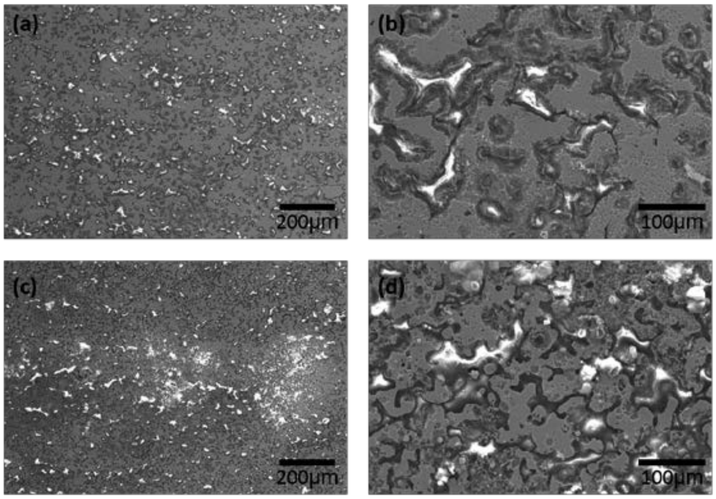

Figure A.7 Surface morphology of 3DP Fe-Mn at (a) 100x (b) 500x and 3DP Fe-Mn-1Ca at (c) 100x (d) 500x after potentiodynamic polarization measurement.

In vitro cytoxicity test of 3D printed specimens

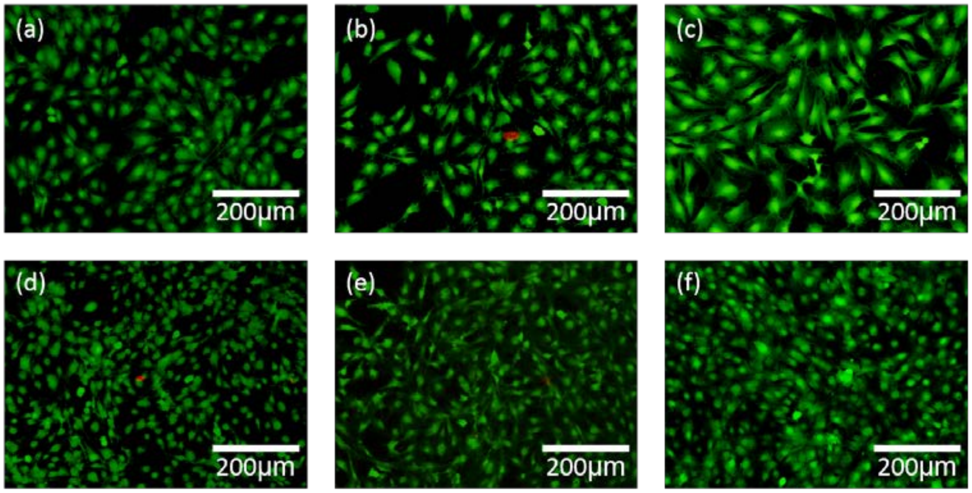

Figure A.8 Fluorescence images of live dead cell viability of MC3T3-E1 cells on (a) 3DP Fe-Mn, (b,) 3DP Fe-Mn-1Ca, and (c) cell culture plastic control after 1 day culture. Respective results after 3 days culture are seen in the fluorescence images (d)-(f).

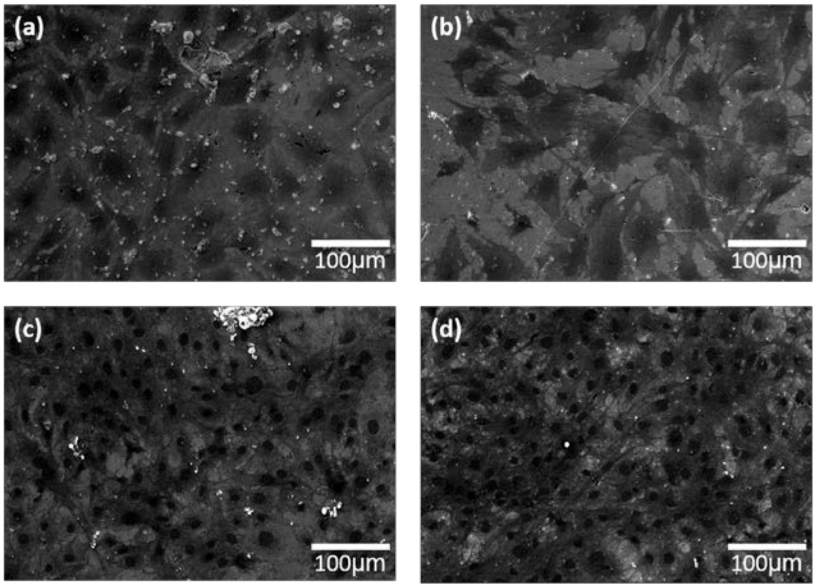

Figure A.9 Scanning electron microscopy (SEM) images of fixed MC3T3-E1 cells after live dead cell viability assay on (a) 3DP Fe-Mn and (b) 3DP Fe-Mn-1Ca for 1 day culture. Respective SEM images of fixed cells for 3 day culture are shown in images (c)-(d).

Fluorescent images of live/dead cell viability assay are presented in Figure A.8 to assess the cytotoxicity of 3D-printed Fe-Mn and Fe-Mn-1Ca. After 1 and 3 day cultures, 3D-printed Fe-Mn and Fe-Mn-1Ca specimens exhibited live cell viability comparable to the tissue culture plastic control. Figure A.9 exhibits the cell morphology after fluorescent imaging of the live/dead cell viability assay. Substantial cell-cell junctions and cytoplasmic extension of MC3T3 cells was observed on 3D-printed Fe-Mn and Fe-Mn-1Ca specimens as shown in Figure A.9.

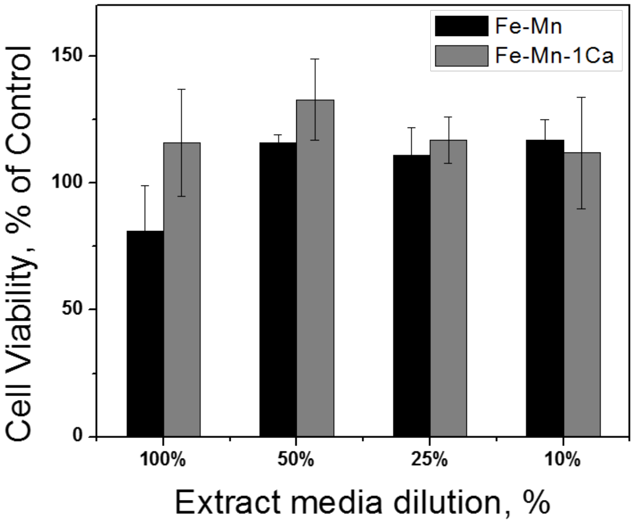

Figure A.10 Indirect MTT cell viability of MC3T3-E1 cells cultured for 3 days with the extract media of 3DP Fe-Mn and Fe-Mn-1Ca (n=3).

The indirect cytotoxicity test result was plotted in Figure A.10 to represent the corrosion extracts derived from 3D-printed Fe-Mn, and Fe-Mn-1Ca samples. After 3 days of culturing MC3T3-E1 in 100% extract, the cell viability assessed using MTT cytoxicity test exhibited in excess of 80% of cell viability, with respect to negative control of cell culture plastic. Cell viability of 50, 25, and 10% extract media diluted with fresh media exhibited ~100% cell viability for both alloy systems. In contrast to the live/dead assay result, no significant difference in cell viability was observed among the different groups. According to ISO protocol for cytotoxicity testing, a 75% or higher cell viability is generally considered a good representation of non-toxicity (123). Thus, good cell viability of 3D-printed Fe-based samples is demonstrated using indirect MTT cytotoxicity test. Similar Fe and Mn compositions were observed in the extract media for both, Fe-Mn compared to Fe-Mn-Ca, while a relatively high Ca concentration compared to its nominal composition in the Fe-Mn-Ca alloy was observed as shown in Table A.4 indicating the higher corrosion propensity of the Fe-Mn-Ca system.

Table A.4 Fe, Mn, and Ca concentration in the extract media of 3DP Fe-Mn and Fe-Mn-1Ca.

	Fe (ppm)	Mn (ppm)	Ca (ppm)
Fe-Mn	3.01	4.53	-
Fe-Mn-1Ca	4.43	4.40	29.12

Figure A.11 illustrates the cell viability of 0.1, 1, and 10 m mol of $FeCl_2$, $MnCl_2$, and $CaCl_2$ dissolved in the culture media after 7 days culture. Cell viability higher than 75% was maintained for Fe and Mn at concentrations up to 1 mM. On the other hand, as expected, Ca and Mg exhibited no cytotoxicity at 10 mM, although higher concentrations of Ca and Mg were not tested for this study.

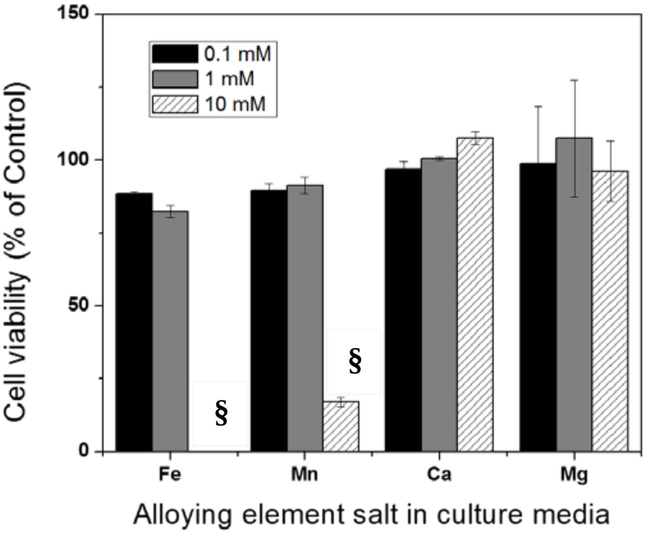

Figure A.11 MC3T3-E1 cytocompatibility of Fe, Mn, Ca, and Mg salt in culture medium at 0.1, 1, and 10 mM concentrations after 7 days of culture (n=3, §$p<0.05$ denotes a significant difference with all other groups).

Mechanical properties

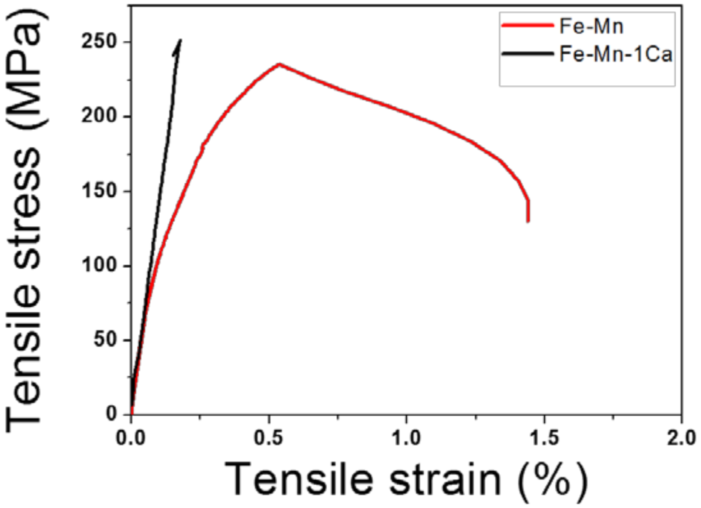

Figure A.12 Representative stress vs. strain curves from tensile testing of 3DP Fe-Mn and Fe-Mn-1Ca.

Stress-strain curves, shown in Figure A.12, represents tensile properties of 3D-printed Fe-Mn, and Fe-Mn-1Ca after sintering. Ultimate tensile strength (UTS), yield strength (YS), elongation (E) and Young's modulus of 3D-printed specimens are tabulated in Table A.5. 3D printed Fe-Mn exhibited an UTS of 228.1 MPa, YS of 189.7 MPa, and modulus of 0.39 GPa. Addition of Ca to Fe-Mn alloy resulted in higher stiffness which increased UTS from 228.1 to 296.6 MPa, and modulus from 0.39 to 1.63 GPa. However, brittle fracture without any yield point was observed in the stress-strain curve of 3D printed Fe-Mn-1Ca and its elongation at fracture was only ~0.1%.

Table A.5 Tensile properties of 3DP Fe-Mn and Fe-Mn-1Ca (n=5, §p<0.05 denotes a significant difference between two groups.

Materials	Ultimate Tensile Strength (MPa)	Modulus (GPa)	Yield Tensile Strength (MPa)
Fe-Mn	228.1±10.6 **§**	0.39±0.05 **§**	189.7±25.6
Fe-Mn-1Ca	296.6±45.8 **§**	1.63±0.2 **§**	-

A.4 DISCUSSION

A.4.1 Strategy for alloying

Various alloying elements or composite materials have been attempted to improve the degradation rate of biodegradable Fe-based alloys. The strategy has been to introduce noble metallic alloying elements such as Pd, Pt, Au, Ag, W, and Si, which tend to cause a galvanic corrosion couple with Fe matrices resulting in enhanced degradation (178, 179, 188, 189). The noble element precipitates can be taken away from the implantation site if the biodegradable Fe alloyed with these alloying elements are used for cardiovascular applications. On the contrary, limited amount of blood and fluid exchange occurs in the areas associated with cranio-maxillofacial bone defects. Among recently published *in vivo* studies of biodegradable Fe-based alloys, rat femoral implantation of pure Fe, Fe–10Mn–1Pd, and Fe–21Mn–0.7C–1Pd pins were used to assess the degradation and biocompatibility of the Fe alloys in bone tissue for up to 52 weeks (181). Very little degradation was observed, and hence, consequently, no sign of toxicity was observed in the CT analysis and histology of the surrounding tissue. Analysis also showed that the in vitro degradation rate of Fe–21Mn–0.7C–1Pd alloy was reported as ~0.13mm/year

(180). Therefore, the present study introduced less corrosion resistant alloying elements, Ca and Mg, to induce higher corrosion to the corrosion resistant Fe system such that these alloys could result in faster degradation from the scaffold prior to the Fe-Mn matrix.

Melting points of both Ca (842 °C) and Mg (650 °C) are low compared to that of Fe (1538 °C) and Mn (1246 °C). Due to this extreme difference in the melting points of Fe and Mn versus Ca and Mg, traditional gas-atomization of the alloy powders is unable to achieve the homogeneous solid solution of the nominal composition. High energy mechanical alloying (HEMA) was therefore used to synthesize Fe-Mn-Ca and Fe-Mn-Mg since Ca and Mg do not have solubility in Fe or Mn. Homogeneous alloy powders of Fe-Mn-Ca and Fe-Mn-Mg were accordingly obtained showing no peaks of pure Ca or Mg in the X-ray diffraction pattern (Figure A.2).

Binder-jet 3D-printed specimens of different compositions with irregular particle morphology can result in different open porosity. Different open porosity is expected to expose different surface area and affect the corrosion measurement. In order to avoid such inconsistencies, compacted pellets of Fe-Mn-Ca and Fe-Mn-Mg were used for the corrosion assessment to demonstrate the increase in degradation rates with addition of Ca and Mg in Fe-Mn alloys. As predicted by the CALPHAD calculation, the effect of adding Ca and Mg was demonstrated by the potentiodynamic polarization result showing an increased corrosion current density related to the amount of Ca and Mg in the solid solution as seen in Table A.1.

Addition of Ca also caused higher Fe concentration in the ICP analysis of the extract media of 3DP Fe-Mn-1Ca compared to 3DP Fe-Mn (Table A.4). This observation is correlated with enhanced degradation properties due to the presence of Ca in Fe-Mn alloy demonstrated and valdidating the CALPHAD calculation and electrochemical corrosion test.

A.4.2 Binder-jet 3D printing

Binder-jet 3D printing of biodegradable Fe alloys demonstrated the ability to enhance degradation rates due to higher exposed surface area of porous structure. Binder-jet 3D printing results in micropores after sintering due to the low as-printed density (190). Chou et. al previously demonstrated an increase in degradation properties of Fe-30Mn mixtures after binder-jet 3D printing (182). Moreover, these micropores create a rough surface finish which can improve osseointegration. For industrial applications, these micropores are infiltrated with the same or different material to improve corrosion resistance and mechanical properties. Medical devices, made of inert metals such as titanium, also share the same dilemma requiring infiltration and smooth surface finish (191). On the other hand, development of a biodegradable Fe-based alloy is focused on increasing the corrosion rate, and micropores induced by binder-jet 3D printing are beneficial to enhance the degradation of biodegradable Fe-based scaffolds. When the potentiodynamic polarization data of compacted pellets and 3D printing samples were compared, 3DP samples exhibited increased corrosion current density in both Fe-Mn and Fe-Mn-1Ca alloys (Table A.1 and A.3). The porous structure of 3DP Fe-Mn and Fe-Mn-1Ca enhanced degradation rate by exposing a larger surface area to the electrolyte.

Insoluble oxide formation was observed in the micropores of 3DP Fe-Mn and Fe-Mn-1Ca after the potentiodynamic polarization test (Figure A.7). These observations convey that the presence of micropores from binder-jet 3D printing can increase the contact with electrolytes and enhance the degradation of biodegradable Fe-based alloy.

A.4.3 Indirect cytocompatibility of biodegradable Fe alloys

Indirect cytocompatibility of biodegradable Fe alloys has been assessed using various types of cells such as fibroblast, smooth muscle cells, and osteoblasts depending on the target application (178, 179, 182). In this study, the cytocompatibility of 3DP Fe-Mn and Fe-Mn-1Ca alloys were investigated for their potential use as cranio-maxillofacial implants. Cranio-maxillofacial implants are placed in direct contact with bone tissues within the human body. As the material corrodes within the body, it releases metallic ions which may be harmful to cellular functions. Therefore, degradation products of these implants must be compatible with associated bone cells. For this reason, mouse pre-osteoblast MC3T3-E1 cells were used to test the cytocompatibility of possible implant materials.

MTT assay results exhibited good cytocompatibility with 100%, 50%, 25%, and 10% extract media of 3DP Fe-Mn and Fe-Mn-1Ca, as shown in Figure A.10. ICP analysis on 100% extract exhibited ~5 ppm (equivalent to ~0.1 mM) Fe and Mn concentration as well as ~29 ppm (equivalent to ~0.7 mM) additional calcium concentration in 3DP Fe-Mn-1Ca extract. Ionic concentration of Fe and other alloying elements in the extract media is closely correlated with the cell viability. Purnama et al. reported the fibroblast cell count after dosing different concentration of $FeCl_2$ and $MnCl_2$ to check the tolerance of fibroblasts against the metal ion concentration (192). At 25 ppm (equivalent to ~0.5 mM) of $MnCl_2$ and 150 ppm (equivalent to ~3 mM) of $FeCl_2$, the fibroblast cell count was halved. Unlike the fibroblast, MC3T3 pre-osteoblasts tested here indicated that they were cytocompatible with 1mM concentration of $FeCl_2$ and $MnCl_2$ (Figure A.11).

The metal ion concentration from 3DP Fe-Mn and Fe-Mn-1Ca reaches approximately 10% of tolerable amounts (Table A.4 and Figure A.11). Hence, higher degradation rate can be pursued by altering the composition in the next development process.

A.4.4 Mechanical properties

Ultimate tensile strength of 3DP Fe-Mn (228.1 MPa) and Fe-Mn-1Ca (296.6 MPa) was higher than that of human cortical bone. 3DP Fe-based medical devices for cranio-maxillofacial application are anticipated to be implanted in semi-loaded or non-load bearing sites. Porous structure of 3DP Fe-Mn-1Ca with 52.1% open porosity resulted in brittle fracture during tensile testing. Ductility of 3DP Fe-Mn-1Ca needs to be improved to qualify for load-bearing bone implant applications that require toughness since both strength and ductility contribute to toughness. 3DP Fe-Mn with 39.1% open porosity exhibited higher ductility than 3DP Fe-Mn-1Ca; this suggests that less porosity can improve the ductility of 3DP Fe-based alloys. Hermawan et al. reported UTS and elongation at fracture of rolled bulk Fe-35Mn as 550 MPa and 31% respectively (175), with the significantly higher strength as a result of the near-fully dense material compared to the porous 3DP material reported here. Electron beam-based or laser-based 3D fabrication can be a solution to achieve higher densification and mechanical properties since these techniques do not result in micropores due to instant particle to particle diffusion, melting and subsequent solidification. Also, 3DP Fe-based alloys can be infiltrated either with the same material, ceramic or biodegradable polymers to improve the toughness although a decrease in porosity will result in a decrease of the material degradation rate.

A.5 CONCLUSION

In this study, theoretical calculation was performed to predict an effect of introducing Ca and Mg on corrosion behavior of biodegradable Fe-Mn alloy. Fe-Mn-Ca and Fe-Mn-Mg alloys were synthesized and the sintered pellets of the alloys were analyzed in terms of corrosion and cytotoxicity properties. Furthermore, Fe-Mn and Fe-Mn-Ca exhibited good cytotoxicity results and thus were selected for binder-jet 3D printing studies. Based on the results, the main conclusions are listed as follows:

(1) CALPHAD calculation exhibited an increase in corrosion rates of binary Fe-35Mn alloy by replacing Mn content with Ca and Mg. Synthesized powder of Fe-Mn-Ca and Fe-Mn-Mg exhibited ɤ-phase austenite and ε-phase martensite solid solution without distinct Ca or Mg peaks in X-ray diffraction patterns.

(2) Sintered pellets of Fe-Mn-Ca and Fe-Mn-Mg demonstrated that the corrosion current density increased with Ca or Mg content in the potentiodynamic polarization testing validating the theoretical CALPHAD studies. The pellets exhibited good cytocompatibility after 1 and 3 days culture of MC3T3 culture followed by live/dead cell viability assay.

(3) 3D-printed specimens of Fe-Mn and Fe-Mn-1Ca presented 39.1 and 52.1% open porosity respectively. Micro pores in size of ~5um diameter were observed under scanning electron microscopy.

(4) The corrosion current density of 3D-printed Fe-Mn and Fe-Mn-1Ca was greater than that of sintered pellets. 3D-printed Fe-Mn-1Ca exhibited higher corrosion current density compared to 3D-printed Fe-Mn.

(5) 3D-printed Fe-Mn and Fe-Mn-1Ca also exhibited good cytocompatibility with MC3T3 cells assessed using both direct live/dead and indirect MTT cell viability assays. In terms of

mechanical properties, Fe-Mn-1Ca exhibited higher stiffness and brittle failure in tensile testing but higher UTS was observed in comparison to Fe-Mn.

BIBLIOGRAPHY

1. Johansson J, Nordström A, Nordström P. Objectively measured physical activity is associated with parameters of bone in 70-year-old men and women. Bone. 2015;81:72-9.

2. Sullivan F. U.S. Medical Devices Market Outlook. 2008.

3. Cornell CN, Levine D, Pagnani MJ. Internal fixation of proximal humerus fractures using the screw-tension band technique. J Orthop Trauma. 1994;8(1):23-7.

4. Goel A, Laheri V. Plate and screw fixation for atlanto-axial subluxation. Acta neurochirurgica. 1994;129(1):47-53.

5. Damien CJ, Parsons JR. Bone graft and bone graft substitutes: a review of current technology and applications. Journal of Applied Biomaterials. 1991;2(3):187-208.

6. Claes L, Recknagel S, Ignatius A. Fracture healing under healthy and inflammatory conditions. Nat Rev Rheumatol. 2012;8(3):133-43.

7. Claes L. Biomechanical principles and mechanobiologic aspects of flexible and locked plating. J Orthop Trauma. 2011;25 Suppl 1:S4-7.

8. McKibbin B. The biology of fracture healing in long bones. The Journal of bone and joint surgery British volume. 1978;60-B(2):150-62.

9. Kolar P, Schmidt-Bleek K, Schell H, Gaber T, Toben D, Schmidmaier G, et al. The early fracture hematoma and its potential role in fracture healing. Tissue Eng Part B Rev. 2010;16(4):427-34.

10. Kędra M, Rybojad P, Jendrej J, Sawicki M. Intraspinal K-wire migration after humeral fracture fixation. European Journal of Cardio-Thoracic Surgery. 2011;39(6):1079.

11. Jacobs JMS, Dec W, Levine JP, McCarthy JG, Weimer K, Moore K, et al. Best Face Forward: Virtual Modeling and Custom Device Fabrication to Optimize Craniofacial Vascularized Composite Allotransplantation. Plastic and Reconstructive Surgery. 2013;131(1):64-70 10.1097/PRS.0b013e3182729ef0.

12. Wang K. The use of titanium for medical applications in the USA. Materials Science and Engineering a-Structural Materials Properties Microstructure and Processing. 1996;213(1-2):134-7.

13. Uhthoff HK, Poitras P, Backman DS. Internal plate fixation of fractures: short history and recent developments. J Orthop Sci. 2006;11(2):118-26.

14. Gefen A. Computational simulations of stress shielding and bone resorption around existing and computer-designed orthopaedic screws. Med Biol Eng Comput. 2002;40(3):311-22.

15. Regel JP, Pospiech J, Aalders TA, Ruchholtz S. Intraspinal migration of a Kirschner wire 3 months after clavicular fracture fixation. Neurosurg Rev. 2002;25(1-2):110-2.

16. Coen N, Kadhim MA, Wright EG, Case CP, Mothersill CE. Particulate debris from a titanium metal prosthesis induces genomic instability in primary human fibroblast cells. British journal of cancer. 2003;88(4):548-52.

17. Haynes DR, Rogers SD, Hay S, Pearcy MJ, Howie DW. The differences in toxicity and release of bone-resorbing mediators induced by titanium and cobalt-chromium-alloy wear particles. The Journal of bone and joint surgery American volume. 1993;75(6):825-34.

18. Wang JC, Yu WD, Sandhu HS, Betts F, Bhuta S, Delamarter RB. Metal debris from titanium spinal implants. Spine. 1999;24(9):899-903.

19. Rezwan K, Chen QZ, Blaker JJ, Boccaccini AR. Biodegradable and bioactive porous polymer/inorganic composite scaffolds for bone tissue engineering. Biomaterials. 2006;27(18):3413-31.

20. Nair LS, Laurencin CT. Biodegradable polymers as biomaterials. Progress in Polymer Science. 2007;32(8–9):762-98.

21. Nair L, Laurencin C. Polymers as Biomaterials for Tissue Engineering and Controlled Drug Delivery. In: Lee K, Kaplan D, editors. Tissue Engineering I. Advances in Biochemical Engineering/Biotechnology. 102: Springer Berlin Heidelberg; 2006. p. 47-90.

22. Babensee JE, McIntire LV, Mikos AG. Growth factor delivery for tissue engineering. Pharmaceutical research. 2000;17(5):497-504.

23. Dimitriou R, Jones E, McGonagle D, Giannoudis PV. Bone regeneration: current concepts and future directions. BMC Medicine. 2011;9:66-.

24. Tannoury CA, An HS. Complications with the use of bone morphogenetic protein 2 (BMP-2) in spine surgery. The Spine Journal. 2014;14(3):552-9.

25. Cooper GS, Kou TD. Risk of cancer following lumbar fusion surgery with recombinant human bone morphogenic protein-2 (rh-BMP-2). Spine. 2013;38(21):1862.

26. LeGeros RZ. Properties of Osteoconductive Biomaterials: Calcium Phosphates. Clinical Orthopaedics and Related Research. 2002;395:81-98.

27. BAILEY CA, KUIPER JH, KELLY CP. Biomechanical Evaluation of a New Composite Bioresorbable Screw. Journal of Hand Surgery (British and European Volume). 2006;31(2):208-12.

28. Tecklenburg K, Burkart P, Hoser C, Rieger M, Fink C. Prospective Evaluation of Patellar Tendon Graft Fixation in Anterior Cruciate Ligament Reconstruction Comparing Composite Bioabsorbable and Allograft Interference Screws. Arthroscopy: The Journal of Arthroscopic & Related Surgery. 2006;22(9):993-9.

29. Kurtz SM, Devine JN. PEEK biomaterials in trauma, orthopedic, and spinal implants. Biomaterials. 2007;28(32):4845-69.

30. Ponnappan RK, Serhan H, Zarda B, Patel R, Albert T, Vaccaro AR. Biomechanical evaluation and comparison of polyetheretherketone rod system to traditional titanium rod fixation. The Spine Journal. 2009;9(3):263-7.

31. Torres Y, Trueba P, Pavo, x, n JJ, Rodriguez JA, editors. Titanium for biomedical application with radial graded porosity: Development of a novel compaction device. Health Care Exchanges (PAHCE), 2013 Pan American; 2013 April 29 2013-May 4 2013.

32. Niinomi M, Nakai M. Titanium-based biomaterials for preventing stress shielding between implant devices and bone. International journal of biomaterials. 2011;2011.

33. Matthew IR, Frame JW. Ultrastructural analysis of metal particles released from stainless steel and titanium miniplate components in an animal model. Journal of Oral and Maxillofacial Surgery. 1998;56(1):45-50.

34. Bahr W, Stricker A, Gutwald R, Wellens E. Biodegradable osteosynthesis material for stabilization of midface fractures: experimental investigation in sheep. Journal of Cranio-Maxillofacial Surgery. 1999;27(1):51-7.

35. Ferretti C. A prospective trial of poly-L-lactic/polyglycolic acid co-polymer plates and screws for internal fixation of mandibular fractures. International journal of oral and maxillofacial surgery. 2008;37(3):242-8.

36. Bai B, Jazrawi LM, Kummer FJ, Spivak JM. The use of an injectable, biodegradable calcium phosphate bone substitute for the prophylactic augmentation of osteoporotic vertebrae and the management of vertebral compression fractures. Spine. 1999;24(15):1521-6.

37. Daculsi G. Biphasic calcium phosphate concept applied to artificial bone, implant coating and injectable bone substitute. Biomaterials. 1998;19(16):1473-8.

38. Staiger MP, Pietak AM, Huadmai J, Dias G. Magnesium and its alloys as orthopedic biomaterials: A review. Biomaterials. 2006;27(9):1728-34.

39. Castellani C, Lindtner RA, Hausbrandt P, Tschegg E, Stanzl-Tschegg SE, Zanoni G, et al. Bone–implant interface strength and osseointegration: Biodegradable magnesium alloy versus standard titanium control. Acta Biomaterialia. 2011;7(1):432-40.

40. Witte F, Abeln I, Switzer E, Kaese V, Meyer-Lindenberg A, Windhagen H. Evaluation of the skin sensitizing potential of biodegradable magnesium alloys. Journal of Biomedical Materials Research Part A. 2008;86A(4):1041-7.

41. Li Y, Wen C, Mushahary D, Sravanthi R, Harishankar N, Pande G, et al. Mg–Zr–Sr alloys as biodegradable implant materials. Acta Biomaterialia. 2012;8(8):3177-88.

42. Witte F, Ulrich H, Palm C, Willbold E. Biodegradable magnesium scaffolds: Part II: Peri-implant bone remodeling. Journal of Biomedical Materials Research Part A. 2007;81A(3):757-65.

43. Feyerabend F, Witte F, Kammal M, Willumeit R. Unphysiologically high magnesium concentrations support chondrocyte proliferation and redifferentiation. Tissue Engineering. 2006;12(12):3545-56.

44. Kraus T, Fischerauer SF, Hänzi AC, Uggowitzer PJ, Löffler JF, Weinberg AM. Magnesium alloys for temporary implants in osteosynthesis: In vivo studies of their degradation and interaction with bone. Acta Biomaterialia. 2012;8(3):1230-8.

45. Gray-Munro JE, Strong M. The mechanism of deposition of calcium phosphate coatings from solution onto magnesium alloy AZ31. Journal of biomedical materials research Part A. 2009;90(2):339-50.

46. Kim K-N, Yang J-E, Jang J-W, Sasikala B, Beng W, Kim I-K. Morphometric analysis on bone formation effect of β-TCP and rhBMP-2 in rabbit mandible. J Korean Assoc Oral Maxillofac Surg. 2010;36(3):161-71.

47. Smith MR, Atkinson P, White D, Piersma T, Gutierrez G, Rossini G, et al. Design and assessment of a wrapped cylindrical Ca-P AZ31 Mg alloy for critical-size ulna defect repair. Journal of biomedical materials research Part B, Applied biomaterials. 2012;100(1):206-16.

48. Yang JX, Cui FZ, Yin QS, Zhang Y, Zhang T, Wang XM. Characterization and Degradation Study of Calcium Phosphate Coating on Magnesium Alloy Bone Implant In Vitro. Ieee Transactions on Plasma Science. 2009;37(7):1161-8.

49. Gray-Munro JE, Seguin C, Strong M. Influence of surface modification on the in vitro corrosion rate of magnesium alloy AZ31. Journal of biomedical materials research Part A. 2009;91(1):221-30.

50. Lin X, Tan LL, Wan P, Yu XM, Yang K, Hu ZQ, et al. Characterization of micro-arc oxidation coating post-treated by hydrofluoric acid on biodegradable ZK60 magnesium alloy. Surf Coat Tech. 2013;232:899-905.

51. Narayanan TSNS, Park IS, Lee MH. Strategies to improve the corrosion resistance of microarc oxidation (MAO) coated magnesium alloys for degradable implants: Prospects and challenges. Prog Mater Sci. 2014;60:1-71.

52. Tang H, Li DY, Chen XP, Wu C, Wang FP. Formation of Ha-Containing Coating on Az31 Magnesium Alloy by Micro-Arc Oxidation. Surf Rev Lett. 2013;20(3-4).

53. Zhao QM, Guo X, Dang XQ, Hao JM, Lai JH, Wang KZ. Preparation and properties of composite MAO/ECD coatings on magnesium alloy. Colloid Surface B. 2013;102:321-6.

54. Erbel R, Di Mario C, Bartunek J, Bonnier J, de Bruyne B, Eberli FR, et al. Temporary scaffolding of coronary arteries with bioabsorbable magnesium stents: a prospective, non-randomised multicentre trial. The Lancet. 2007;369(9576):1869-75.

55. Haude M, Erbel R, Erne P, Verheye S, Degen H, Bose D, et al. Safety and performance of the drug-eluting absorbable metal scaffold (DREAMS) in patients with de-novo coronary lesions: 12 month results of the prospective, multicentre, first-in-man BIOSOLVE-I trial. Lancet. 2013;381(9869):836-44.

56. Campos CM, Muramatsu T, Iqbal J, Zhang Y-J, Onuma Y, Garcia-Garcia HM, et al. Bioresorbable drug-eluting magnesium-alloy scaffold for treatment of coronary artery disease. International journal of molecular sciences. 2013;14(12):24492-500.

57. Waizy H, Diekmann J, Weizbauer A, Reifenrath J, Bartsch I, Neubert V, et al. In vivo study of a biodegradable orthopedic screw (MgYREZr-alloy) in a rabbit model for up to 12 months. Journal of Biomaterials Applications. 2014;28(5):667-75.

58. Windhagen H, Radtke K, Weizbauer A, Diekmann J, Noll Y, Kreimeyer U, et al. Biodegradable magnesium-based screw clinically equivalent to titanium screw in hallux valgus surgery: short term results of the first prospective, randomized, controlled clinical pilot study. Biomed Eng Online. 2013;12:62.

59. Chen D, He Y, Tao H, Zhang Y, Jiang Y, Zhang X, et al. Biocompatibility of magnesium-zinc alloy in biodegradable orthopedic implants. International journal of molecular medicine. 2011;28(3):343-8.

60. Huan ZG, Leeflang MA, Zhou J, Fratila-Apachitei LE, Duszczyk J. In vitro degradation behavior and cytocompatibility of Mg-Zn-Zr alloys. J Mater Sci Mater Med. 2010;21(9):2623-35.

61. Peng Q, Li X, Ma N, Liu R, Zhang H. Effects of backward extrusion on mechanical and degradation properties of Mg-Zn biomaterial. Journal of the mechanical behavior of biomedical materials. 2012;10:128-37.

62. Hong D, Saha P, Chou D-T, Lee B, Collins BE, Tan Z, et al. In vitro degradation and cytotoxicity response of Mg–4% Zn–0.5% Zr (ZK40) alloy as a potential biodegradable material. Acta Biomaterialia. 2013;9(10):8534-47.

63. Alvarez-Lopez M, Pereda MD, del Valle JA, Fernandez-Lorenzo M, Garcia-Alonso MC, Ruano OA, et al. Corrosion behaviour of AZ31 magnesium alloy with different grain sizes in simulated biological fluids. Acta Biomater. 2010;6(5):1763-71.

64. Liu CL, Xin YC, Tang GY, Chu PK. Influence of heat treatment on degradation behavior of bio-degradable die-cast AZ63 magnesium alloy in simulated body fluid. Materials Science and Engineering a-Structural Materials Properties Microstructure and Processing. 2007;456(1-2):350-7.

65. Vojtech D, Cizova H, Volenec K. Investigation of magnesium-based alloys for biomedical applications. Kovove Materialy-Metallic Materials. 2006;44(4):211-23.

66. Chou DT, Hong D, Saha P, Ferrero J, Lee B, Tan Z, et al. In vitro and in vivo corrosion, cytocompatibility and mechanical properties of biodegradable Mg-Y-Ca-Zr alloys as implant materials. Acta Biomater. 2013.

67. Zhao Y, Wu G, Pan H, Yeung KWK, Chu PK. Formation and electrochemical behavior of Al and O plasma-implanted biodegradable Mg-Y-RE alloy. Materials Chemistry and Physics. 2012;132(1):187-91.

68. Hort N, Huang Y, Fechner D, Stormer M, Blawert C, Witte F, et al. Magnesium alloys as implant materials - Principles of property design for Mg-RE alloys. Acta Biomaterialia. 2010;6(5):1714-25.

69. Stulikova I, Smola B. Mechanical properties and phase composition of potential biodegradable Mg–Zn–Mn–base alloys with addition of rare earth elements. Materials Characterization. 2010;61(10):952-8.

70. Leeflang MA, Dzwonczyk JS, Zhou J, Duszczyk J. Long-term biodegradation and associated hydrogen evolution of duplex-structured Mg–Li–Al–(RE) alloys and their mechanical properties. Materials Science and Engineering: B. 2011;176(20):1741-5.

71. Krewski D, Yokel RA, Nieboer E, Borchelt D, Cohen J, Harry J, et al. HUMAN HEALTH RISK ASSESSMENT FOR ALUMINIUM, ALUMINIUM OXIDE, AND ALUMINIUM HYDROXIDE. Journal of toxicology and environmental health Part B, Critical reviews. 2007;10(Suppl 1):1-269.

72. Cannata Andia JB. Aluminium toxicity: its relationship with bone and iron metabolism. Nephrology, dialysis, transplantation : official publication of the European Dialysis and Transplant Association - European Renal Association. 1996;11 Suppl 3:69-73.

73. Kumar V, Gill KD. Aluminium neurotoxicity: neurobehavioural and oxidative aspects. Archives of toxicology. 2009;83(11):965-78.

74. van der Voet GB, Marani E, Tio S, de Wolff FA. Aluminium neurotoxicity. Progress in histochemistry and cytochemistry. 1991;23(1-4):235-42.

75. Cai S, Lei T, Li N, Feng F. Effects of Zn on microstructure, mechanical properties and corrosion behavior of Mg–Zn alloys. Materials Science and Engineering: C. 2012;32(8):2570-7.

76. Li G-Q, Wu G-H, Fan Y, Ding W-J. Effect of the main alloying elements on microstructure and corrosion resistance of magnesium alloys. Zhuzao Jishu(Foundry Technology). 2006;27(1):79-83.

77. Liu M, Schmutz P, Uggowitzer PJ, Song G, Atrens A. The influence of yttrium (Y) on the corrosion of Mg–Y binary alloys. Corrosion Science. 2010;52(11):3687-701.

78. Socjusz-Podosek M, Lityńska L. Effect of yttrium on structure and mechanical properties of Mg alloys. Materials Chemistry and Physics. 2003;80(2):472-5.

79. Yamashita A, Horita Z, Langdon TG. Improving the mechanical properties of magnesium and a magnesium alloy through severe plastic deformation. Materials Science and Engineering: A. 2001;300(1–2):142-7.

80. Li ZJ, Gu XN, Lou SQ, Zheng YF. The development of binary Mg-Ca alloys for use as biodegradable materials within bone. Biomaterials. 2008;29(10):1329-44.

81. Zhang T, Shao Y, Meng G, Cui Z, Wang F. Corrosion of hot extrusion AZ91 magnesium alloy: I-relation between the microstructure and corrosion behavior. Corrosion Science. 2011;53(5):1960-8.

82. Gu X, Zheng Y, Cheng Y, Zhong S, Xi T. In vitro corrosion and biocompatibility of binary magnesium alloys. Biomaterials. 2009;30(4):484-98.

83. Trumbo P, Yates AA, Schlicker S, Poos M. Dietary reference intakes: vitamin A, vitamin K, arsenic, boron, chromium, copper, iodine, iron, manganese, molybdenum, nickel, silicon, vanadium, and zinc. Journal of the American Dietetic Association. 2001;101(3):294-301.

84. Friedrich HE, Mordike BL. Magnesium technology : metallurgy, design data, applications. Berlin ; New York: Springer; 2006. xxii, 677 p. p.

85. Avedesian MM, Baker H, ASM International. Handbook Committee. Magnesium and magnesium alloys. Materials Park, OH: ASM International; 1999. ix, 314 p. p.

86. Chen XB, Nisbet DR, Li RW, Smith PN, Abbott TB, Easton MA, et al. Controlling initial biodegradation of magnesium by a biocompatible strontium phosphate conversion coating. Acta Biomater. 2014;10(3):1463-74.

87. Cui X, Yang Y, Liu E, Jin G, Zhong J, Li Q. Corrosion behaviors in physiological solution of cerium conversion coatings on AZ31 magnesium alloy. Applied Surface Science. 2011;257(23):9703-9.

88. Gao JH, Guan SK, Chen J, Wang LG, Zhu SJ, Hu JH, et al. Fabrication and characterization of rod-like nano-hydroxyapatite on MAO coating supported on Mg-Zn-Ca alloy. Applied Surface Science. 2011;257(6):2231-7.

89. O'Donnell MD, Hill RG. Influence of strontium and the importance of glass chemistry and structure when designing bioactive glasses for bone regeneration. Acta Biomater. 2010;6(7):2382-5.

90. Saidak Z, Marie PJ. Strontium signaling: molecular mechanisms and therapeutic implications in osteoporosis. Pharmacology & therapeutics. 2012;136(2):216-26.

91. Schmidlin PR, Tchouboukov A, Wegehaupt FJ, Weber FE. Effect of cerium chloride application on fibroblast and osteoblast proliferation and differentiation. Archives of Oral Biology. 2012;57(7):892-7.

92. Zhou G, Gu G, Li Y, Zhang Q, Wang W, Wang S, et al. Effects of Cerium Oxide Nanoparticles on the Proliferation, Differentiation, and Mineralization Function of Primary Osteoblasts In Vitro. Biol Trace Elem Res. 2013;153(1-3):411-8.

93. Material ASfTa. ASTM E112 Standard Test Methods for Determining Average Grain Size. Annual book of ASTM standards. Philadelphia, PA: ASTM; 2010.

94. Zhao M-C, Liu M, Song G, Atrens A. Influence of the β-phase morphology on the corrosion of the Mg alloy AZ91. Corrosion Science. 2008;50(7):1939-53.

95. StJohn DH, Qian M, Easton MA, Cao P, Hildebrand Z. Grain refinement of magnesium alloys. 2005;36:1669-79.

96. Saha P, Lolies K, Viswanathan S, Gokhale A, Batson R. A Systematic Study of the Grain Refinement of Magnesium by Zirconium: Minerals, Metals and Materials Society/AIME, 420 Commonwealth Dr., P. O. Box 430 Warrendale PA 15086 USA; 2010.

97. Saha P, Viswanathan S, editors. An analysis of the grain refinement of magnesium by zirconium. Magnesium Technology 2011 - TMS 2011 Annual Meeting and Exhibition, February 27, 2011 - March 3, 2011; 2011; San Diego, CA, United states: Minerals, Metals and Materials Society.

98. Saha P, Viswanathan S. Grain refinement of magnesium by zirconium: characterization and analysis (11-066). AFS Transactions-American Foundry Society. 2011;119:469-80.

99. Maxwell I, Hellawell A. A simple model for grain refinement during solidification. Acta Metallurgica. 1975;23(2):229-37.

100. Greer AL, Bunn AM, Tronche A, Evans PV, Bristow DJ. Modelling of inoculation of metallic melts: application to grain refinement of aluminium by Al-Ti-B. Acta Materialia. 2000;48(11):2823-35.

101. Lee Y, Dahle A, StJohn D. The role of solute in grain refinement of magnesium. Metallurgical and Materials Transactions A. 2000;31(11):2895-906.

102. Okamoto H. Comment on Mg-Zn (magnesium-zinc). Journal of Phase Equilibria. 1994;15(1):129-30.

103. Kirkland NT, Birbilis N, Staiger MP. Assessing the corrosion of biodegradable magnesium implants: A critical review of current methodologies and their limitations. Acta Biomaterialia. 2012;8(3):925-36.

104. Shi Z, Song G, Atrens A. Corrosion resistance of anodised single-phase Mg alloys. Surface and Coatings Technology. 2006;201(1–2):492-503.

105. Song G, Atrens A. Recent Insights into the Mechanism of Magnesium Corrosion and Research Suggestions. Adv Eng Mater. 2007;9(3):177-83.

106. Song GL, Atrens A. Corrosion Mechanisms of Magnesium Alloys. Adv Eng Mater. 1999;1(1):11-33.

107. Material ASfTa. ASTM E8-04 Standard Test Methods for Tension Testing of Metallic Materials. Annual book of ASTM standards. Philadelphia, PA: ASTM; 2004.

108. Material ASfTa. ASTM G31-72 Standard Practice for Laboratory Immersion Corrosion Testing of Metals. Annual book of ASTM standards. Philadelphia, PA: ASTM; 2004.

109. Standardization IO. Biological evaluation of medical devices -- Part 12: Sample preparation and reference materials. ISO 10993-12:20072007.

110. Fischer J, Prosenc MH, Wolff M, Hort N, Willumeit R, Feyerabend F. Interference of magnesium corrosion with tetrazolium-based cytotoxicity assays. Acta Biomaterialia. 2010;6(5):1813-23.

111. Witte F, Hort N, Vogt C, Cohen S, Kainer KU, Willumeit R, et al. Degradable biomaterials based on magnesium corrosion. Current Opinion in Solid State & Materials Science. 2008;12(5-6):63-72.

112. Hall HO. Proc Phys Soc B. 1951;64:747-53.

113. Petch NJ, Iron Steel IJ. London. 1953;173:25.

114. Baker H, Okamoto H. ASM Handbook, Volume 03 - Alloy Phase Diagrams. ASM International.

115. Xin Y, Hu T, Chu PK. In vitro studies of biomedical magnesium alloys in a simulated physiological environment: A review. Acta Biomaterialia. 2011;7(4):1452-9.

116. Boehlert CJ, Knittel K. The microstructure, tensile properties, and creep behavior of Mg–Zn alloys containing 0–4.4wt.% Zn. Materials Science and Engineering: A. 2006;417(1–2):315-21.

117. Peng Q, Li X, Ma N, Liu R, Zhang H. Effects of backward extrusion on mechanical and degradation properties of Mg–Zn biomaterial. Journal of the Mechanical Behavior of Biomedical Materials. 2012;10(0):128-37.

118. Wei S, Zhu T, Hodgson M, Gao W. Effects of lead addition on the microstructure and mechanical properties of as-cast Mg–4Zn alloys. Materials Science and Engineering: A. 2012;550(0):199-205.

119. Zhang S, Li J, Song Y, Zhao C, Zhang X, Xie C, et al. In vitro degradation, hemolysis and MC3T3-E1 cell adhesion of biodegradable Mg–Zn alloy. Materials Science and Engineering: C. 2009;29(6):1907-12.

120. Zhang S, Zhang X, Zhao C, Li J, Song Y, Xie C, et al. Research on an Mg–Zn alloy as a degradable biomaterial. Acta Biomaterialia. 2010;6(2):626-40.

121. Fischer J, Pröfrock D, Hort N, Willumeit R, Feyerabend F. Improved cytotoxicity testing of magnesium materials. Materials Science and Engineering: B. 2011;176(11):830-4.

122. Contiguglia S, Alfrey A, Miller N, Butkus D. TOTAL-BODY MAGNESIUM EXCESS IN CHRONIC RENAL FAILURE. The Lancet. 1972;299(7764):1300-2.

123. Watanabe H, Mukai T, Ishikawa K, Mabuchi M, Higashi K. Realization of high-strain-rate superplasticity at low temperatures in a Mg–Zn–Zr alloy. Materials Science and Engineering: A. 2001;307(1–2):119-28.

124. Shahzad M, Wagner L. Microstructure development during extrusion in a wrought Mg–Zn–Zr alloy. Scripta Materialia. 2009;60(7):536-8.

125. Lin L, Liu Z, Chen L, Liu T, Wu S. Microstructure evolution and low temperature superplasticity of ZK40 magnesium alloy subjected to ECAP. Met Mater Int. 2004;10(6):501-6.

126. Zheng YF, Gu XN, Witte F. Biodegradable metals. Materials Science and Engineering: R: Reports. 2014;77(0):1-34.

127. Witte F, Kaese V, Haferkamp H, Switzer E, Meyer-Lindenberg A, Wirth CJ, et al. In vivo corrosion of four magnesium alloys and the associated bone response. Biomaterials. 2005;26(17):3557-63.

128. Luthringer BJ, Feyerabend F, Willumeit-Römer R. Magnesium-based implants: a mini-review. Magnesium Research. 2014;27(4):142-54.

129. Han H-S, Minghui Y, Seok H-K, Byun J-Y, Cha P-R, Yang S-J, et al. The modification of microstructure to improve the biodegradation and mechanical properties of a biodegradable Mg alloy. Journal of the mechanical behavior of biomedical materials. 2013;20(0):54-60.

130. Yang XM, Li M, Lin X, Tan LL, Lan GB, Li LH, et al. Enhanced in vitro biocompatibility/bioactivity of biodegradable Mg-Zn-Zr alloy by micro-arc oxidation coating contained Mg2SiO4. Surf Coat Tech. 2013;233:65-73.

131. Gu XN, Li N, Zheng YF, Ruan LQ. In vitro degradation performance and biological response of a Mg-Zn-Zr alloy. Mater Sci Eng B-Adv Funct Solid-State Mater. 2011;176(20):1778-84.

132. Emley EF. Principles of magnesium technology. 1st ed. Oxford, New York,: Pergamon Press; 1966. xx, 1013 p. p.

133. Nayeb-Hashemi AA, Clark JB, ASM International. Phase diagrams of binary magnesium alloys. Metals Park, Ohio: ASM International; 1988. ix, 370 p. p.

134. Liu L, Chen X, Pan F, Wang Z, Liu W, Cao P, et al. Effect of Y and Ce additions on microstructure and mechanical properties of Mg–Zn–Zr alloys. Materials Science and Engineering: A. 2015;644:247-53.

135. Li Q, Wang Q, Wang Y, Zeng X, Ding W. Effect of Nd and Y addition on microstructure and mechanical properties of as-cast Mg–Zn–Zr alloy. Journal of Alloys and Compounds. 2007;427(1–2):115-23.

136. Ding WJ, Wu YJ, Peng LM, Zeng XQ, Yuan GY, Lin DL. Formation of 14H-type long period stacking ordered structure in the as-cast and solid solution treated Mg–Gd–Zn–Zr alloys. Journal of Materials Research. 2009;24(05):1842-54.

137. Sila-Asna M, Bunyaratvej A, Maeda S, Kitaguchi H, Bunyaratavej N. Osteoblast differentiation and bone formation gene expression in strontium-inducing bone marrow mesenchymal stem cell. Kobe J Med Sci. 2007;53(1-2):25-35.

138. Bornapour M, Muja N, Shum-Tim D, Cerruti M, Pekguleryuz M. Biocompatibility and biodegradability of Mg–Sr alloys: The formation of Sr-substituted hydroxyapatite. Acta Biomaterialia. 2013;9(2):5319-30.

139. Brar HS, Wong J, Manuel MV. Investigation of the mechanical and degradation properties of Mg-Sr and Mg-Zn-Sr alloys for use as potential biodegradable implant materials. Journal of the mechanical behavior of biomedical materials. 2012;7:87-95.

140. ISO 10993-5(2009), Biological evaluation of medical devices – Part 5: Tests for in vitro cytotoxicity, International Organization for Standardization.

141. Witte F, Fischer J, Nellesen J, Crostack HA, Kaese V, Pisch A, et al. In vitro and in vivo corrosion measurements of magnesium alloys. Biomaterials. 2006;27(7):1013-8.

142. Yoshizawa S, Brown A, Barchowsky A, Sfeir C. Magnesium ion stimulation of bone marrow stromal cells enhances osteogenic activity, simulating the effect of magnesium alloy degradation. Acta Biomaterialia. 2014;10(6):2834-42.

143. Lian JB, Stein GS. Concepts of osteoblast growth and differentiation: basis for modulation of bone cell development and tissue formation. Crit Rev Oral Biol Med. 1992;3(3):269-305.

144. Marie PJ, Fromigué O. Osteogenic differentiation of human marrow-derived mesenchymal stem cells. Regenerative Medicine. 2006;1(4):539-48.

145. Zheng Y, Gu X, Witte F. Biodegradable metals. Materials Science and Engineering: R: Reports. 2014;77:1-34.

146. Witte F. The history of biodegradable magnesium implants: a review. Acta biomaterialia. 2010;6(5):1680-92.

147. Kirkland NT. Magnesium biomaterials: past, present and future. Corros Eng Sci Techn. 2012;47(5):322-8.

148. Feyerabend F, Fischer J, Holtz J, Witte F, Willumeit R, Drucker H, et al. Evaluation of short-term effects of rare earth and other elements used in magnesium alloys on primary cells and cell lines. Acta Biomaterialia. 2010;6(5):1834-42.

149. Fischer J, Profrock D, Hort N, Willumeit R, Feyerabend F. Improved cytotoxicity testing of magnesium materials. Mater Sci Eng B-Adv Funct Solid-State Mater. 2011;176(11):830-4.

150. Chaya A, Yoshizawa S, Verdelis K, Myers N, Costello BJ, Chou D-T, et al. In vivo study of magnesium plate and screw degradation and bone fracture healing. Acta Biomaterialia. 2015;18(0):262-9.

151. Fallah AA, Saei-Dehkordi SS, Nematollahi A, Jafari T. Comparative study of heavy metal and trace element accumulation in edible tissues of farmed and wild rainbow trout (Oncorhynchus mykiss) using ICP-OES technique. Microchemical Journal. 2011;98(2):275-9.

152. Engström E, Stenberg A, Senioukh S, Edelbro R, Baxter DC, Rodushkin I. Multi-elemental characterization of soft biological tissues by inductively coupled plasma–sector field mass spectrometry. Analytica Chimica Acta. 2004;521(2):123-35.

153. Zhang E, Xu L, Yu G, Pan F, Yang K. In vivo evaluation of biodegradable magnesium alloy bone implant in the first 6 months implantation. Journal of Biomedical Materials Research Part A. 2009;90A(3):882-93.

154. Iglesias C, Bodelón OG, Montoya R, Clemente C, Garcia-Alonso MC, Rubio JC, et al. Fracture bone healing and biodegradation of AZ31 implant in rats. Biomedical Materials. 2015;10(2):025008.

155. Unigovski Y, Eliezer A, Abramov E, Snir Y, Gutman E. Corrosion fatigue of extruded magnesium alloys. Materials Science and Engineering: A. 2003;360(1):132-9.

156. Kannan MB, Raman RKS, Witte F, Blawert C, Dietzel W. Influence of circumferential notch and fatigue crack on the mechanical integrity of biodegradable magnesium-based alloy in simulated body fluid. Journal of Biomedical Materials Research Part B-Applied Biomaterials. 2011;96B(2):303-9.

157. Kannan MB, Raman RKS. In vitro degradation and mechanical integrity of calcium-containing magnesium alloys in modified-simulated body fluid. Biomaterials. 2008;29(15):2306-14.

158. Xu L, Yu G, Zhang E, Pan F, Yang K. In vivo corrosion behavior of Mg-Mn-Zn alloy for bone implant application. Journal of Biomedical Materials Research Part A. 2007;83A(3):703-11.

159. Mordes JP, Wacker WE. Excess magnesium. Pharmacological Reviews. 1977;29(4):273-300.

160. David D. Maxillofacial trauma: principles of management, priorities and basic techniques. Trauma. 1999;1(3):215-26.

161. SCHMITZ JP, Hollinger JO. The critical size defect as an experimental model for craniomandibulofacial nonunions. Clinical orthopaedics and related research. 1986;205:299-308.

162. Hollinger JO, Kleinschmidt JC. The critical size defect as an experimental model to test bone repair materials. Journal of Craniofacial Surgery. 1990;1(1):60-8.

163. Ciocca L, Mazzoni S, Fantini M, Persiani F, Marchetti C, Scotti R. CAD/CAM guided secondary mandibular reconstruction of a discontinuity defect after ablative cancer surgery. Journal of Cranio-Maxillofacial Surgery. 2012;40(8):e511-e5.

164. Eufinger H, Harders A, Heuser L, Kruse D, Machtens E, Wehmoller M. Reconstruction of craniofacial bone defects with individual alloplastic implants based on CAD/CAM-manipulated CT-data. Journal of Cranio-Maxillofacial Surgery. 1995;23:175+.

165. Scolozzi P, Martinez A, Jaques B. Complex orbito-fronto-temporal reconstruction using computer-designed PEEK implant. Journal of Craniofacial Surgery. 2007;18(1):224-8.

166. Heissler E, Fischer FS, Boiouri S, Lehrnann T, Mathar W, Gebhardt A, et al. Custom-made cast titanium implants produced with CAD/CAM for the reconstruction of cranium defects. International Journal of Oral and Maxillofacial Surgery. 1998;27(5):334-8.

167. Grandfield K, Palmquist A, Gonçalves S, Taylor A, Taylor M, Emanuelsson L, et al. Free form fabricated features on CoCr implants with and without hydroxyapatite coating in vivo: a comparative study of bone contact and bone growth induction. Journal of Materials Science: Materials in Medicine. 2011;22(4):899-906.

168. Fierz FC, Beckmann F, Huser M, Irsen SH, Leukers B, Witte F, et al. The morphology of anisotropic 3D-printed hydroxyapatite scaffolds. Biomaterials. 2008;29(28):3799-806.

169. Younger EM, Chapman MW. Morbidity at bone graft donor sites. Journal of orthopaedic trauma. 1989;3(3):192-5.

170. Bohner M. Resorbable biomaterials as bone graft substitutes. Materials Today. 2010;13(1–2):24-30.

171. Jorgenson DS, Mayer MH, Ellenbogen RG, Centeno JA, Johnson FB, Mullick FG, et al. Detection of titanium in human tissues after craniofacial surgery. Plastic and reconstructive surgery. 1997;99(4):976-9.

172. Zaffe D, Bertoldi C, Consolo U. Accumulation of aluminium in lamellar bone after implantation of titanium plates, Ti–6Al–4V screws, hydroxyapatite granules. Biomaterials. 2004;25(17):3837-44.

173. Song G. Control of biodegradation of biocompatable magnesium alloys. Corrosion Science. 2007;49(4):1696-701.

174. Giesekel M, Noelkel C, Kaierlel S, Weslingl V, Haferkarnp H. Selective Laser Melting of Magnesium and Magnesium Alloys. Magnesium Technology 2013. 2013:65-8.

175. Hermawan H, Alamdari H, Mantovani D, Dubé D. Iron–manganese: new class of metallic degradable biomaterials prepared by powder metallurgy. Powder Metallurgy. 2008;51(1):38-45.

176. Liu B, Zheng Y, Ruan L. In vitro investigation of Fe30Mn6Si shape memory alloy as potential biodegradable metallic material. Materials Letters. 2011;65(3):540-3.

177. Schinhammer M, Hänzi AC, Löffler JF, Uggowitzer PJ. Design strategy for biodegradable Fe-based alloys for medical applications. Acta Biomaterialia. 2010;6(5):1705-13.

178. Huang T, Cheng J, Zheng Y. In vitro degradation and biocompatibility of Fe–Pd and Fe–Pt composites fabricated by spark plasma sintering. Materials Science and Engineering: C. 2014;35:43-53.

179. Cheng J, Zheng Y. In vitro study on newly designed biodegradable Fe-X composites (X= W, CNT) prepared by spark plasma sintering. Journal of Biomedical Materials Research Part B: Applied Biomaterials. 2013;101(4):485-97.

180. Schinhammer M, Steiger P, Moszner F, Löffler JF, Uggowitzer PJ. Degradation performance of biodegradable FeMnC(Pd) alloys. Materials Science and Engineering: C. 2013;33(4):1882-93.

181. Kraus T, Moszner F, Fischerauer S, Fiedler M, Martinelli E, Eichler J, et al. Biodegradable Fe-based alloys for use in osteosynthesis: Outcome of an in vivo study after 52weeks. Acta biomaterialia. 2014;10(7):3346-53.

182. Chou D-T, Wells D, Hong D, Lee B, Kuhn H, Kumta PN. Novel processing of iron–manganese alloy-based biomaterials by inkjet 3-D printing. Acta Biomaterialia. 2013;9(10):8593-603.

183. Velikokhatnyi OI, Kumta PN. First-principles studies on alloying and simplified thermodynamic aqueous chemical stability of calcium-, zinc-, aluminum-, yttrium- and iron-doped magnesium alloys. Acta Biomaterialia. 2010;6(5):1698-704.

184. Saunders N, Miodownik AP. CALPHAD (Calculation of Phase Diagrams): A Comprehensive Guide: A Comprehensive Guide: Elsevier Science; 1998.

185. Andersson JO, Helander T, Hoglund LH, Shi PF, Sundman B. THERMO-CALC & DICTRA, computational tools for materials science. Calphad-Computer Coupling of Phase Diagrams and Thermochemistry. 2002;26(2):273-312.

186. Thermo-Calc Software SSUB5 SGTE Substances Database version 5.1, (Accessed 23 Aug 2013).

187. Lee Y-K, Jun J-H, Choi C-S. Damping Capacity in Fe-Mn Binary Alloys. ISIJ International. 1997;37(10):1023-30.

188. Huang T, Cheng J, Bian D, Zheng Y. Fe–Au and Fe–Ag composites as candidates for biodegradable stent materials. Journal of Biomedical Materials Research Part B: Applied Biomaterials. 2015:n/a-n/a.

189. Xu Z, Hodgson MA, Cao P. A comparative study of powder metallurgical (PM) and wrought Fe–Mn–Si alloys. Materials Science and Engineering: A. 2015;630(0):116-24.

190. Dimitrov D, Schreve K, De Beer N. Advances in Three Dimensional Printing - state of the art and future perspectives2006; 4(1):[p.21-49 pp.]. Available from: http://reference.sabinet.co.za/webx/access/electronic_journals/newgen/newgen_v4_n1_a3.pdf.

191. Hong SB, Eliaz N, Sachs EM, Allen SM, Latanision RM. Corrosion behavior of advanced titanium-based alloys made by three-dimensional printing (3DPTM) for biomedical applications. Corrosion Science. 2001;43(9):1781-91.

192. Purnama A, Mantovani D, Couet J. Caveolin: A possible biomarker of degradable metallic materials toxicity in vascular cells. Acta biomaterialia. 2013;9(10):8754-60.